

SRB Project

A Dissertation by Nabil Akbar

Volume 54

**SEISMIC SIGNATURES OF RESERVOIR TRANSPORT
PROPERTIES AND PORE FLUID DISTRIBUTION**

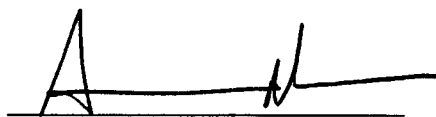
**A DISSERTATION
SUBMITTED TO THE DEPARTMENT OF GEOPHYSICS
AND THE COMMITTEE ON GRADUATE STUDIES
OF STANFORD UNIVERSITY
IN PARTIAL FULFILLMENT OF THE REQUIREMENTS
FOR THE DEGREE OF
DOCTOR OF PHILOSOPHY**

Nabil Akbar

June 1993

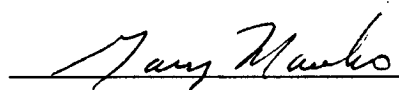
©Copyright by Nabil Akbar 1993
All Right Reserved

I certify that I have read this dissertation and that in my opinion it is fully adequate, in scope and quality, as a dissertation for the degree of Doctor of Philosophy.

A handwritten signature in black ink, appearing to read 'Amos Nur', written over a horizontal line.

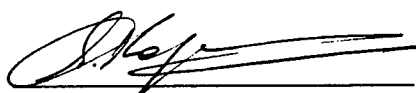
Amos Nur (Principal Adviser)

I certify that I have read this dissertation and that in my opinion it is fully adequate, in scope and quality, as a dissertation for the degree of Doctor of Philosophy.

A handwritten signature in black ink, appearing to read 'Gary Mavko', written over a horizontal line.

Gary Mavko (Geophysics)

I certify that I have read this dissertation and that in my opinion it is fully adequate, in scope and quality, as a dissertation for the degree of Doctor of Philosophy.

A handwritten signature in black ink, appearing to read 'Jack Dvorkin', written over a horizontal line.

Jack Dvorkin (Geophysics)

Approved for the University Committee on Graduate Studies:

ABSTRACT

We investigate the effects of permeability, frequency, and fluid distribution on the viscoelastic behavior of rock. The viscoelastic response of rock to seismic waves depends on the relative motion of pore fluid with respect to the solid phase. Fluid motion depends, in part, on the internal wave-induced pore pressure distribution that relates to the pore microstructure of rock, and the scales of saturation. We consider wave-induced squirt fluid flow at two scales: (1) local microscopic flow at the smallest scale of saturation heterogeneity (e.g., within a single pore) and (2) macroscopic flow at a larger scale of fluid-saturated and dry patches. We explore the circumstances under which each of these mechanisms prevails. We examine such flows under the conditions of uniform confining (bulk) compression and obtain the effective dynamic bulk modulus of rock. The solutions are formulated in terms of generalized frequencies that depend on frequency, saturation, fluid and gas properties; and on the macroscopic properties of rock such as permeability, porosity, and dry bulk modulus. The study includes the whole range of saturation and frequency; therefore, we provide the missing link between the low-frequency limit (Gassmann's formula) and the high frequency limit given by Mavko and Jizba. Further, we compare our model with Biot's theory and introduce a geometrical factor whose numeric value gives an indication to whether the local fluid squirt or the global (squirt and/or Biot's) mechanisms dominate the viscoelastic properties of porous materials.

The important results of our theoretical modeling are: (1) a hysteresis of seismic velocity versus saturation due to variations in fluid distributions, and (2) two peaks of acoustic wave attenuation – one at low frequency (due to the global squirt flow) and another at higher frequency (due to the local flow). Both theoretical results are well supported by experimental data.

To little nabil, the child within,
and to big Ameera
who took well care of little nabil.

ACKNOWLEDGEMENTS

It is all over now, and it all goes to those sincere people who gave me their best wishes, support, and knowledge.

My grandfather Isam-Aldeen, who died lonely in Turkey, back in 1983. "Where is Nabil?", he said, "I wish he came ... please ... give him some of my money ... he needs it in America ..." he said in his last moments. Well, Isam, it is your final best wishes that make my real treasure.

The research presented in this dissertation is a result of enormous discussions with Amos Nur, my principal advisor, Gary Mavko, and Jack Dvorkin. I would like to thank Amos for his endless patience, care, and sincerity. This work has benefited greatly from Gary Mavko and his outstanding publications.

I want to give my appreciation to Dr. A. Fuda at SAUDI ARAMCO, and Dr. J. Dvorkin at Stanford. This work would simply be impossible without their support. "An intersection of space and time gathered us," Jack once explained to me. I am so grateful to J. Dvorkin for his advice, friendship, experience, and kindness. I benefited greatly from the long hours we spent together discussing the research.

I am grateful to my professors M. Zoback, J. Harris, N. Sleep, P. Segal, and S. Graham, for their support during my study. Tapan Mukerji is a quiet, nice, and sincere person from whose friendship I benefited a great deal. I would like to thank Margaret Muir for always being there.

I have been blessed with my wife Ameera and my three children, Nouruddin, Hashim, and Zainalabdeen whose kindness and love made this doctorate possible. "Do you like yourself, Dad?", a six-year old Nouruddin once asked after seeing me under stress one day. "Yes Nouruddin. Why do you ask?" "Because you look sad today!" "And who taught you all this wisdom, son? It is just the blessing ..." I wondered to myself.

I will never forget the day of one of my qualifying exams ... I was running unconsciously to my car, when Nouruddin and Hashim insisted on following me up to the

sidewalk. "Why do not you get into the house???", I shouted unconsciously at them. They did not obey me. Standing shoulder to shoulder, like two little roses in a wild field, they started waving their tiny hands together until I left the scene. It is just as if they knew it all ... "Dad is up to something serious ... we wish you well, Dad."

I had ups and downs. My wife Ameera was always with me. I found the hope in her heart whenever I lost it. "To me, You are the best ... in the whole world ... no matter what," she said once in a cold long night. My last resort, an elegant, wise woman, whom I always find when I need most.

This work was sponsored by SAUDI ARAMCO. I am indebted to the Vice President Mr. Mahmood Abdulbaqi, and the Geophysics Manager Mr. John Ward for their support and encouragement. Also, I want to thank S. Al-Ghamdi from Dhahran and Mr. T. Bishop from Houston for their support during my study. Also, I would like to thank my friend Saleh Al-Maglouth for his nice companionship during his two-year study at Stanford.

Finally, I want to thank that great woman ... Safia ... the daughter of Isam-Aldeen ... my mother ... for sacrificing her life to her little children ...

TABLE OF CONTENTS

GENERAL INTRODUCTION	1
CHAPTER 1	
Relating P-Wave Attenuation to Permeability	7
Abstract	8
Introduction	8
Theoretical Model	10
Pore Wall Displacements	10
Pore Fluid Dynamics	12
Numerical Analysis	16
Comparison With Data	23
Conclusions	29
Acknowledgments	29
References	30
Appendix A- The Peak of Stored Energy	31
Work done by the actual set of tractions	33
Work done by the artificial set of tractions	35
Appendix B- Stresses and Strains	38
Appendix C - Permeability Calculations	39
CHAPTER 2	
Relating P-Wave Attenuation to Permeability Anisotropy	40
Abstract	41
Introduction	41
Theoretical Model	43
Numerical Analysis	46
Rock With Isotropic Permeability	46
Effects of the drop length on attenuation	47
Effects of frequency	47

Rock With Anisotropic Permeability	51
Effects of frequency	51
Effects of length of the fluid drop	60
Comparison With Data	63
Effect of frequency on permeability-attenuation relation	63
Permeabilities along two perpendicular directions	67
Conclusions	69
References	70
CHAPTER 3	
Seismic Signatures of Reservoir Transport Properties	71
Abstract	72
Introduction	73
Basic Assumptions and Definitions	76
Microscopic Squirt Flow	76
Macroscopic Squirt Flow	79
Microscopic Versus Macroscopic Squirt	81
Theoretical Model	83
Uniform Saturation	83
Porosity estimates	83
Compressibility estimates	84
Relations between α , β , ℓ , and the bulk properties	88
Case $\alpha \sim 0$	89
Case $\alpha \sim 1$	90
Case $\alpha \sim \infty$	90
Limits imposed on β	91
Hydrodynamics	93
Average fluid pressure	94
Non-Uniform Saturation	97
Average fluid pressure	98

Approximated relations between local and global characteristic frequencies	99
Dynamic Bulk Modulus and Applications	100
Uniform Fluid Distribution	100
Non-Uniform Fluid Distribution	101
Heterogeneous fluid distribution due to saturation processes	101
Fully saturated patches	101
Partially saturated patches	102
Effects of medium heterogeneity at global scale	102
Seismic Wave Velocities	103
Comparison With Other Models	104
Low/High frequency limits	104
O'Connell and Budiansky	104
The Biot's theory, Biot	105
1) Effects of permeability and fluid distribution	105
2) Critical frequencies	106
Comparison With Data	107
Uniform Fluid Distribution	107
Effects of confining pressure	107
Effects of saturation hysteresis	115
A qualitative relation between permeability and the scale of the microscopic heterogeneity	116
Non-Uniform Fluid Distribution	121
Effects of frequency	121
Conclusions	126
Acknowledgements	126
Appendix A: Volumetric Strains	127
Pore wall displacements	128

Appendix B: Gas Pressure	129
Appendix C: Fluid Pressure in a Needle-Like Conduit	133
Appendix D: Fluid Pressure in a Two-Dimensional Conduit	135
Appendix E: Fluid Pressure in a Penny-Shaped Crack	137
Appendix F: A Unified Expression for Fluid Pressure for Unidirectional Flow	139
Appendix G: Effects of Radial Flow on Fluid Pressure	141
Appendix H: Fluid Pressure in a Macroscopic Conduit	143
Appendix I: Bulk Modulus Calculations	145
Appendix J: Limits Imposed on β	147
References	148

LIST OF TABLES

Table 1.1. Permeabilities and the corresponding attenuations of ultrasonic frequencies (N. Lucet, 1989).	27
Table 1.2. Permeabilities and the corresponding attenuations of sonic frequencies (N. Lucet, 1989).	28
Table 2.1. The calculated pore radii and attenuation $\log Q_p^{-1}$ for ultrasonic frequencies.	65
Table 2.2. The calculated pore radii and attenuation $\log Q_p^{-1}$ for sonic frequencies.	65
Table 3.1. Rock and fluid properties used in plotting Figure 3.12.	120

LIST OF FIGURES

Fig. I.1. Some examples of using seismic wave methods in oil-related industries.	1
Fig. I.2. Wave propagation through a porous material causes two main components of solid/fluid relative displacements: (a) Biot's and (b) the squirt mechanisms.	3
Fig. 1.1. An element with a single cylindrical pore embedded in an isotropic homogeneous block.	11
Fig. 1.2. The plot of $\text{Log}Q^{-1}$ versus $\text{Log}f$ for $\delta = 0^\circ, 45^\circ, \text{ and } 90^\circ$.	17
Fig. 1.3. $\text{Log}Q^{-1}$ versus $\text{Log}a_0$ for: $\delta = 0^\circ, 30^\circ, 60^\circ, \text{ and } 90^\circ$.	18
Fig. 1.4. $\text{Log}Q^{-1}$ versus saturation for $\delta = 0^\circ, 45^\circ, \text{ and } 90^\circ$.	20
Fig. 1.5. The effects of frequency, pore's radius, and saturation on the Q^{-1} - δ relation.	21
Fig. 1.6. $\text{Log}Q^{-1}$ versus $\text{Log}k$ for three frequencies: $f = 5 \text{ kHz}, 50 \text{ kHz}, \text{ and } .5 \text{ MHz}$.	22
Fig. 1.7. Permeability (mD) versus attenuation coefficient.	24

- Fig. 1.8. The measured and the estimated Q_p^{-1} versus permeability for Fontainebleau sandstone. Data obtained from Lucet (1989). 26
- Fig. 1.9. (a) Stresses and displacements in the actual element;
(b) an artificial element containing a single pore. 32
- Fig. 1.10. (a) The actual system forces acting on the artificial element;
(b) artificial system showing the components of fluid pressure. 34
- Fig. 1.11. (a) Artificial tractions acting on the actual system;
(b) the normal component of stress. 36
- Fig. 2.1. (a) A sample with permeabilities k_x and k_z ($k_x > k_z$) along two perpendicular directions.
(1b) Two perpendicular pores with radii r_x and r_z . 45
- Fig. 2.2. $\log Q_p^{-1}$ versus the length of the fluid drop L . 48
- Fig. 2.3. $\log Q^{-1}$ versus L using the properties of crude oil as a saturating fluid. 49
- Fig. 2.4. $\log Q^{-1}$ versus $\log k$ for three frequencies. 50
- Fig. 2.5. $\log Q^{-1}$ versus incident angle δ for a rock with permeabilities 100 mD and 1000 mD along two perpendicular directions. 53

- Fig. 2.6. $\log Q^{-1}$ versus incident angle δ for a rock with permeabilities .1 mD and 10 mD along two perpendicular directions. 54
- Fig. 2.7. $\log Q^{-1}$ versus k and ω for a rock with isotropic permeability. 56
- Fig. 2.8. $\log Q^{-1}$ versus δ and ω for a rock with permeabilities 100 mD and 1000 mD along two perpendicular directions. 57
- Fig. 2.9. $\log Q^{-1}$ versus δ and ω for a rock with permeabilities $k = .1$ mD and 10 mD along two perpendicular directions. 59
- Fig. 2.10. The attenuation ratio versus $\log k_{max}$ and $\log \omega$ for a water-saturated rock. 61
- Fig. 2.11. The attenuation ratio versus k_{max} and ω for $L = 4$ mm. 62
- Fig. 2.12. The measured and the calculated Q_p^{-1} versus permeability for Fontainebleau sandstones. Data are from Lucet (1989). 66
- Fig. 2.13. The attenuation ratio \tilde{R} versus saturation for Meule Vert sandstone sample. The data are from Tarif (1986). 68
- Fig. 3.1. (a) An accumulation of microscopic units; (b) local fluid flow within a microscopic unit; and (c) a network of few microscopic units. 78

- Fig. 3.2. (a) Non-uniformly saturated rock; (b) a macroscopic unit; and (c) a macroscopic conduit. 80
- Fig. 3.3. Graphic images for the relations between the geometrical factor α and the microscopic structure of the rocks. 92
- Fig. 3.4. Measured bulk modulus for dry, water-saturated, and benzene saturated Berea sandstone versus differential pressure (Coyner, 1977). 109
- Fig. 3.5. Measured compressional and shear wave velocities V_p and V_s for water-saturated Berea sandstone versus differential pressure (Coyner, 1977). 110
- Fig. 3.6. Measured compressional and shear wave velocities V_p and V_s for benzene-saturated Berea sandstone versus differential pressure (Coyner, 1977). 111
- Fig. 3.7. Calculated bulk attenuation versus confining pressure for water and benzene-saturated Berea sandstone. 112
- Fig. 3.8. Calculated P-wave attenuation versus confining pressure for water and benzene-saturated Berea sandstone. 113
- Fig. 3.9. Calculated S-wave attenuation versus confining pressure for water and benzene-saturated Berea sandstone. 114

- Fig. 3.10. Bulk modulus calculated from measured V_p and V_s versus saturation for drainage and imbibition in a tight gas sandstone (Knight and Nolen-Hoeksema, 1990). 117
- Fig. 3.11. Conduit saturation versus overall saturation for drainage and imbibition. These functions were used in calculating bulk modulus shown in Figure 3.10. 118
- Fig. 3.12. The scale of the microscopic heterogeneity ℓ versus permeability for different rock samples. 119
- Fig. 3.13. Attenuation Q_K^{-1} as calculated from measured Q_E^{-1} and Q_S^{-1} versus frequency for Harz quartzite (Paffenholz and Burkhardt, 1989). 123
- Fig. 3.14. Attenuation of extensional waves Q_E^{-1} versus frequency for Harz quartzite (Paffenholz and Burkhardt, 1989). 124
- Fig. 3.15. Shear wave attenuation Q_S^{-1} versus frequency for Harz quartzite (Paffenholz and Burkhardt, 1989). 125
- Fig. 3.16 (a) A microscopic unit composed of partially saturated stiff pore and a conduit; (b) a needle-like conduit; (c) a two-dimensional conduit; and (d) a penny-shaped conduit. 132

GENERAL INTRODUCTION

Seismic wave propagation in rocks is the most important tool in oil exploration. It is a direct, cheap, fast, and environmentally clean method that can be used in detecting geological features that might be of a great interest for oil and gas prospects. Common examples of using seismic wave methods in oil-related industries are (Figure 1):

- 1) Large scale measurements at low frequencies (10-100 Hz). This includes estimating interval velocity, reflection amplitude, and AVO analysis for a layered medium.
- 2) Intermediate scale with frequency range of 10-20 kHz. Examples of this are cross-borehole measurements, VSP, and sonic log analysis.
- 3) Small scale measurements using ultrasonic frequencies (0.1-1.0 MHz). This includes velocity and attenuation measurements on core samples in the laboratory.

It is crucial, therefore, to fully understand the effects of frequency, rock properties (permeability, porosity, compressibility, density, tortuosity, mineralogy, sorting and clay content), and fluid properties (viscosity, density, compressibility) on seismic wave properties (compressional and shear wave velocities and attenuation).

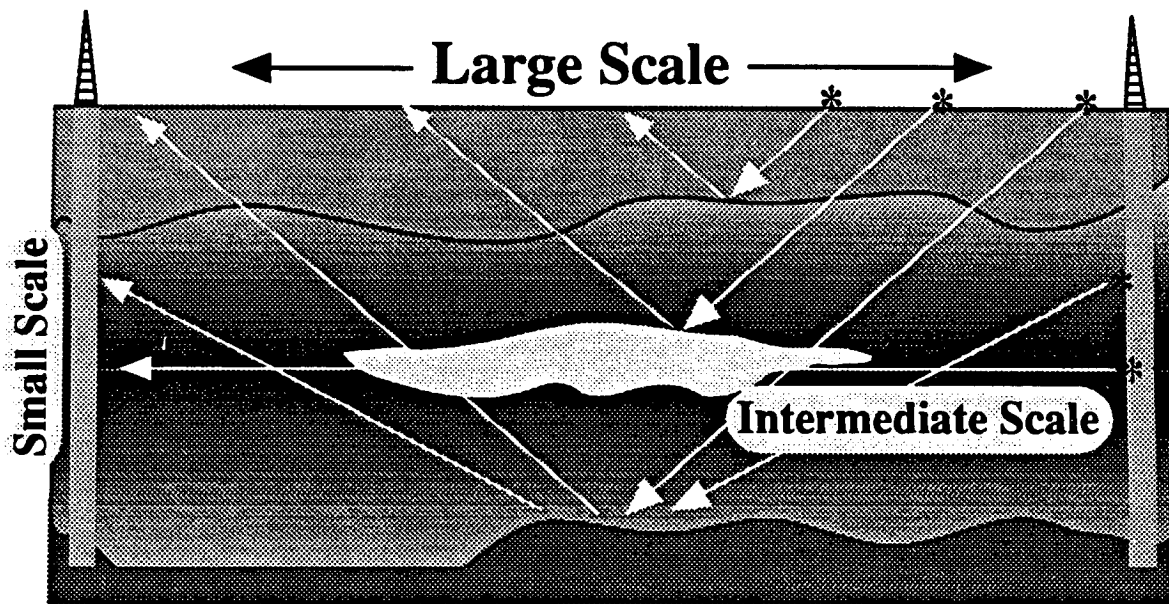


Fig. I.1. Some examples of using seismic wave methods in oil-related industries.

Wave propagation through a porous material causes two main components of solid/fluid relative displacements (Figure 2). The first one occurs when both solid and fluid move in the same direction which is the mechanism used in Biot's theory. The second type of the solid/fluid motion occurs when the solid and fluid phases move in perpendicular directions which is the squirt flow mechanism.

The objective of this dissertation is to relate seismic wave properties to rock and fluid properties. We achieve our goals by introducing theoretical models based on the squirt flow mechanism.

The velocities of seismic waves are related to the stiffness of the material that depends strongly on the wave-induced fluid pressure. The induced fluid pressure, in turn, depends on the rock and fluid properties. This allows us to relate velocities to rock and fluid properties. Attenuation of seismic waves depends on energy dissipation due to wave-induced fluid flow within pore space. Fluid flow, in turn, depends mainly on frequency, permeability, and fluid viscosity. This allows us to relate attenuation to rock and fluid properties.

The previous discussion shows the importance of wave-induced fluid flow and pressure on velocities and attenuation of seismic waves in rocks. When fluid is not allowed to flow, then rock behaves as an elastic material and the attenuation is relatively small. This corresponds to the following two extreme limits. First is the relaxed mode (small frequency and/or large permeability) in which fluid flows freely between pore space, and fluid pressure is small and uniform throughout the rock. Therefore, velocity is small, which corresponds to Gassmann's low frequency limit. Second, is the unrelaxed mode at which fluid flow is prevented due to high induced pressure (high frequency and/or small permeability). In this case, the material is stiffer and consequently the velocity is relatively large. This corresponds to the high frequency limit given by Mavko and Jizba (1991).

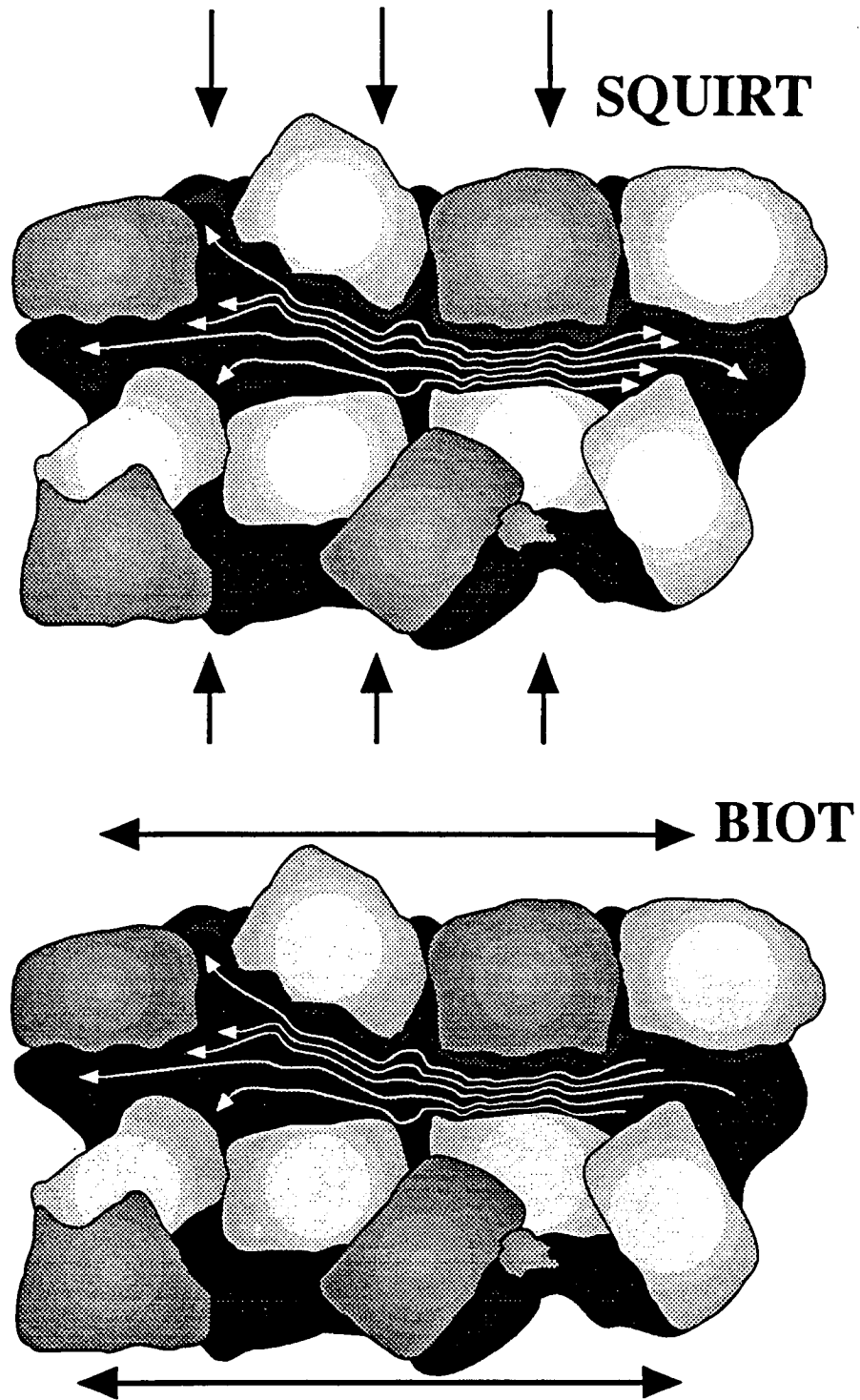


Fig. I.2. Wave propagation through a porous material causes two main components of solid/fluid relative displacements: (a) Biot's and (b) the squirt mechanisms.

At some intermediate frequencies or permeabilities, the fluid relaxation time from relaxed to unrelaxed modes is comparable to the seismic period, resulting in relatively large attenuation. This transition causes an effective viscoelastic behavior of the porous material.

Our model is based on the fact that viscoelastic behavior and rock and fluid properties are intimately linked with the process of fluid motion in the rock.

The examination of the squirt-flow mechanism in the literature has been restricted to the pore scale, requiring the consideration of specific pore or grain-contact geometries (e.g., Palmer and Traviolia, 1980; Murphy et al., 1986; Mavko and Nur, 1979; O'Connell and Budiansky 1977). This approach limits practical usage of the squirt-flow theories as they are not directly connected to measurable macroscopic rock properties (permeability, porosity, etc.). On the other hand, models relating bulk properties to seismic velocities ignore the viscoelastic effects (i.e., frequency dependence). These include the high frequency limit in which fluid is unrelaxed (Mavko and Jizba, 1991; Mavko and Nolen-Hoeksema, 1993), and the low frequency limit in which fluid is in the equilibrium state (Gassmann, 1951).

In this research, we relate rock and fluid properties, saturation, fluid distribution and frequency to the viscoelastic behavior of rock. One of the main goals is to relate, using the squirt-flow mechanism, the seismic wave velocities and attenuation of rock to measurable parameters such as permeability, porosity, dry bulk modulus and fluid and gas properties.

The dissertation is divided into three chapters. In the first chapter, we relate P-wave attenuation to permeability by assuming that pore space consists of needle-like pores filled with viscous fluid and embedded in an infinite isotropic elastic medium. We calculate both attenuation and permeability as functions of the direction of wave propagation measured from the main axis of the pore. We find that in the case when a plane P-wave propagates perpendicular to the pore axis, attenuation is always higher than when a wave propagates parallel to the pore axis. By changing permeability and varying the radius of the pore, we find that the permeability-attenuation relation

is characterized by a peak that shifts toward lower permeabilities as frequency decreases. Therefore, the attenuation of a low-frequency wave decreases with increasing permeability.

In the second chapter, we pursue the same theoretical approach and relate P-wave attenuation to permeability anisotropy. We investigate the effects of frequency, saturation, and magnitudes of permeabilities along two perpendicular directions on the permeability-attenuation relation. We find that the attenuation of a low frequency P-wave is minimum when the wave propagates perpendicular to the direction of maximum permeability.

The third chapter represents our main model in which we explore the effects of permeability, frequency, and fluid distribution on the viscoelastic behavior of rock. We consider wave-induced squirt fluid flow at two scales: (1) local microscopic flow at the smallest scale of saturation heterogeneity (e.g., within a single pore) and (2) macroscopic flow at a larger scale of fluid-saturated and dry patches. We explore the circumstances under which each of these mechanisms prevails. The solutions are formulated in terms of generalized frequencies that depend on frequency, saturation, fluid and gas properties; and on the macroscopic properties of rock such as permeability, porosity, and dry bulk modulus. The study includes the whole range of saturation and frequency; therefore, we provide the missing link between the low-frequency limit (Gassmann's formula) and the high frequency limit given by Mavko and Jizba. Further, we compare our model with Biot's theory and introduce a geometrical factor whose numeric value gives an indication to whether the local fluid squirt or the global (squirt and/or Biot's) mechanisms dominate the viscoelastic properties of porous materials.

The important results of our theoretical modeling are: (1) a hysteresis of seismic velocity versus saturation due to variations in fluid distributions, and (2) two peaks of acoustic wave attenuation – one at low frequency (due to the global squirt flow) and another at higher frequency (due to the local flow). Both theoretical results are well supported by experimental data.

REFERENCES

- Akbar, N., Dvorkin, J., and Nur, A., 1993, Relating P-wave attenuation to permeability: *Geophysics*, **58**, 20-29.
- Biot, M. A., 1956a, Theory of propagation of elastic waves in a fluid saturated porous solid. I. Low-frequency range: *J. Acoust. Soc. Amer.*, **28**, 168-178.
- Biot, M. A., 1956b, Theory of propagation of elastic waves in a fluid saturated porous solid. II. Higher-frequency range: *J. Acoust. Soc. Amer.*, **28**, 179-191.
- Dvorkin, J. and Nur, A., 1993, Dynamic poroelasticity: a unified theory with the squirt and the Biot mechanisms: *Geophysics*, **58**, in press.
- Gassmann, F., 1951, Über die elastizität porö medien: *Vierteljahrsschrift der Naturforschenden Gesellschaft in Zurich*, **96**, 1-23.
- Klimentos, T., and McCann, C., 1990, Relationships among compressional wave attenuation, porosity, clay content, and permeability in sandstones: *Geophysics*, **55**, 998-1014.
- Mavko, G., and Jizba, D., 1991, Estimating grain-scale fluid effects on velocity dispersion in rocks: *Geophysics*, **56**, 1940-1949.
- Mavko, G. M., and Nur, A., 1979, Wave attenuation in partially saturated rocks: *Geophysics*, **44**, 161-178.
- Mavko, G. M., and Nolen-Hoeksema, R., 1993, Estimating seismic velocities in partially saturated rocks: Submitted to *GEOPHYSICS*.
- Murphy, W. F., Winkler, K. W., and Kleinberg, R. L., 1986, Acoustic relaxation in sedimentary rocks: dependence on grain contacts and fluid saturation: *Geophysics*, **51**, 757-766.
- O'Connell, R. J., and Budiansky, B., 1977, Viscoelastic properties of fluid-saturated cracked-solids: *J. Geophys. Res.*, **82**, 5719-5725.
- Palmer, I. D., and Traviolia, M. L., 1980, Attenuation by squirt flow in undersaturated gas sands: *Geophysics*, **45**, 1780-1792.
- Zimmerman, R. W., 1991, *Compressibility of sandstones*: Elsevier science publ. Co., Inc.

CHAPTER 1

Relating P-Wave Attenuation to Permeability

ABSTRACT

To relate P-wave attenuation to permeability, we examine a three-dimensional (3-D) theoretical model of a cylindrical pore filled with viscous fluid and embedded in an infinite isotropic elastic medium. We calculate both attenuation and permeability as functions of the direction of wave propagation. Attenuation estimates are based on the squirt flow mechanism; permeability is calculated using the Kozeny-Carman relation.

We find that in the case when a plane P-wave propagates perpendicular to the pore orientation ($Q_{\delta=90^\circ}^{-1}$), attenuation is always higher than when a wave propagates parallel to this orientation ($Q_{\delta=0^\circ}^{-1}$). The ratio of these two attenuation values $\frac{Q_{\delta=90^\circ}^{-1}}{Q_{\delta=0^\circ}^{-1}}$ increases with an increasing pore radius and decreasing frequency and saturation.

By changing permeability, varying the radius of the pore, we find that the permeability-attenuation relation is characterized by a peak that shifts toward lower permeabilities as frequency decreases. Therefore, the attenuation of a low-frequency wave decreases with increasing permeability. We observe similar trend on relations between attenuation and permeability experimentally obtained on sandstone samples.

INTRODUCTION

The objective of this research is to theoretically detect the direction of maximum permeability using the attenuation dependence on the direction of wave propagation. Our model is based on the fact that both permeability and attenuation are intimately linked with the process of fluid motion in the rock. It is possible, therefore, to calculate attenuation and permeability separately and to find a relationship between them.

Most of the measurement, processing, and interpretation effort in the industry and in academia has concentrated on velocity rather than attenuation data, since the velocity measurements are more reliable and efficient. Recently, Gibson and Toksoz (1990) predicted the permeability variation with direction in fractured rocks from seismic velocity anisotropy.

We believe that attenuation rather than velocity is strongly correlated with permeability. Our argument is based on the experimental data of Han (1987) and Klimentos and McCann (1990) obtained on sandstone samples. Han's experiments resulted in the following empirical relation for P-wave velocity V_p :

$$V_p \text{ (km/s)} = 5.59 - 6.93\phi - 2.18C,$$

where ϕ is porosity and C is volumetric clay content. Klimentos and McCann show that for the attenuation coefficient α

$$\alpha \text{ (dB/cm)} = -0.132 + 3.15\phi + 24.1C.$$

These formulas indicate that unlike velocity, attenuation is strongly affected by clay content. On the other hand, Klimentos and McCann show strong systematic relation between clay content and permeability. We conclude that attenuation is the key factor in determining permeability.

To calculate the attenuation, we model the dynamic reaction of pore fluid to wave excitation depending on the angle of incidence of the wave measured from the pore's main axis. Our attenuation estimates are based on the squirt flow model that has been shown to be an important attenuation mechanism in rocks (Mavko and Nur, 1979; Murphy et al., 1986). We calculate the inverse of the attenuation quality factor Q^{-1} as the ratio of viscous energy dissipation during one period to the peak of stored energy in the rock. The permeability of the rock is also calculated with respect to the direction of wave propagation, using the Kozeny-Carman relation (Berryman and Blair, 1987).

We find that in the case when a wave propagates perpendicular to the preferred pore orientation ($Q_{\delta=90^\circ}^{-1}$), attenuation is always higher than when a wave propagates parallel to this orientation ($Q_{\delta=0^\circ}^{-1}$). The ratio of these two attenuation values $\frac{Q_{\delta=90^\circ}^{-1}}{Q_{\delta=0^\circ}^{-1}}$ increases with the increase of the pore's radius and the decrease of frequency and saturation.

THEORETICAL MODEL

We model a rock as an accumulation of identical typical cells with parallel pores inside, and assume that pores can be represented as infinitely long straight circular pipes partly filled with viscous fluid. The porosity of such a rock is introduced as the ratio of the pore cross-sectional area to the cross-sectional area of the cell. The saturation S is introduced as the ratio between the length occupied by the fluid L to the length of the pore H : $S = L/H$ (Figure 1.1). The pore's length H is a "free parameter" and has to be determined by matching theoretical to experimental data.

Fluid flow inside pores is induced by the radial displacements of the walls due to P-wave excitation. This viscous flow results in seismic energy dissipation and P-wave attenuation.

The attenuation is represented as the inverse of the quality factor Q^{-1} defined as:

$$Q^{-1} = \frac{\Delta W}{2\pi W}, \quad (1)$$

where ΔW is the energy loss per cycle of a harmonic excitation, and W is the elastic energy stored at maximum stress and strain (Mavko and Nur, 1979).

Pore Wall Displacements

We consider a rock containing N parallel identical pores, and estimate the deformation of a pore by employing the solution for the interaction between a P-wave and an infinitely long cylindrical borehole of radius a_0 embedded in an elastic medium (White, 1983). As a plane P-wave propagates along the $x - z$ plane at an angle δ to the z axis that is directed along the main axis of the pore (Figure 1.1), the spatial average radial displacement of the walls U_r is:

$$U_r = \frac{a_0}{2\mu} \left(1 - 2 \frac{V_s^2}{V_p^2} \cos^2 \delta\right) M,$$

where V_s is shear-wave velocity, V_p is compressional-wave velocity, μ is Lamé's constant, and M is normal stress in the direction of wave propagation. Here we assume

that

$$M = M_0 e^{i\omega(t - \frac{z \cos \delta}{V_p})},$$

where M_0 is the stress amplitude and ω is the angular frequency $\omega = 2\pi f$. This solution is employed in calculating the dynamics of pore fluid due to pore wall motion. Assuming that the wavelength is much larger than the characteristic length of a saturated interval inside the pore, we can neglect the variation of U_r with the z coordinate.

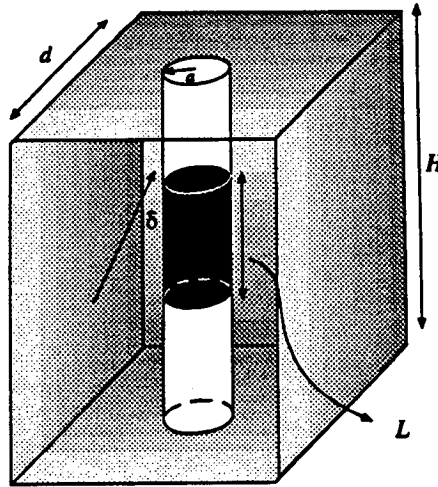


Fig. 1.1. An element with a single cylindrical pore of radius a_0 and length H embedded in an isotropic homogeneous block.

This assumption allows us to simplify the previous formula and to obtain the following expression for U_r :

$$U_r = \frac{a_0}{2\mu} \left(1 - 2 \frac{V_s^2}{V_p^2} \cos^2 \delta\right) M_0 e^{i\omega t}. \quad (2)$$

This expression doesn't account for the effects of fluid pressure on the walls of the pore. To consider this effect, equation (2) is modified by substituting the expression $[M_0 e^{i\omega t} - P_f(z, t)]$, where $P_f(z, t)$ is pore fluid pressure, instead of $M_0 e^{i\omega t}$. We introduced this expression using the idea of differential pressure commonly employed in rock physics (Mavko and Nur, 1979).

Assuming that P_f is a harmonic function of time: $P_f(z, t) = P_0(z) e^{i\omega t}$, we arrive at the following formula for the average radial displacements of the walls:

$$U_r = \frac{a_0}{2\mu} \left(1 - 2 \frac{V_s^2}{V_p^2} \cos^2 \delta\right) [M_0 - P_0(z)] e^{i\omega t}.$$

This formula gives the following expression for the radius of the pore as a function of t and z :

$$a = a_0 + a_0 s [M_0 - P_0(z)] e^{i\omega t}, \quad (3)$$

where

$$s = \frac{1}{2\mu} \left(1 - 2 \frac{V_s^2}{V_p^2} \cos^2 \delta\right). \quad (4)$$

Pore Fluid Dynamics

We examine the axisymmetrical flow of incompressible viscous pore fluid, induced by the radial displacement of the pore's walls in the cylindrical coordinate system (r, z) (Figure 1.1). We assume that the flow is laminar and parallel to the z direction. The equation of viscous fluid flow is:

$$\rho \frac{\partial u}{\partial t} = -\frac{\partial P_f}{\partial z} + \eta \left(\frac{\partial^2 u}{\partial r^2} + \frac{1}{r} \frac{\partial u}{\partial r} \right), \quad (5)$$

where u is fluid velocity in the z -direction; η is the dynamic viscosity of the fluid.

Consider a saturated interval inside the pore between $z = 0$ and $z = L$ that is surrounded by high compressibility gas at a given pressure. Counting the pressure from this level, we arrive at the boundary conditions

$$P_f(0, t) = P_f(L, t) = 0. \quad (6)$$

The no-slip boundary condition for velocity $u(z, r, t)$ is $u(z, a, t) = 0$. Given small deformation of the pore ($a \approx a_0$), we obtain the following equation:

$$u(z, a_0, t) = 0. \quad (7)$$

Assuming that pressure and velocity of the fluid are harmonically time-dependent ($P_f = P_0 e^{i\omega t}$, $u = u_0 e^{i\omega t}$), and substituting these expressions into equation (5), we obtain the relation:

$$\frac{\partial^2 u_0}{\partial r^2} + \frac{1}{r} \frac{\partial u_0}{\partial r} - \frac{i\omega}{\nu} u_0 = \frac{1}{\rho\nu} \frac{\partial P_0}{\partial z}, \quad (8)$$

where $\nu = \eta/\rho$.

The solution of ordinary differential equation (8) with boundary condition equation (7) is:

$$u_0(r, z) = \frac{1}{i\omega\rho} \frac{\partial P_0}{\partial z} \left[\frac{J_0(\Lambda r)}{J_0(\Lambda a_0)} - 1 \right], \quad (9)$$

where J_0 is Bessel's function of the first kind, and $\Lambda = \sqrt{-i\omega/\nu}$. Taking the derivative of equation (9) with respect to r and using the relation $J_0'(\Lambda r) = -J_1(\Lambda r)$ we arrive at:

$$\frac{\partial u_0}{\partial r} = -\frac{1}{i\omega\rho} \frac{\partial P_0}{\partial z} \frac{\Lambda J_1(\Lambda r)}{J_0(\Lambda a_0)}. \quad (10)$$

The continuity equation for axisymmetrical incompressible flow in the cylindrical coordinate system (r, z) is:

$$\frac{1}{r} \frac{\partial}{\partial r} (r\tilde{v}) + \frac{\partial u}{\partial z} = 0, \quad (11)$$

where \tilde{v} is the radial velocity component of fluid, which satisfies the boundary conditions:

$$\tilde{v}_{r=a} = \frac{\partial a}{\partial t}.$$

Multiplying equation (11) by r and integrating in the r direction from 0 to a , we obtain the equation:

$$\int_0^a \frac{\partial}{\partial r}(r\tilde{v}) dr = - \int_0^a r \frac{\partial u}{\partial z} dr. \quad (12)$$

The left-hand side of equation (12) is:

$$\begin{aligned} r\tilde{v}|_0^a &= a \frac{\partial a}{\partial t} \\ &\approx i\omega a_0^2 s [M_0 - P_f(z)] e^{i\omega t}. \end{aligned}$$

The right-hand side of equation (12) is:

$$\begin{aligned} &-e^{i\omega t} \int_0^{a_0} \frac{\partial u_0}{\partial z} r dr \\ &\approx \frac{1}{i\omega\rho} \frac{\partial^2 P_0}{\partial^2 z} \left[\frac{a_0^2}{2} - \frac{a_0 J_1(\Lambda a_0)}{\Lambda J_0(\Lambda a_0)} \right] e^{i\omega t}. \end{aligned}$$

Equating both sides and dropping $e^{i\omega t}$ we arrive at

$$\frac{\partial^2 P_0}{\partial^2 z} - \beta^2 P_0 + \beta^2 M_0 = 0, \quad (13)$$

where

$$\beta^2 = \frac{2\omega^2 \rho s}{1 - \frac{2J_1(\Lambda a_0)}{(\Lambda a_0)J_0(\Lambda a_0)}}.$$

The general solution of equation (13) is:

$$P_0 = C_1 e^{\beta z} + C_2 e^{-\beta z} + M_0,$$

where C_1 and C_2 are constants. Applying boundary conditions (6), we get:

$$P_0 = M_0 \left[\frac{e^{-\beta L} - 1}{e^{\beta L} - e^{-\beta L}} e^{\beta z} - e^{-\beta z} - \frac{e^{-\beta L} - 1}{e^{\beta L} - e^{-\beta L}} e^{-\beta z} + 1 \right]. \quad (14)$$

The derivative from equation (14) with respect to z yields the following relation:

$$\frac{\partial P_0}{\partial z} = \beta M_0 \left[\frac{e^{-\beta L} - 1}{e^{\beta L} - e^{-\beta L}} e^{\beta z} + e^{-\beta z} + \frac{e^{-\beta L} - 1}{e^{\beta L} - e^{-\beta L}} e^{-\beta z} \right]. \quad (15)$$

The viscous energy dissipation ΔW is defined as:

$$\Delta W = \frac{\eta}{2} \int_v \int_T \left\| \frac{\partial u}{\partial r} \right\|^2 dv dt,$$

where T is the period, v is the fluid volume.

The dissipation in N identical pores is:

$$\Delta W_N = \frac{N\eta}{2} \int_0^T dt \int_0^{2\pi} d\theta \int_0^L dz \int_0^{a_0} \left\| \frac{\partial u}{\partial r} \right\|^2 r dr,$$

where θ is the azimuth angle.

The peak of stored energy in a cell containing N parallel pores is (Appendix A):

$$W = \frac{VM_0^2}{2\tilde{m}} - \frac{\pi}{2\tilde{m}} NLa_0^2 \sin^2 \delta \operatorname{Re}(M^* \tilde{P}_f) + \frac{\pi}{2} NHa_0^2 M_0 s \left(\sin^2 \delta + \frac{\lambda}{\tilde{m}} \cos^2 \delta + \frac{\lambda}{\tilde{m}} \right) \operatorname{Re}(M_0 - \tilde{P}_f).$$

Now using equation (1) we arrive at the following formula for Q^{-1} :

$$Q^{-1} = \frac{1}{\pi} \frac{\frac{N\eta}{2} \int_0^T dt \int_0^{2\pi} d\theta \int_0^L dz \int_0^{a_0} \left\| \frac{\partial u}{\partial r} \right\|^2 r dr}{\frac{VM_0^2}{\tilde{m}} - \frac{\pi}{\tilde{m}} NLa_0^2 \sin^2 \delta \operatorname{Re}(M^* \tilde{P}_f) + \pi NHa_0^2 M_0 s \left(\sin^2 \delta + \frac{\lambda}{\tilde{m}} \cos^2 \delta + \frac{\lambda}{\tilde{m}} \right) \operatorname{Re}(M_0 - \tilde{P}_f)}.$$

NUMERICAL ANALYSIS

In this section, we relate attenuation to permeability by keeping fluid properties (water) and porosity (10%) unchanged, and concentrating on the effects of pore size, frequency, saturation, and incident angle.

The incident angle δ is measured from the pore's main axis. We define the ratio of attenuations (R_δ) as the ratio of the attenuation at $\delta = 90^\circ$ to the attenuation at $\delta = 0^\circ$: $R_\delta = \frac{Q_{\delta=90^\circ}^{-1}}{Q_{\delta=0^\circ}^{-1}}$.

In Figure 1.2, we plot $\log Q^{-1}$ versus $\log f$ for constant radius $a_0 = 10\mu\text{m}$ and for a full saturation with the pore length $H = L = 4\text{mm}$. The curves are plotted for $\delta = 0^\circ$, 45° , and 90° . For lower frequencies, the attenuation increases with frequency and depends strongly on the incident angle. At higher frequencies, attenuation decreases with frequency and the dependence on the incident angle becomes negligible.

Figure 1.3 shows $\log Q^{-1}$ versus $\log a_0$ at a constant frequency $f = 5\text{ kHz}$ and with $L = H = 4\text{ mm}$. The curves are plotted for: $\delta = 0^\circ$, 30° , 60° , and 90° . Attenuation increases with the increasing radius and depends weakly on the incident angle at small radii. At larger radii, attenuation decreases with the increasing radius and its dependence on the incident angle becomes stronger.

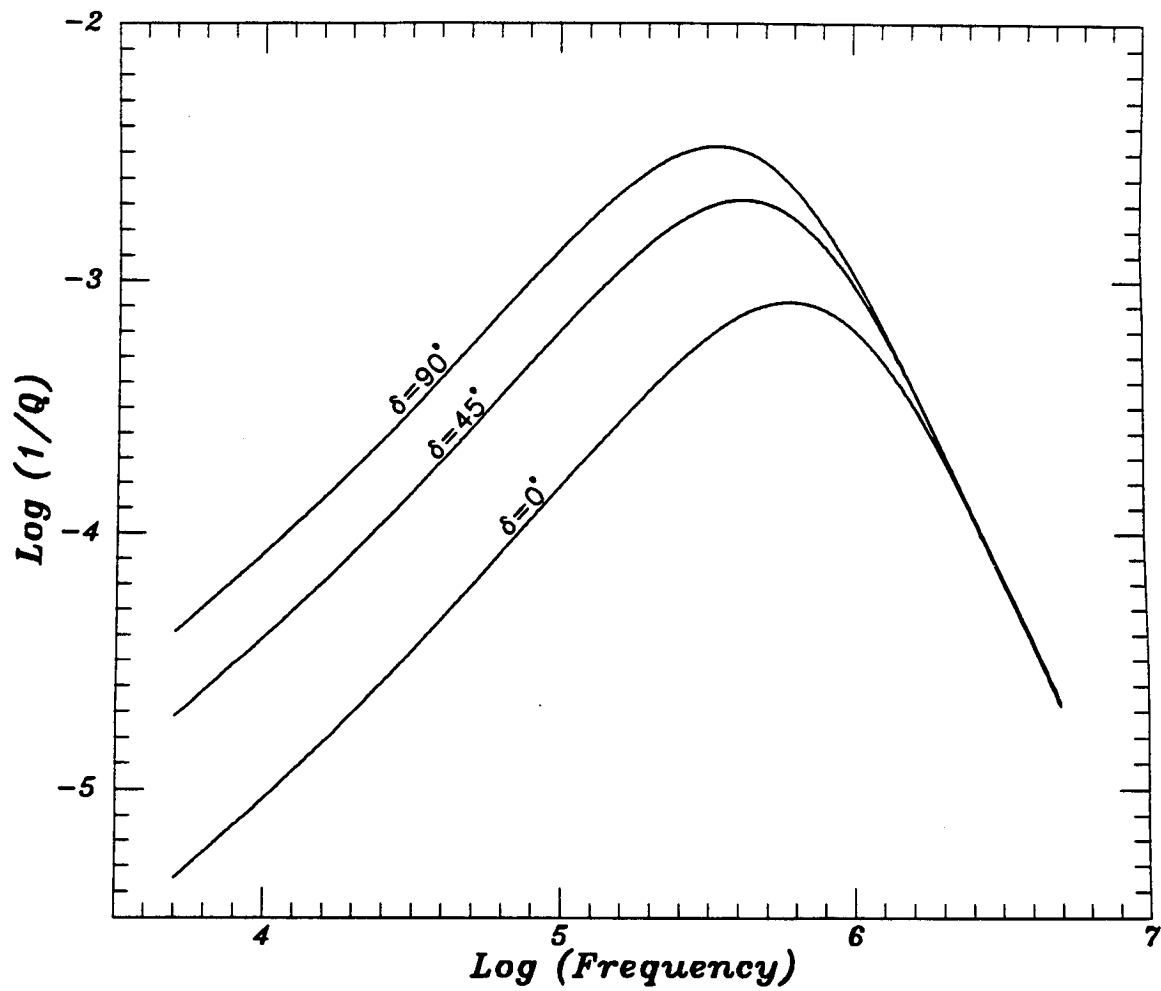


Fig. 1.2. The plot of $\text{Log}Q^{-1}$ versus $\text{Log}f$; the curves are plotted for $\delta = 0^\circ$, 45° , and 90° .

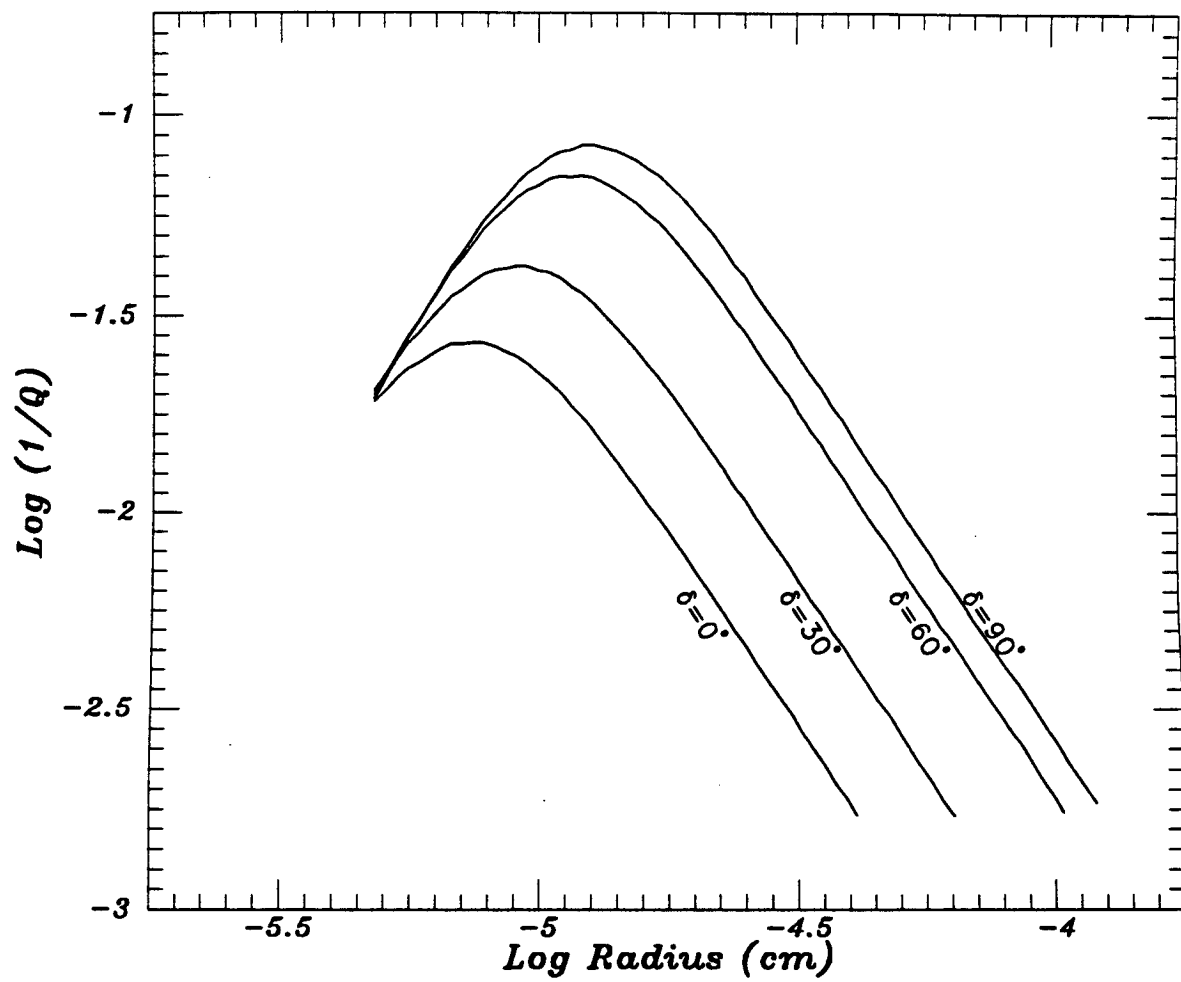


Fig. 1.3. $\text{Log}Q^{-1}$ is plotted versus $\text{Log}a_0$; the curves are plotted for: $\delta = 0^\circ, 30^\circ, 60^\circ,$ and 90° .

The peaks in attenuations shown in Figures 1.2 and 1.3 can be explained in terms of the variation of the shear stresses and pressure within the fluid as frequency or the pore radius change. At small frequencies (or large radii) the fluid is relaxed and the shear stress within the fluid is small, which results in small attenuation. As frequency increases (or the radius decreases), the shear stress increases resulting in high attenuation. At very high frequencies (or small radii) the fluid is unrelaxed with high pressure, reducing the displacement of the pore's wall and resulting in a small attenuation.

Figure 1.4 shows $\log Q^{-1}$ versus saturation at a constant frequency $f = 1$ MHz, $a_0 = 5\mu\text{m}$, and $H = 10$ mm. The curves are plotted for $\delta = 0^\circ, 45^\circ$, and 90° .

The peaks in attenuation shown in Figure 1.4 can be explained as follows: when the saturation is small (length of fluid drop is small), the shear stress within the fluid is small, resulting in small attenuation. As saturation increases, the shear stress increases sharply and attenuation reaches its peak. Further increase in saturation builds up fluid pressure that results in the unrelaxed mode of fluid motion leading to a smooth decrease in attenuation.

Figure 1.5 shows the effects of frequency, the pore radius, and saturation on the $Q^{-1} - \delta$ relation. The solid curve is plotted for full saturation using the following parameters: $a_0 = 1\mu\text{m}$, $f = 200$ kHz, and $H = L = 10$ mm. R_δ in this case is approximately 1.5.

Each of the other curves is obtained by changing only one of the above-mentioned parameters. The dotted line shows the effects of the increasing pore radius (up to $100\mu\text{m}$). In this case R_δ increases to about 5. R_δ for the dashed curve is about 9.1, which is due to the decrease of frequency down to 200 Hz. The dash-dot curve shows the effects of saturation decreasing down to 20%. R_δ in this case is about 8.4.

Figure 1.5 shows that for all cases, the attenuation increases with an increasing incident angle. Increasing frequency or saturation and the decreasing pore radius result in decreasing R_δ .

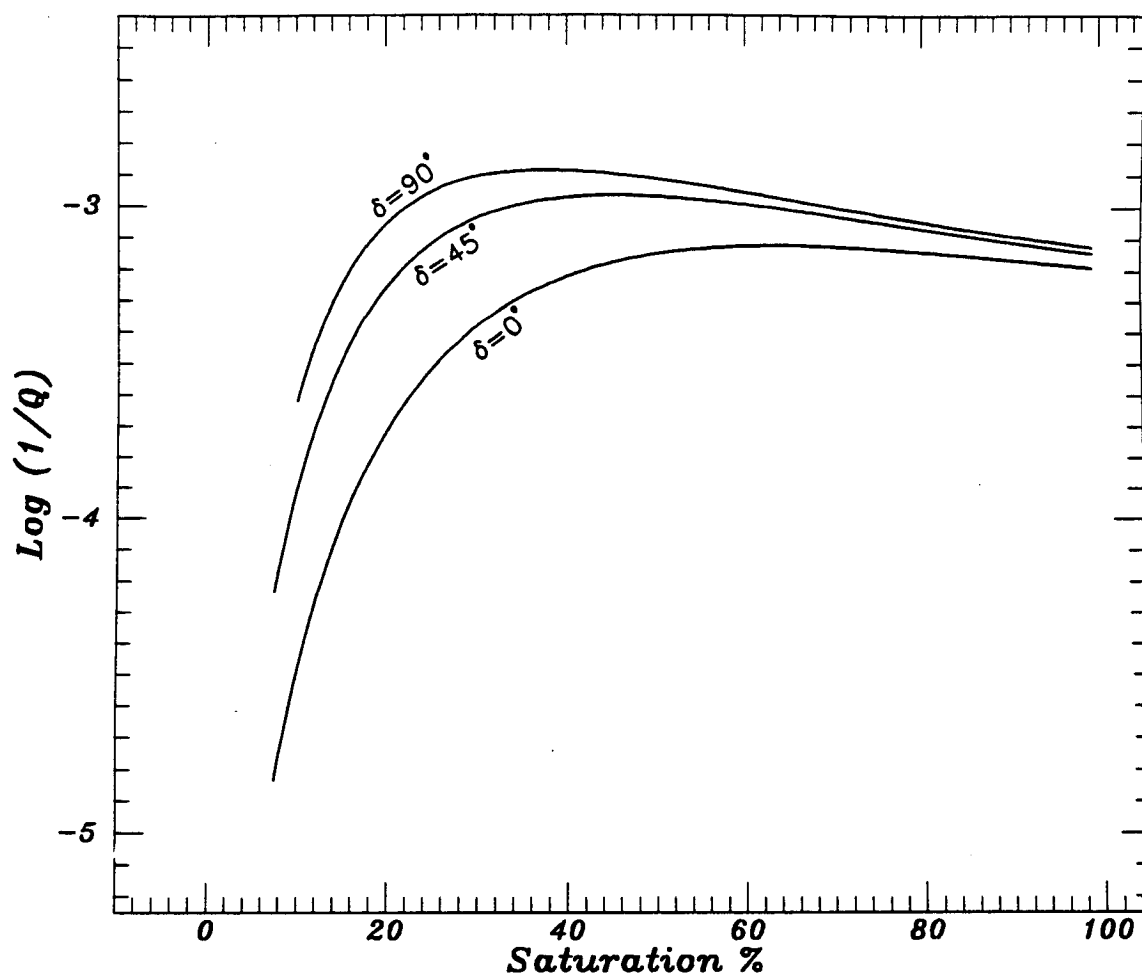


Fig. 1.4. $\text{Log}Q^{-1}$ versus saturation; the curves are plotted for $\delta = 0^\circ$, 45° , and 90° .

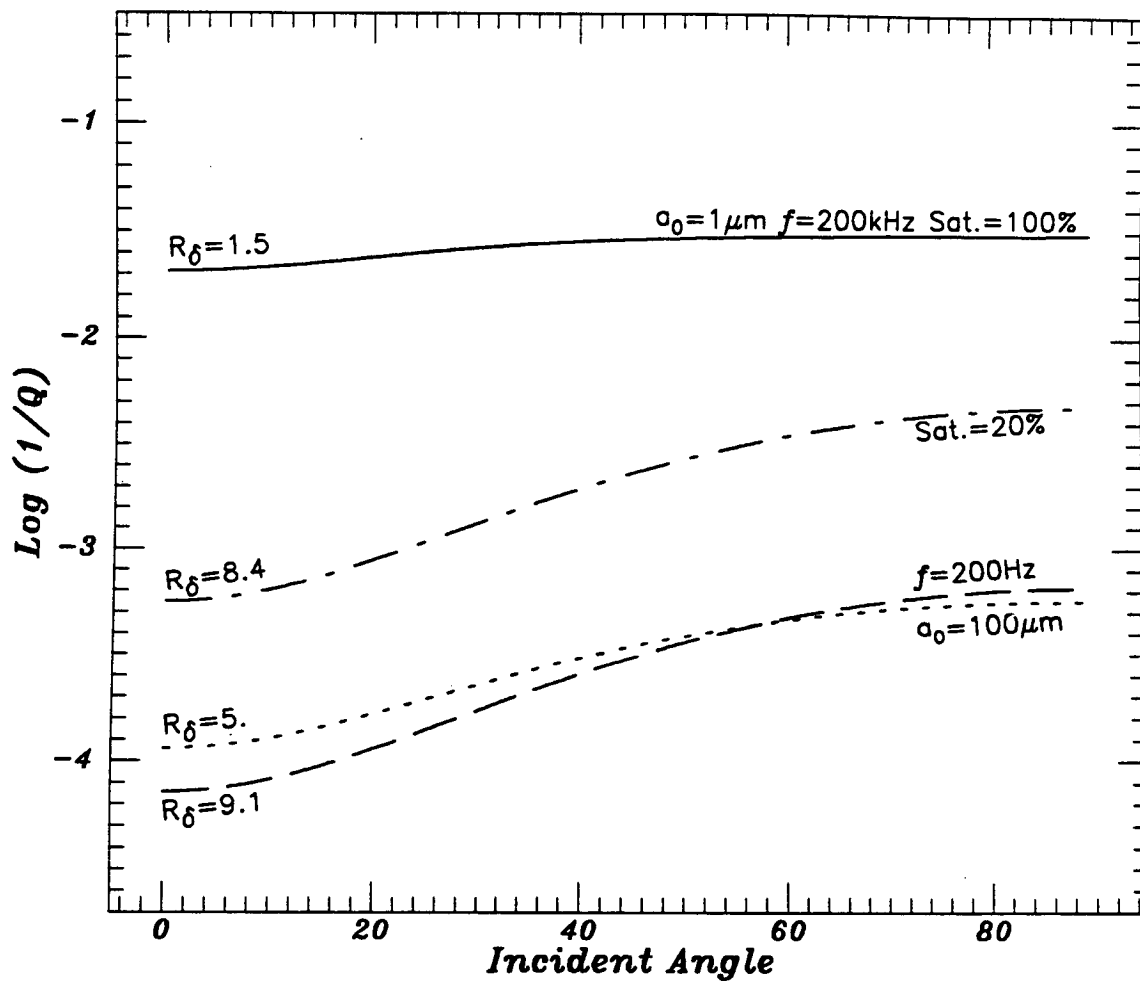


Fig. 1.5. The effects of frequency, pore's radius, and saturation on the $Q^{-1}-\delta$ relation. The parameters are shown on the curves.

Figure 1.6 shows Q^{-1} versus permeability for full saturation with the pore length $H = 1$ mm. The curves are plotted for three frequencies: $f = 5$ kHz, 50 kHz, and .5 MHz. The effect of frequency on the attenuation-permeability relation manifests itself in shifting the peak towards lower permeabilities as frequency decreases. In this example, we change permeability while keeping porosity constant by increasing the number of pores and reducing their radii (Appendix C).

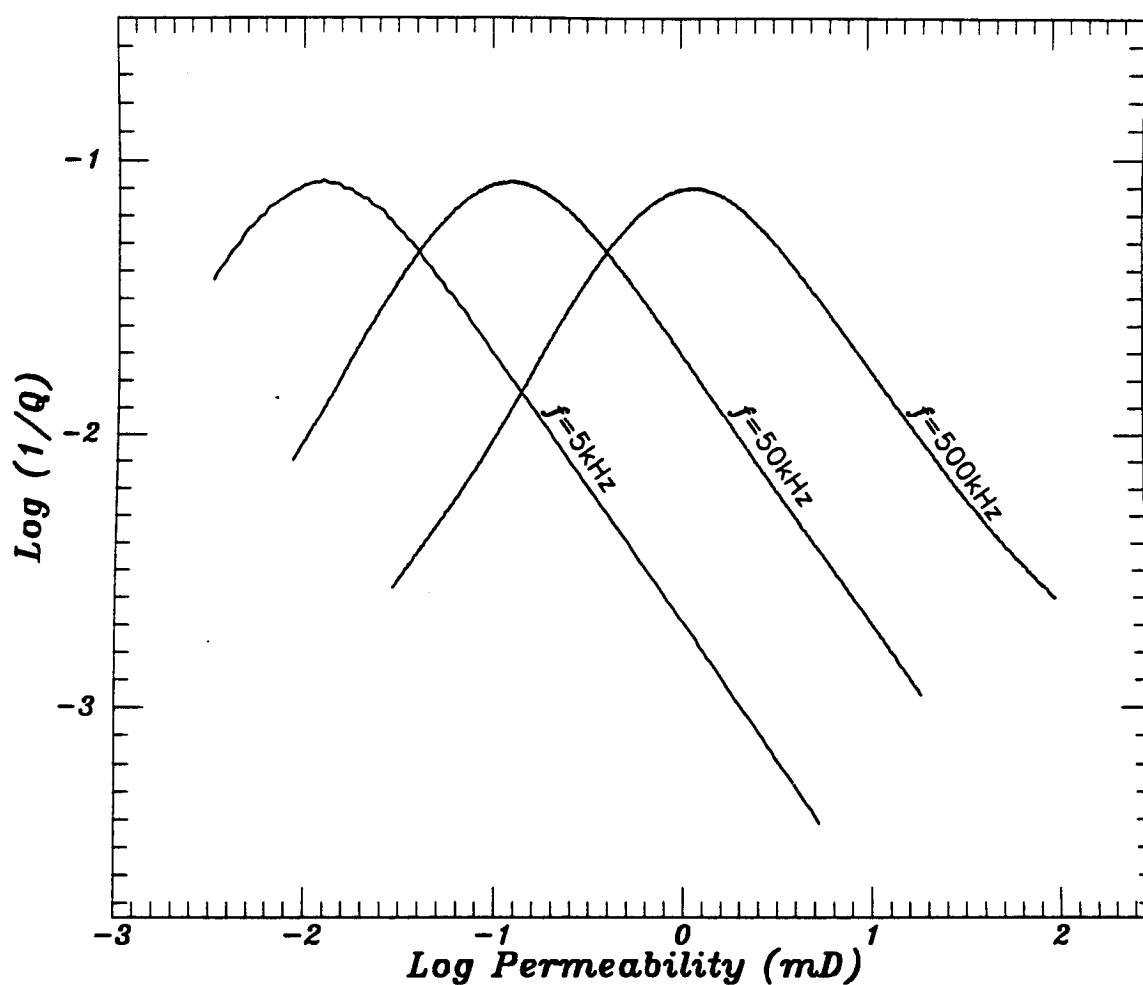


Fig. 1.6. $\text{Log}Q^{-1}$ versus $\text{Log}k$. The curves are plotted for three frequencies: $f = 5$ kHz, 50 kHz, and .5 MHz.

COMPARISON WITH DATA

A rock with isotropic permeability can be represented by pores having all possible orientations. Each pore contributes to the overall attenuation depending on the angle between its main axis and the direction of the propagation. We approximate the attenuation analysis by representing such a rock with a typical cell having pores that are aligned at a certain angle with respect to the direction of wave propagation. This approximation is reasonable within our analysis since the goal of this paper is to elucidate general trends rather than to find exact values of attenuation as a function of different parameters. Indeed, our analysis has shown that varying the orientation of a pore changes the magnitude of attenuation but does not change qualitative trends in the attenuation behavior.

We model the experimental results of Klimentos and McCann (1990) where an attenuation-permeability relation was obtained on 17 water-saturated sandstone samples of a constant porosity of approximately 15%. Klimentos and McCann have concluded that attenuation systematically decreases with increasing permeability.

In modeling this experiment, we used $f = 1$ MHz and saturation $S = 1$. We have also assumed that $\delta = 90^\circ$ and $L = H = .6$ mm. We changed the permeability while keeping the porosity unchanged, by increasing the number of pores and decreasing their radii, so that the total pore volume was constant (Appendix C). The elastic properties of the rock frame were chosen from the experimental P-velocity measurements.

Figure 1.7 shows the attenuation coefficient normalized by its maximum theoretical value versus permeability according to our model (solid line), and the experimental data (asterisks) normalized by its maximum experimental value. Our theoretical results show that attenuation has a sharp peak at low permeability.

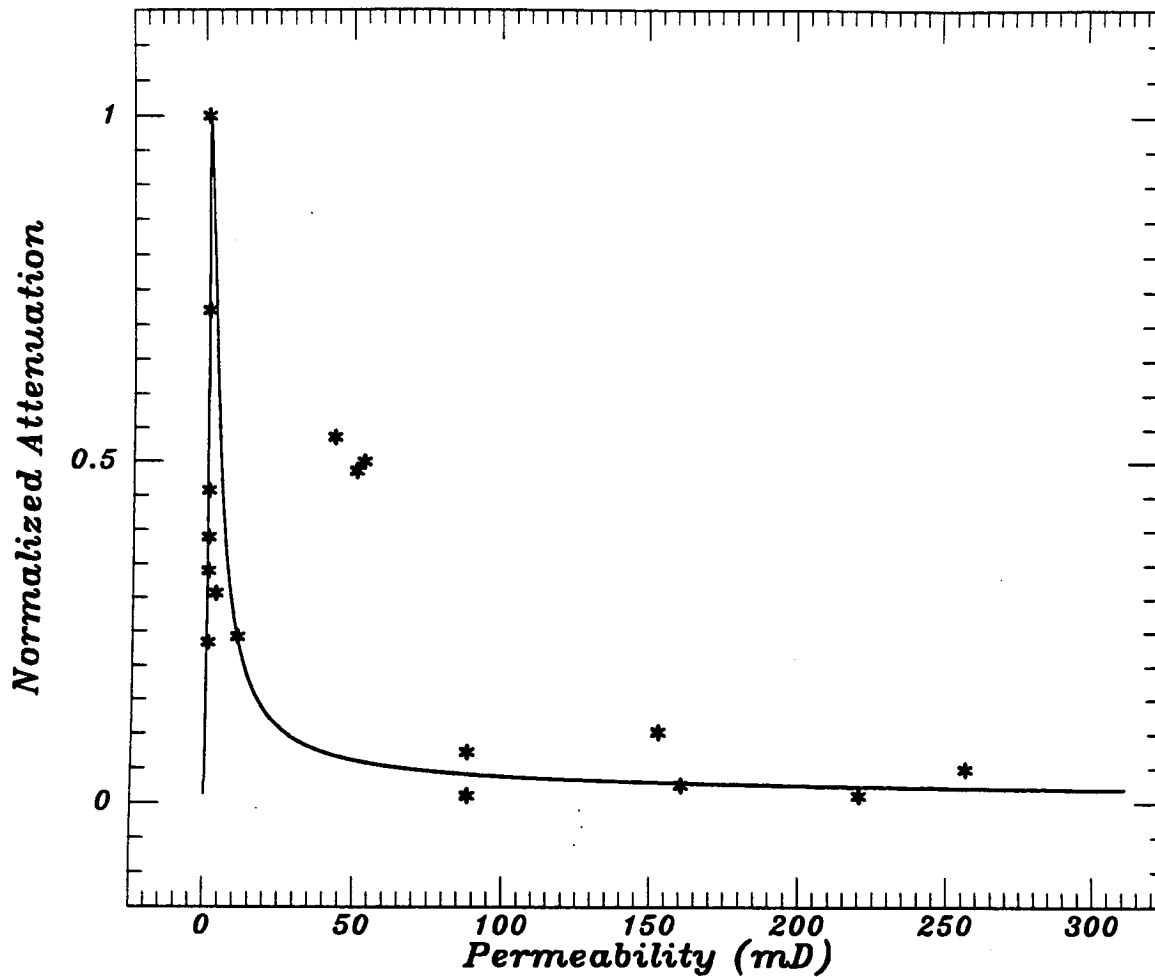


Fig. 1.7. Permeability versus attenuation coefficient α normalized according to its maximum value for $f=1\text{MHz}$, pore's radius $a_0 = 55\mu\text{m}$, and constant porosity $\phi = 15\%$. Asterisks represent experimental data from Klimentos and McCann (1990) for 17 sandstone samples of a constant porosity about 15% and frequency 1 MHz. Data was normalized according to its maximum value.

To investigate the effects of frequency on the permeability-attenuation relation, we analyze the experimental results of Lucet (1989) where attenuation has been measured as a function of the applied external stress for five samples of Fontainebleau sandstones (99% quartz) with known permeabilities and porosities. The attenuation of the extensional waves Q_e^{-1} was measured for sonic frequencies $f \approx 1.14 - 6.5$ kHz. The attenuation of compressional waves Q_p^{-1} was also measured at ultrasonic frequencies $f \approx 5$ MHz.

We calculated Q_p^{-1} for the sonic frequency range from the available data of Q_e^{-1} by using the following relation (Winkler, 1979):

$$(1 - \nu)(1 - 2\nu) Q_p^{-1} \approx (1 + \nu) Q_e^{-1} - 2\nu(2 - \nu) Q_s^{-1},$$

where ν is the Poisson ratio, and Q_s^{-1} is the attenuation of the shear waves.

Tables 1.1 and 1.2 summarize the experimental data for both ultrasonic and sonic frequencies when the applied external stress is 5 MPa.

Figure 1.8 shows the experimental values of Q_p^{-1} for both sonic (S) and ultrasonic (U) frequencies versus permeability. In both cases, we Normalized the attenuation data by the maximum attenuation values separately for sonic and ultrasonic frequencies.

The results show that attenuation decreases with increasing permeability for low-frequency waves. For ultrasonic frequencies, the attenuation is small for both low and high permeabilities and reaches a maximum at $k \approx 1$ d.

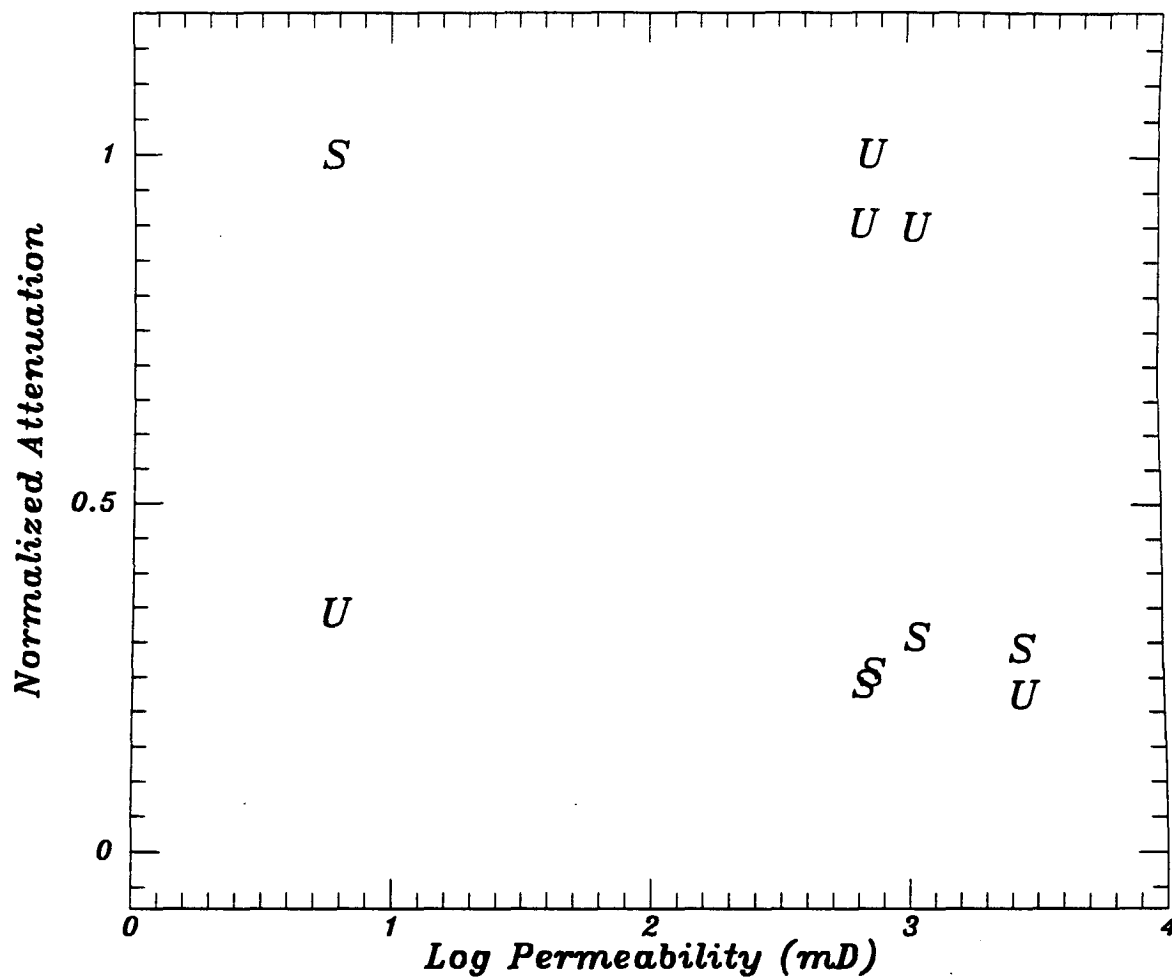


Fig. 1.8. The measured and the estimated Q_p^{-1} (normalized by their maximum) versus permeability for five samples of Fontainebleau sandstones. Letters *U* and *S* denote the experimental data for ultrasonic and sonic frequencies respectively. Data obtained from Lucet (1989).

Table 1.1. Permeabilities and the corresponding attenuations of ultrasonic frequencies when the applied external stress is 5 MPa (Lucet, 1989).

Sample #	ϕ %	k (mD)	$\text{Log } Q_{10P}^{-1}$	Q_p^{-1} (Normalized)
A6	6.7	6	-1.881	0.342
F60	13.6	670	-1.460	0.902
F5	14.8	720	-1.415	1.000
F64	15.5	1080	-1.462	0.897
A8	22	2800	-2.065	0.224

Table 1.2. Permeabilities and the corresponding attenuations of sonic frequencies when the applied external stress is 5 MPa (Lucet, 1989).

Sample #	ν	$\text{Log}_{10} Q_s^1$	$\text{Log}_{10} Q_e^1$	$^* \text{Log}_{10} Q_p^1$	$Q_p^1(\text{Normalized})$
A6	.25	-1.04	-0.903	-0.689	1.000
F60	.05	-1.70	-1.362	-1.311	0.239
F5	.08	-1.67	-1.362	-1.281	0.256
F64	.05	-1.62	-1.255	-1.202	0.307
A8	.18	-1.51	-1.380	-1.262	0.290

CONCLUSIONS

We relate P-wave attenuation to permeability by considering a theoretical model of a cylindrical pore filled with viscous fluid, embedded in an infinite isotropic elastic medium. Attenuation estimates are based on the squirt flow mechanism. Both attenuation and permeability are calculated as functions of the direction of wave propagation. The permeability-attenuation relation is characterized by a peak which shifts toward lower permeabilities as frequency decreases. A similar trend can be observed in some experimental relations between attenuation and permeability obtained on sandstone samples. In the case when a plane P-wave propagates perpendicular to the pore orientation, attenuation is always higher than when a wave propagates parallel to this orientation. The ratio of these two attenuation values increases with increasing pore radius and decreasing frequency or saturation.

ACKNOWLEDGMENTS

We thank G. Mavko, T. Mukerji, and J. P. Blangy for their helpful comments and suggestions. This work was sponsored by SAUDI ARAMCO and DOE.

REFERENCES

- Berryman, J. G., and Blair, S. C., 1987, Kozeny-Carman relations and image processing methods for estimating Darcy's constant: *J. Appl. Phys.*, **62**, 2221-2228.
- Gibson, R. L. and Toksöz, M. N., 1990, Permeability estimation from velocity anisotropy in fractured rock: *JGR*, **95**, 15643-15655.
- Han, D., 1987, Effect of porosity and clay content on acoustic properties of sandstones and unconsolidated sediments: Ph.D. Thesis, Stanford University.
- Klimentos, T., and McCann, C., 1990, Relationships among compressional wave attenuation, porosity, clay content, and permeability in sandstones: *Geophysics*, **55**, 998-1014.
- Lucet, N., 1989, Vitesse et atténuation des ondes élastiques soniques et ultrasoniques dans les roches sous pression de confinement: Thèse de Doctorat de l'Université Paris 6.
- Mavko, G. M., and Nur, A., 1979, Wave attenuation in partially saturated rocks: *Geophysics*, **44**, 161-178.
- Murphy, W. F., Winkler, K. W., and Kleinberg, R. L., 1986, Acoustic relaxation in sedimentary rocks: dependence on grain contacts and fluid saturation: *Geophysics*, **51**, 757-766.
- White, J. E., 1983, *Underground sound*: Elsevier science publishers.
- Winkler, K. W., 1979, Effects of pore fluids and frictional sliding on seismic attenuation: Ph.D. Thesis, Stanford University.

Appendix A- the Peak of Stored Energy

To find the peak of stored energy in the rock during one period, we divide the rock into small rectangular elements each containing N pores. We assume that a cross-section of an element perpendicular to pore orientation is a square of dimensions $(d \times d)$. The length of the element in the direction parallel to the pore is H (Figure 1.9a). As the wave propagates through the element, the resulting displacement of its surfaces along the direction of propagation U is

$$U = U_0 e^{i(\omega t + \psi)}.$$

If the phase difference ψ between the applied stress and the resulting strain is small (small attenuation), then the peak stored energy is (Mavko and Nur, 1979):

$$\begin{aligned} W &\simeq \frac{1}{2} \int \int_{\Sigma} M_0 U_0 ds \\ &\simeq \operatorname{Re} \frac{1}{2} \int \int_{\Sigma} M^* U ds, \end{aligned}$$

where the integration is performed on the external surface Σ of the element; M^* is the complex conjugate of M ; and Re denotes the real part.

To calculate this integral, we use the reciprocity theorem (Mavko and Nur, 1979), and introduce an artificial element with N identical pores, such that the external stress M^* is applied to both the external and internal surfaces (Figure 1.9b). We assume that strain is uniform everywhere in the element and equal to $\frac{M^*}{\tilde{m}}$ along the direction of wave propagation, where $\tilde{m} = \lambda + 2\mu$, λ and μ are Lamé's constants. In this case, the artificial element deforms as if there are no pores inside.

The actual stress M due to a wave propagating in the $(x-z)$ plane at an angle δ to the z axis results in external and internal displacements. We assume that the external surface displacement U takes place only along the direction of wave propagation and that the pore's displacement U_r is radial in the $(x-y)$ plane (Figure 1.9a).

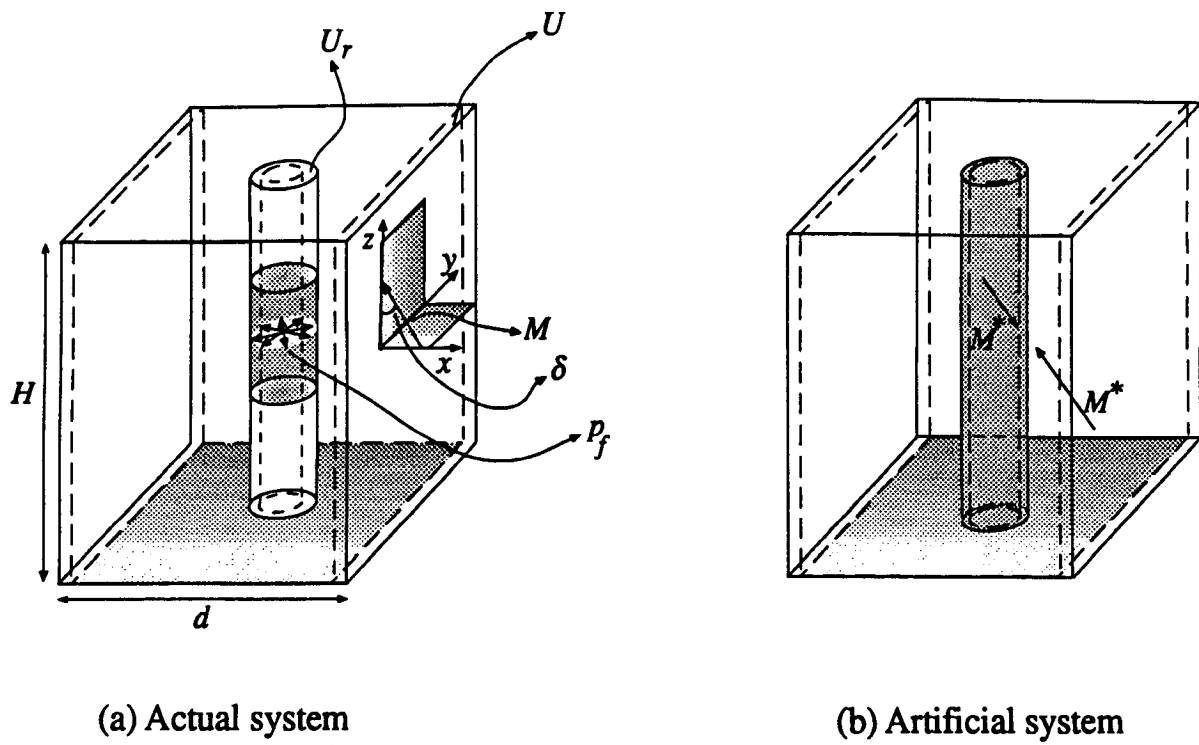


Fig. 1.9. (a) Stresses and displacements in the actual element; (b) an artificial element containing a single pore.

Work done by the actual set of tractions

The work done by the actual set of tractions through the displacements of the artificial element is divided into two parts. The first part represents the work W_0 done by the external stress M of the actual element through the strain of the artificial element $\frac{M^*}{\bar{m}}$ integrated over the total volume:

$$W_0 = \int_V M \frac{M^*}{\bar{m}} dv = \frac{V}{\bar{m}} M_0^2,$$

where V is the element's volume.

The second part represents the work W_{c1} done by the fluid pressure P_f in the actual element through the strain of the artificial element $\frac{M^*}{\bar{m}}$ integrated over the pore's surface which is occupied by the fluid.

From Figure 1.10a, the component of fluid pressure along the x -direction is $P_f \cos \theta$, where θ is the azimuth. We do not consider the normal strain along the z -direction since it is parallel to the pore's axis (Figure 1.10b). The displacement along the x -direction due to strain ϵ_{xx}^* is $2\epsilon_{xx}^* a_0 \cos \theta$. Thus the work ΔW_{c1} done on a small area $da dz$ of the pore's surface in the artificial system is

$$\begin{aligned} \Delta W_{c1} &= -2P_f \cos \theta^2 \epsilon_{xx}^* a_0 da dz \\ &= -2P_f \cos \theta^2 \epsilon_{xx}^* a_0^2 d\theta dz, \end{aligned}$$

where $da = a_0 d\theta$.

Therefore, the total work done by fluid pressure through the displacements of the pore's surface in the artificial system is:

$$\begin{aligned} W_{c1} &= \int_0^L dz \int_{-\frac{\pi}{2}}^{\frac{\pi}{2}} \Delta W_{c1} d\theta \\ &= -\frac{\pi}{\bar{m}} a_0^2 L M^* \sin^2 \delta \bar{P}_f, \end{aligned}$$

where P_f is the average fluid pressure.

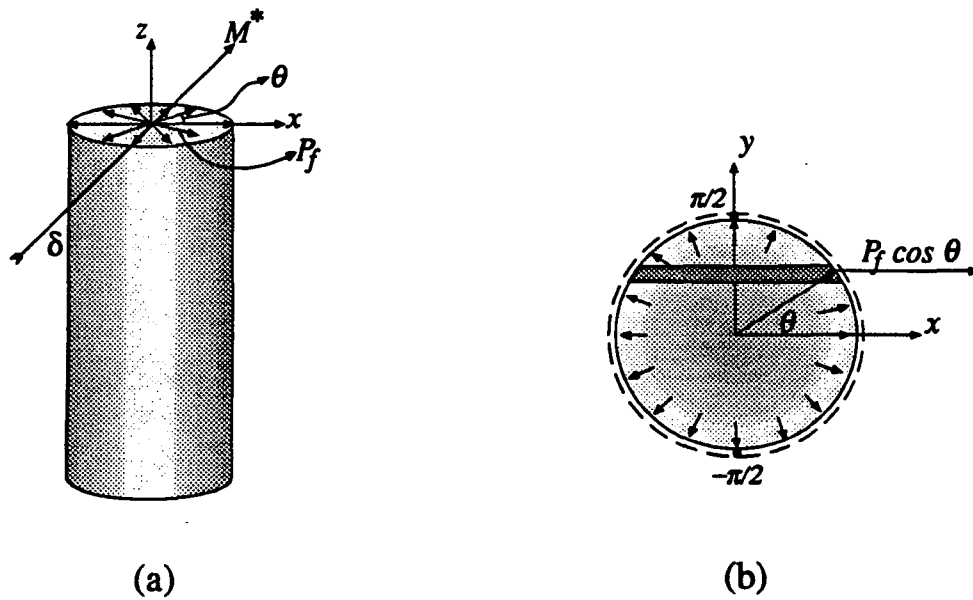


Fig. 1.10. (a) The actual system forces acting on the artificial element; (b) artificial system showing the components of fluid pressure and the strain in the x -direction.

Work done by the artificial set of tractions

The work done by the artificial set of tractions through the displacements of the actual element is divided into two parts.

The first part represents the work W_{c2} done by the stress M^* in the artificial element through the actual radial displacement of the pore's wall U_r integrated over the total pore's surface area (Figure 1.11a). Only one component of the stress, which is normal to the surface of the pore, will contribute to W_{c2} .

Let $\hat{n}(\theta)$ represent a unit vector that is perpendicular to the pore's surface at a point on the pore's surface which is rotated by an angle θ from the x -axis. By transforming the stresses to a new coordinate system x' , y' , and z , which is rotated by an angle θ about the z -axis, we have (Figure 1.11b):

$$\sigma_n^* = \sigma_{x'x'}^* = \sigma_{xx}^* \cos^2 \theta + \sigma_{yy}^* \sin^2 \theta.$$

Stresses $\sigma_{y'y'}$ and σ_{zz} will not contribute to the work since they act perpendicular to the pore's wall displacement. Thus the work done on a small surface element $da dz$ whose normal makes an angle θ with the x -axis is

$$-\sigma_n^*(\theta) U_r da dz.$$

The total work done on the pore's surface area is:

$$\begin{aligned} W_{c2} &= -2 \int_0^H \int_{-\frac{\pi}{2}}^{\frac{\pi}{2}} \sigma_n^*(\theta) U_r da dz \\ &= -2HU_r a_0 \int_{-\frac{\pi}{2}}^{\frac{\pi}{2}} (\sigma_{xx}^* \cos^2 \theta + \sigma_{yy}^* \sin^2 \theta) d\theta \\ &= -\pi H a_0^2 M_0 s \left(\sin^2 \delta + \frac{\lambda}{\bar{m}} \cos^2 \delta + \frac{\lambda}{\bar{m}} \right) (M_0 - \tilde{P}_f), \end{aligned}$$

where s is defined by equation (4).

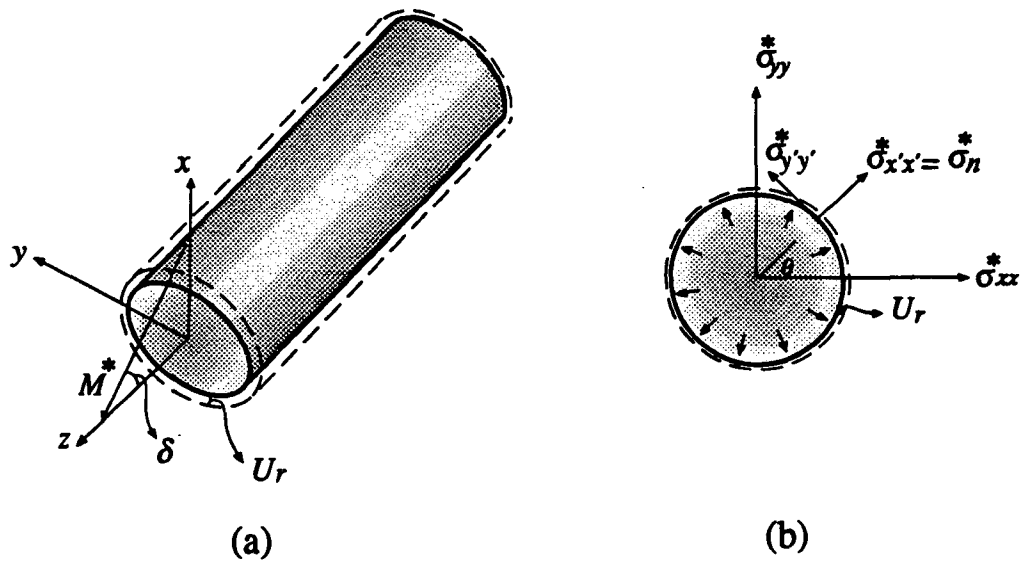


Fig. 1.11. (a) Artificial tractions acting on the actual system; (b) the normal component of stress along the direction of the wall's displacement.

The second part represents the work W done by the stress M^* in the artificial element through the actual external surface displacement along the direction of the wave propagation, integrated over the external surface of the element:

$$\int \int_{\Sigma} M^* U ds.$$

Applying the reciprocity theorem we have:

$$\int \int_{\Sigma} M^* U ds = W_0 + W_{c1} - W_{c2}.$$

The peak of stored energy due to a single pore is:

$$\frac{1}{2} Re \int \int_{\Sigma} M^* U ds = \frac{1}{2} Re [W_0 + W_{c1} - W_{c2}].$$

We can write this equation as $W = W_0 + W_c$ where $W_c = W_{c1} - W_{c2}$. The term W represents the stored energy of the element that includes the pore, while W_0 is the stored energy for the total volume without a pore, and W_c is the increment in the stored energy due to the pore.

For N parallel pores, we modify W_c by $W_{cN} = NW_c$. Substituting the expressions for W_0, W_{cN} into the previous formula, we find the peak of stored energy in a cell containing N pores as:

$$\begin{aligned} W = & \frac{VM_0^2}{2\tilde{m}} - \frac{\pi}{2\tilde{m}} NLa_0^2 \sin^2 \delta Re(M^* \tilde{P}_f) \\ & + \frac{\pi}{2} NHa_0^2 M_0 s \left(\sin^2 \delta + \frac{\lambda}{\tilde{m}} \cos^2 \delta + \frac{\lambda}{\tilde{m}} \right) Re(M_0 - \tilde{P}_f). \end{aligned}$$

Appendix B- Stresses and Strains

In this appendix we give the expressions for the stresses and strains in the rock due to P-wave propagation.

We consider a plane P-wave propagating along the $\hat{1}$ direction at an angle δ to the pore's main axis in the rectangular coordinate system $(\hat{1}, \hat{2}, \hat{3})$. The stresses and the strains in this coordinate system are:

$$\sigma_{11} = M = M_0 e^{i\omega(t - \frac{z \cos \delta}{V_p})}, \quad \epsilon_{11} = \frac{M}{\tilde{m}},$$

$$\sigma_{22} = \sigma_{33} = \lambda \epsilon_{11} = \lambda \frac{M}{\tilde{m}},$$

$$\sigma_{12} = \sigma_{13} = \sigma_{23} = 0,$$

$$\epsilon_{22} = \epsilon_{33} = \epsilon_{12} = \epsilon_{13} = \epsilon_{23} = 0,$$

where $\tilde{m} = \lambda + 2\mu$, λ and μ are Lamé's constants.

The normal and shear stresses σ_{xx} , σ_{yy} , σ_{zz} , σ_{xz} , σ_{xy} and σ_{zy} in the (x, y, z) coordinate system with the z -axis parallel to the pore's main axis are (White, 1983):

$$\sigma_{xx} = \left(\sin^2 \delta + \frac{\nu}{1 - \nu} \cos^2 \delta \right) M_0 e^{i\omega(t - \frac{z \cos \delta}{V_p})},$$

$$\sigma_{yy} = \frac{\nu}{1 - \nu} M_0 e^{i\omega(t - \frac{z \cos \delta}{V_p})},$$

$$\sigma_{zz} = \left(\cos^2 \delta + \frac{\nu}{1 - \nu} \sin^2 \delta \right) M_0 e^{i\omega(t - \frac{z \cos \delta}{V_p})},$$

$$\begin{aligned} \sigma_{xz} &= \sigma_{11} \sin \delta \cos \delta - \sigma_{22} \sin \delta \cos \delta \\ &= \cos \delta \sin \delta \left(1 - \frac{\nu}{1 - \nu} \right) M_0 e^{i\omega(t - \frac{z \cos \delta}{V_p})}, \end{aligned}$$

$$\sigma_{xy} = \sigma_{zy} = 0,$$

where ν is Poisson's ratio.

The normal and shear strains ϵ_{xx} , ϵ_{yy} , ϵ_{zz} , ϵ_{xz} , ϵ_{xy} and ϵ_{zy} are:

$$\epsilon_{xx} = \epsilon_{11} \sin^2 \delta,$$

$$\epsilon_{yy} = 0,$$

$$\epsilon_{zz} = \epsilon_{11} \cos^2 \delta,$$

$$\epsilon_{xz} = \epsilon_{11} \sin \delta \cos \delta,$$

$$\epsilon_{xy} = \epsilon_{zy} = 0.$$

Appendix C - Permeability Calculations

We vary the permeability while maintaining a constant porosity by considering N small pores of radii a_{0i} instead of one pore of a larger radius a_f .

Equating pore space volumes we have:

$$\pi a_f^2 = \pi \sum_{i=1}^{i=N} a_{0i}^2.$$

The porosity is

$$\phi = \frac{\pi \sum_{i=1}^{i=N} a_{0i}^2}{A}.$$

The specific surface area s is

$$s = \frac{2\pi \sum_{i=1}^{i=N} a_{0i}}{A}.$$

If all pores are aligned along the z -direction, then the permeability in the z -direction is:

$$k_z = \frac{\pi}{8A} \frac{(\sum_{i=1}^{i=N} a_{0i}^2)^3}{(\sum_{i=1}^{i=N} a_{0i})^2}.$$

If all pores have the same radii, $a_{01} = a_{02} = \dots = a_{0N}$, then

$$k_z = \frac{\pi}{8A} N a_{0i}^4.$$

CHAPTER 2

Relating P-Wave Attenuation to Permeability Anisotropy

ABSTRACT

In this paper we pursue a theoretical approach relating P-wave attenuation to permeability anisotropy. We examined a theoretical model of a three-dimensional cylindrical pore filled with viscous fluid, embedded in an infinite isotropic elastic medium. Attenuation estimates were based on the squirt flow mechanism. Permeability was calculated from the Kozeny-Carman formula. Permeability and attenuation were related to each other by independently calculating both of them as functions of the size of the pores and their orientations.

We investigated the effects of frequency, the length of a fluid drop, and the magnitudes of permeabilities along two perpendicular directions on the permeability-attenuation relation. We found that the attenuation of a low frequency P-wave is minimum when the wave propagates perpendicular to the direction of maximum permeability.

The permeability-attenuation relation for a rock with isotropic permeability is characterized by a peak which shifts towards lower permeabilities as frequency decreases. Therefore, the attenuation of a low-frequency wave decreases with increasing permeability. Our theoretical predictions are supported by experimental data.

INTRODUCTION

This paper presents a continuation of a theory developed by Akbar et al. (1993) in order to relate P-wave attenuation to permeability anisotropy. Akbar et al. (1993) modeled rock as an accumulation of identical typical cells with parallel pores inside. It was assumed that pores can be modeled as straight circular pipes partly filled with viscous fluid. The porosity of the rock was calculated as the ratio of the cross-sectional area of the pores to the cross-sectional area of the cell (Figure 2.1). Fluid flow inside pores is induced by the radial displacements of the walls due to P-wave excitation (the local flow mechanism). Permeability in a given direction was calculated by the Kozeny-Carman formula (e.g., Berryman and Blair, 1987). The specific dissipation

function Q^{-1} was found as the ratio of viscous energy dissipation during one period to the maximum stored energy in the representative cell (Mavko and Nur, 1979). Permeability and attenuation were related to each other by independently calculating both of them as functions of the size of the pores and their orientations (Akbar et al., 1993).

In the case of isotropic permeability, we study the effect of changing the pore's radius on attenuation. Accordingly, a rock with isotropic permeability can be represented by one typical pore oriented perpendicular to the direction of wave propagation (for this orientation, the deformation of the pore's walls is maximum under wave excitation). In this case, an attenuation-permeability relation has a maximum which shifts towards lower permeabilities as frequency decreases. This theoretical result is supported by the experimental data obtained on five samples of Fontainebleau sandstone (99% quartz) with different porosities and permeabilities at ultrasonic ($\omega \approx .5$ MHz) and sonic ($\omega \approx 1.14\text{kHz}-6.5\text{kHz}$) frequencies (Lucet, 1990; and Akbar et al., 1993). For a low-frequency P-wave, maximum attenuation occurs at very low permeabilities. Therefore, for cases of practical interest, the attenuation of a low-frequency wave decreases systematically with increasing permeability. This result has many practical applications in oil explorations. Another vital application is to locate, using attenuation measurements, regions with low permeabilities.

We extend this theoretical approach to the case where a rock is characterized by two permeabilities k_{max} and k_{min} ($k_{max} > k_{min}$) in two perpendicular directions. The attenuation is computed as a function of the incident angle measured from the direction of the minimum permeability. We explore the influence of such factors as: frequency, the length of the fluid drop, and the magnitudes of permeability along the two perpendicular directions on the attenuation versus incident angle relation. We show that frequency plays an important role in relating permeability anisotropy to attenuation anisotropy. For rocks with small fractures and porosities, the attenuation of seismic-sonic frequency P-waves (1 - 10 kHz) is minimum when the waves propagate perpendicular to the direction of maximum permeability. Since all field measurements

are conducted in a low-frequency range, this result provides us with a direct tool for seismic data interpretation, including VSP and cross-borehole measurements.

The situation changes as frequency increases: in the ultrasonic frequency range, the attenuation of a P-wave propagating perpendicular to the direction of maximum permeability is maximum when the magnitudes of permeabilities along each direction are small; and is minimum when the permeabilities are large. This result does not necessarily hold for high porosity rocks having long pores saturated with high viscosity fluid. Determining the direction of maximum attenuation for a wave with ultrasonic frequency requires a rigorous consideration depending on specific values of crucial parameters.

THEORETICAL MODEL

In the previous chapter (Akbar et al., 1993), we related attenuation to permeability for the case when all pores were aligned in the same direction (permeability perpendicular to this direction was assumed to be zero). Here we extend our model to represent a rock with given nonzero permeabilities in two perpendicular directions.

Attenuation in a rock with permeabilities along two perpendicular directions can be modeled using two representative sets of perpendicular pores (two-dimensional case). Each set contains circular pores of the same radius. As will be shown below, the number and the radius of pores in each direction depend on the permeability along that given direction. Pores' radii are related to permeability by the Kozeny-Carman equation. The representative pore's length H and the length of the microscopic fluid drop L are related through the saturation S by $L = HS$. In our calculations, we assume that L , S , and H are the same along both perpendicular directions. The representative pore's length H is a "free parameter" and has to be determined by matching theoretical to experimental data.

It is necessary to emphasize that we examine a two-dimensional model of a rock with pores oriented only in the x and z directions. We introduce the following two-dimensional porosities (Biot, 1956): one (ϕ_x) in the plane perpendicular to the x

direction and another (ϕ_z) in the perpendicular to the z direction (Figure 2.1a). The porosity ϕ_x (or ϕ_z) is defined as the ratio of the cross-sectional area of the pore aligned in the x (or the z) direction to the total cross-sectional area perpendicular to the x (or the z) direction. The total porosity ϕ is defined as the ratio of pores' volume to the total volume of the rock. We assume that $\phi_x = \phi_z$ and that the bulk porosity of the rock is the sum of these two porosities:

$$\phi = \phi_x + \phi_z; \quad \phi_x = \phi_z = \frac{\phi}{2}. \quad (1)$$

Considering a sample of the rock with unit cross-sectional areas perpendicular to the x and z directions, we have the following formulas for porosities ϕ_x and ϕ_z :

$$\phi_x = \pi r_x^2 N_x; \quad \phi_z = \pi r_z^2 N_z, \quad (2)$$

where r_x and r_z are pore radii in the x and z directions, and N_x and N_z are the number of pores through unit cross-sectional areas in these directions respectively (Figure 2.1a).

As we mentioned earlier, permeabilities may be different along the x and z directions. We compute these permeabilities (k_x and k_z) by using the Kozeny-Carman equation for circular pores (Akbar et al., 1993):

$$k_x = \frac{\pi}{8} r_x^4 N_x; \quad k_z = \frac{\pi}{8} r_z^4 N_z. \quad (3)$$

Equations (1)-(3) lead to the following system of four equations for four unknown parameters r_x , r_z , N_x and N_z :

$$r_x^2 N_x = \frac{\phi}{2\pi}, \quad r_z^2 N_z = \frac{\phi}{2\pi}, \quad r_x^4 N_x = \frac{8k_x}{\pi}, \quad r_z^4 N_z = \frac{8k_z}{\pi}.$$

Solving this system we find:

$$r_x = \sqrt{\frac{16k_x}{\phi}}, \quad r_z = \sqrt{\frac{16k_z}{\phi}}, \quad N_x = \frac{\phi^2}{32\pi k_x}, \quad N_z = \frac{\phi^2}{32\pi k_z}. \quad (4)$$

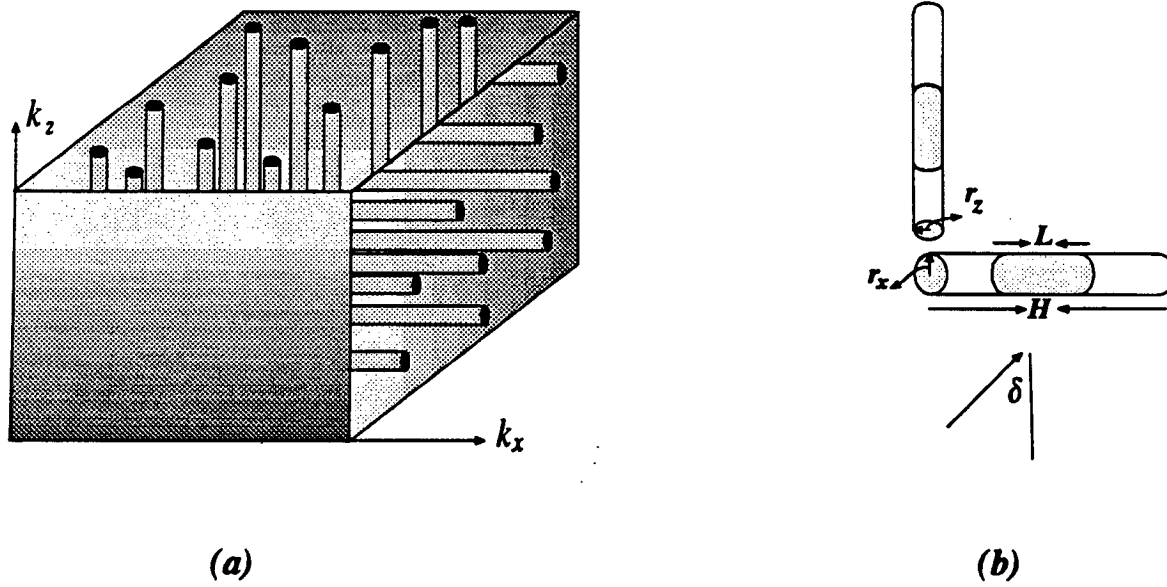


Fig. 2.1. (a) A rock sample with permeabilities k_x and k_z ($k_x > k_z$) along two perpendicular directions. (b) Two perpendicular pores with radii r_x and r_z represent the permeabilities along two perpendicular directions.

NUMERICAL ANALYSIS

In this section we apply our theoretical model to predicting quantitative relationships between permeability and attenuation for isotropic and anisotropic cases. We define an incident angle δ of a P-wave as the angle between the direction of wave propagation and the direction of minimum permeability (Figure 2.1b). In the numerical analysis below, we will refer to the ratio of attenuations \tilde{R} by:

$$\tilde{R} = \frac{Q_{\delta=0^\circ}^{-1}}{Q_{\delta=90^\circ}^{-1}}.$$

Next, we perform the numerical experiments on a limestone sample with porosity $\phi = 4.7\%$, P-wave velocity $V_p = 5.59$ km/s, S-wave velocity $V_s = 2.99$ km/s and density $\rho = 2.663$ gm/cm³. With these parameters fixed, we study the effects of frequency, fluid viscosity, fluid microdistribution (the length of a fluid drop), permeability, and permeability anisotropy on P-wave attenuation.

Rock With Isotropic Permeability

A rock with isotropic permeability k can be represented by pores having all possible orientations. Each pore contributes to the overall attenuation depending on the angle between its main axis and the direction of the propagation. We approximate the attenuation by representing such a rock with one typical cell having a pore that is perpendicular to the direction of the plane wave. This approximation gives reasonable qualitative estimates since attenuation is always maximum when the propagation is perpendicular to the main axis of the pore (Akbar et al., 1993).

Effects of the drop length on attenuation (Figures 2.2,2.3)

Figure 2.2 shows attenuation, ($\log Q^{-1}$) versus length of the fluid drop L . In this example, permeability k of the rock is 50 mD and the angular frequency of the wave ω is .5 MHz. Two types of saturating fluid are considered: crude oil of viscosity 7.8 cp, and pure water of viscosity 1 cp. In both cases attenuation reaches its maximum and then decreases with increasing L . The maximum attenuation for crude oil is sharper than for water and occurs at smaller lengths ($L \approx 8$ mm). Figure 2.3 shows $\log Q^{-1}$ versus L for crude oil at two frequencies .5 MHz and 50 kHz. The peak corresponding to the higher frequency is sharper and takes place at a smaller length. The dependence of attenuation on the length of the fluid drop is due to the fact that the displacement of the pore's wall in our model is perpendicular to the direction of the fluid motion. The peaks in attenuation shown in Figures 2.2 and 2.3 can be explained as follows: when the length of the fluid drop is small, the velocity gradient of the fluid is small and results in small attenuation. The mechanism involved here is best described by the local flow mechanism. As fluid length increases, the velocity gradient increases sharply and attenuation reaches its peak. Further increase does not allow the fluid to relax (freezes the fluid), resulting in a smooth decrease in attenuation.

Effects of frequency (Figure 2.4)

Figure 2.4 shows $\log Q^{-1}$ versus $\log k$ for three frequencies $\omega = 5$ kHz, 50 kHz, and .8 MHz, for a fluid droplet of 10 mm in length. In this case, the effect of frequency on the attenuation-permeability curves is to shift the peak towards lower permeabilities as frequency decreases. At low frequencies, the slope of the permeability-attenuation curves is negative for all permeabilities ($\log Q^{-1}$ decreases with increasing permeability). On the other hand, at high frequency, the slope of the permeability-attenuation curve is negative for large permeabilities and is positive for small permeabilities ($\log Q^{-1}$ increases with increasing permeability). This result supports the experimental data (Figure 2.12).

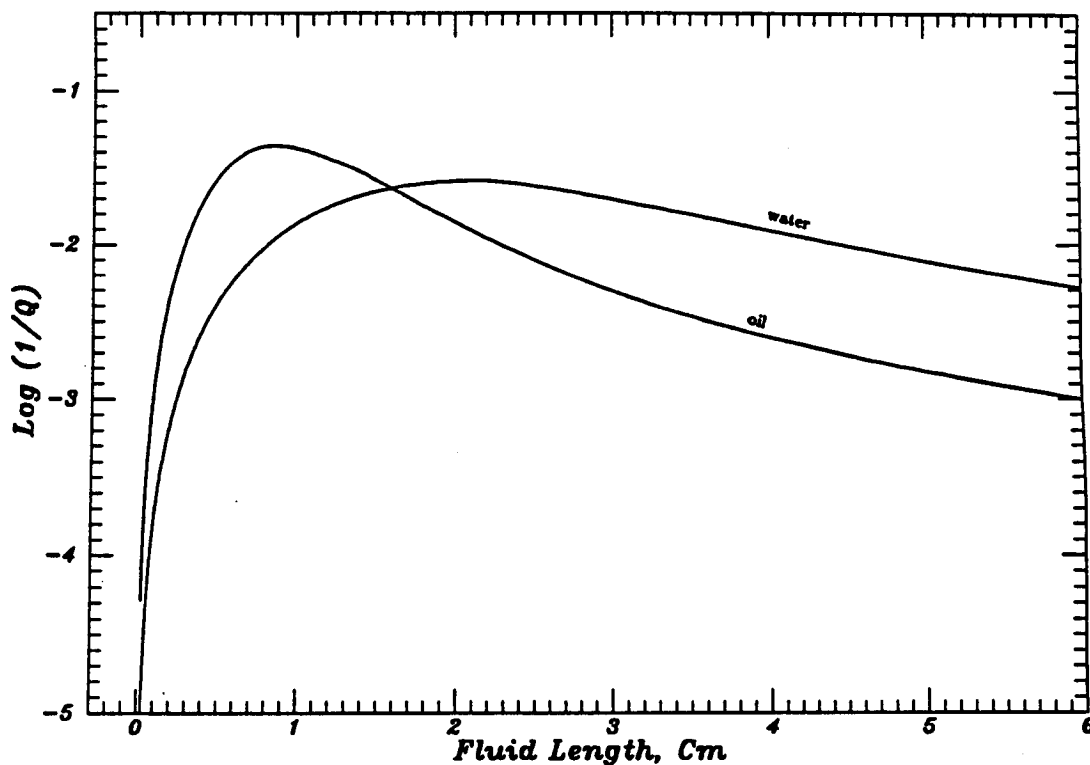


Fig. 2.2. $\log Q_p^{-1}$ versus the length of the fluid drop L for a wave with frequency $\omega = .5$ MHz.

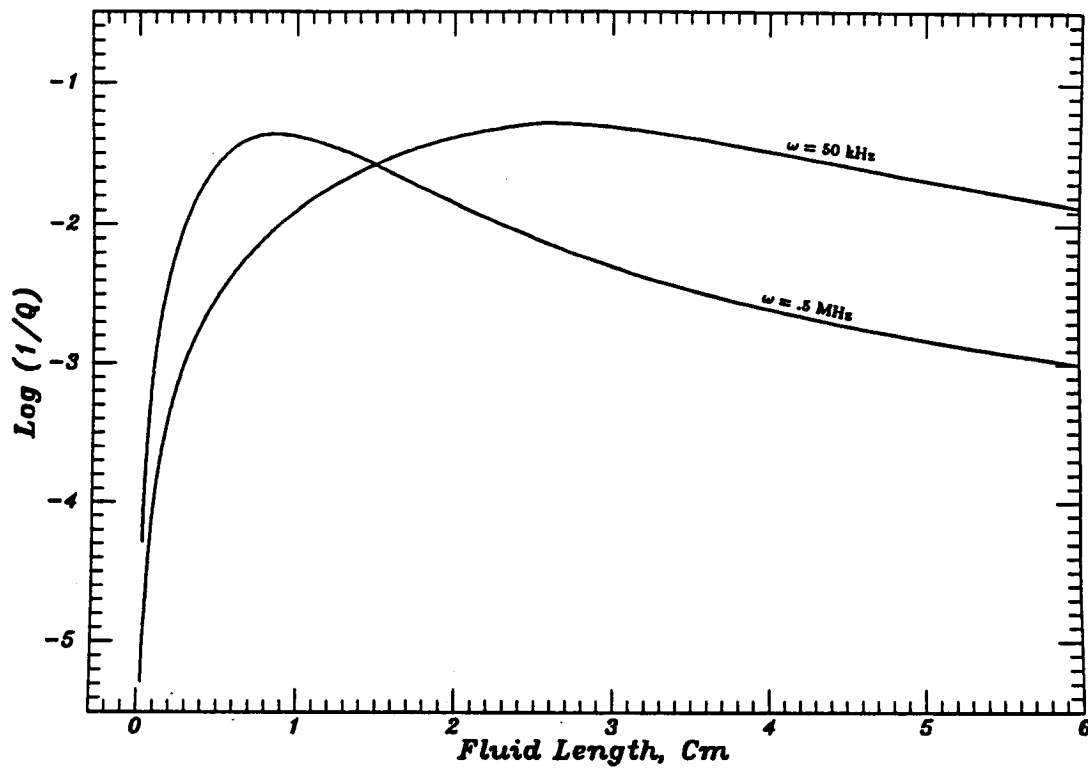


Fig. 2.3. $\log Q^{-1}$ versus L using the properties of crude oil as a saturating fluid for two frequencies $\omega = .5 \text{ MHz}$ and $\omega = 50 \text{ kHz}$. The peak corresponding to the higher frequency is sharper and takes place at smaller length.

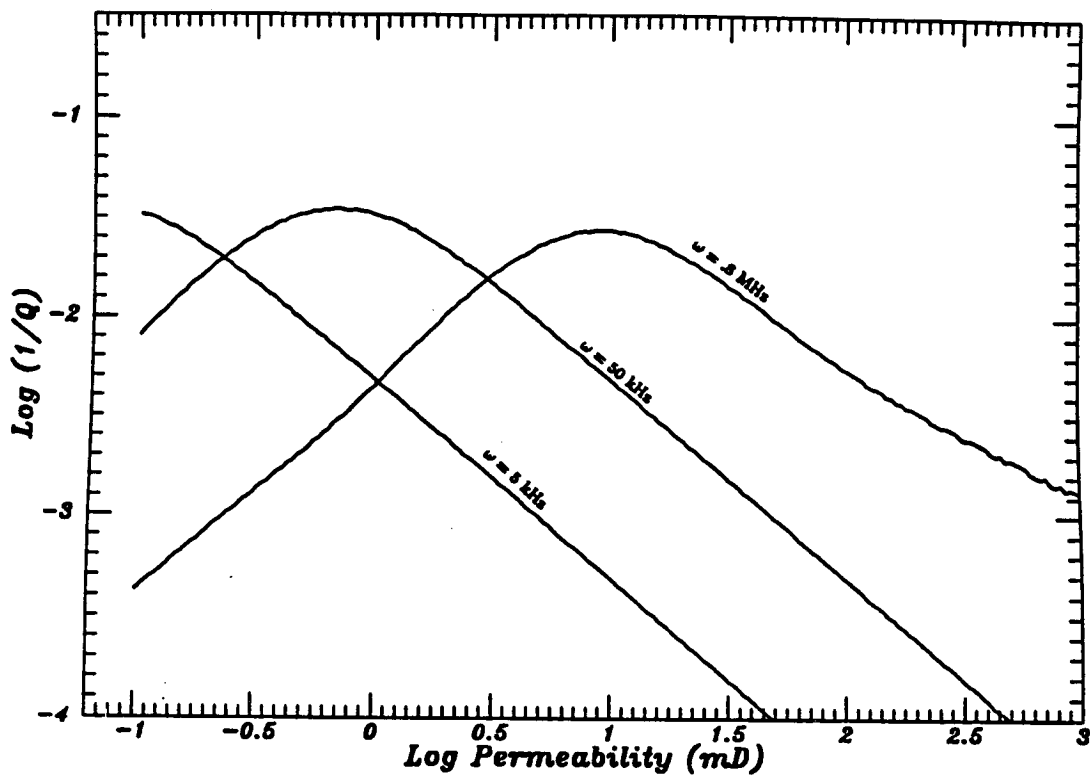


Fig. 2.4. $\log Q^{-1}$ versus $\log k$ for three different frequencies $\omega = 5 \text{ kHz}$, 50 kHz , and $.8 \text{ MHz}$. Porosity is 4.7 % and the length of the fluid drop is 10 mm.

Rock With Anisotropic Permeability

In this section we estimate the direction of maximum attenuation for a rock with known permeabilities k_{max} and k_{min} along the x and the z directions, respectively. As a plane P-wave with a known frequency propagates through such a rock, the resultant attenuation will depend on the contribution from pores along each direction. We previously found that attenuation (for a cell containing a pore oriented along a given direction) is maximum when the wave propagates perpendicular to the pore orientation (Akbar et al., 1993). This suggests that if pores along one of the directions dominate attenuation for a given frequency, then the overall attenuation reaches its maximum when the wave propagates perpendicular to the direction of the dominating permeability. The permeability which dominates attenuation for a given frequency can be found from Figure 2.4 which represent the permeability-attenuation relations for the isotropic case.

Effects of frequency (Figures 2.5-2.9)

Figure 2.4 shows that, for the whole range of permeabilities, attenuation decreases with increasing permeability (negative slope) for a wave with a small frequency. If the permeability along the x direction is k_{max} and the permeability along the z direction is k_{min} , then the smaller permeability k_{min} will dominate the attenuation. Accordingly, the overall attenuation reaches its maximum when the propagation is perpendicular to the direction of k_{min} .

For large frequencies, the positions of k_{min} and k_{max} on the attenuation-permeability curves will be one of three cases depending on the magnitudes of k_{min} and k_{max} . The first case occurs when k_{min} and k_{max} are large and lie on the negative slope. In this case, the minimum permeability k_{min} dominates attenuation and the wave will have a maximum attenuation when it propagates perpendicular to the direction of k_{min} .

The second case occurs when both k_{min} and k_{max} are small and lie on the positive slope. As a result, k_{max} dominates attenuation and a maximum attenuation occurs when the propagation is perpendicular to the direction of k_{max} .

The final case takes place when k_{min} and k_{max} lie on the positive and on the negative slopes respectively. The direction of the maximum attenuation will here depend on the magnitudes of k_{min} and k_{max} . In the following analysis we exclude this case and consider only those in which both permeabilities are either large or small.

Figure 2.5 shows $\log Q^{-1}$ versus incident angle δ (measured from the direction of k_{min}) for a rock with large permeabilities $k_{min} = 100$ mD and $k_{max} = 1000$ mD along two perpendicular directions for four frequencies, $\omega = 500$ Hz, 5 kHz, 50 kHz, and .8 MHz. For all frequencies, the attenuation is maximum when the wave propagates perpendicular to the direction of the minimum permeability k_{min} . This results from the fact that the attenuation is dominated by the lower permeability $k_{min} = 100$ mD for all of the four frequencies (Figure 2.4).

Figure 2.6 represents Q^{-1} versus incident angle δ for a rock with small permeabilities $k_{min} = 1$ mD and $k_{max} = 10$ mD and for four frequencies, $\omega = 500$ Hz, 5 kHz, 50 kHz, and .8 MHz. For small frequencies, $\omega = 500$ Hz and 5 kHz, the attenuation is maximum when the wave propagates perpendicular to the direction of minimum permeability k_{min} . This is due to the fact that attenuation is dominated by $k_{min} = 1$ mD.

For larger frequencies, $\omega = 50$ kHz and .8 MHz, the attenuation is maximum when the wave propagates perpendicular to the direction of maximum permeability k_{max} . This is due to the fact that in this frequency range the attenuation is dominated by k_{max} .

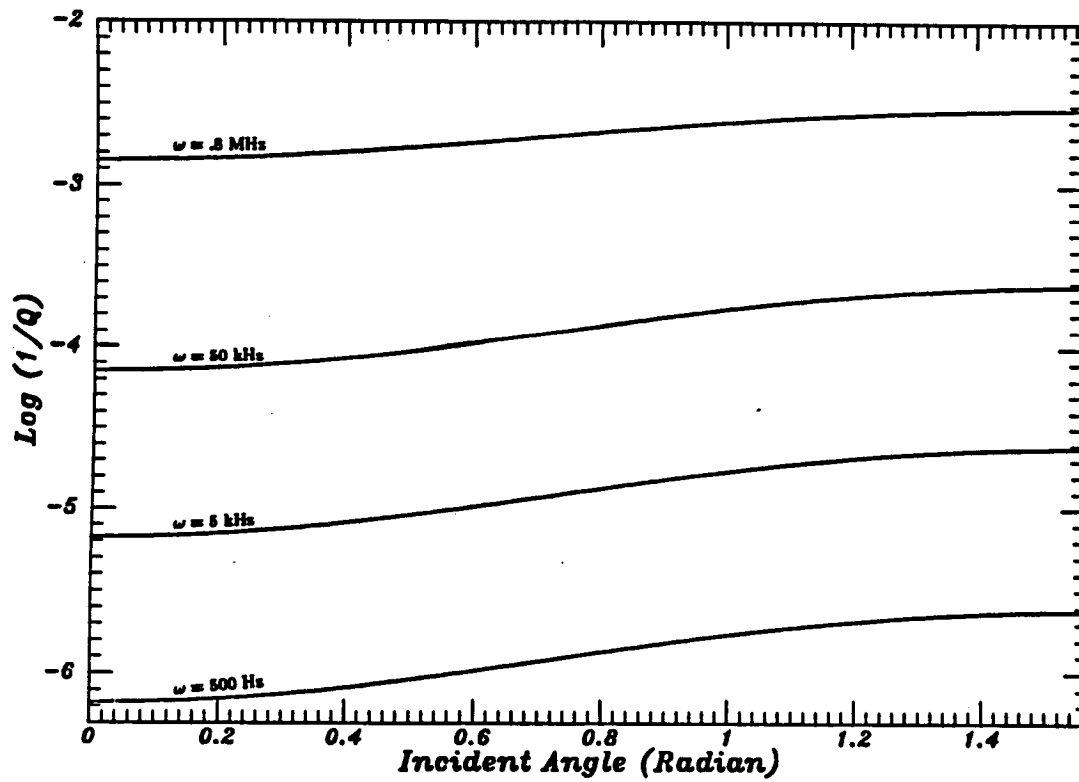


Fig. 2.5. $\log Q^{-1}$ versus incident angle δ for a rock with permeabilities 100 mD and 1000 mD along two perpendicular directions for four frequencies $\omega = 500 \text{ Hz}$, 5 kHz, 50 kHz, and .8 MHz.

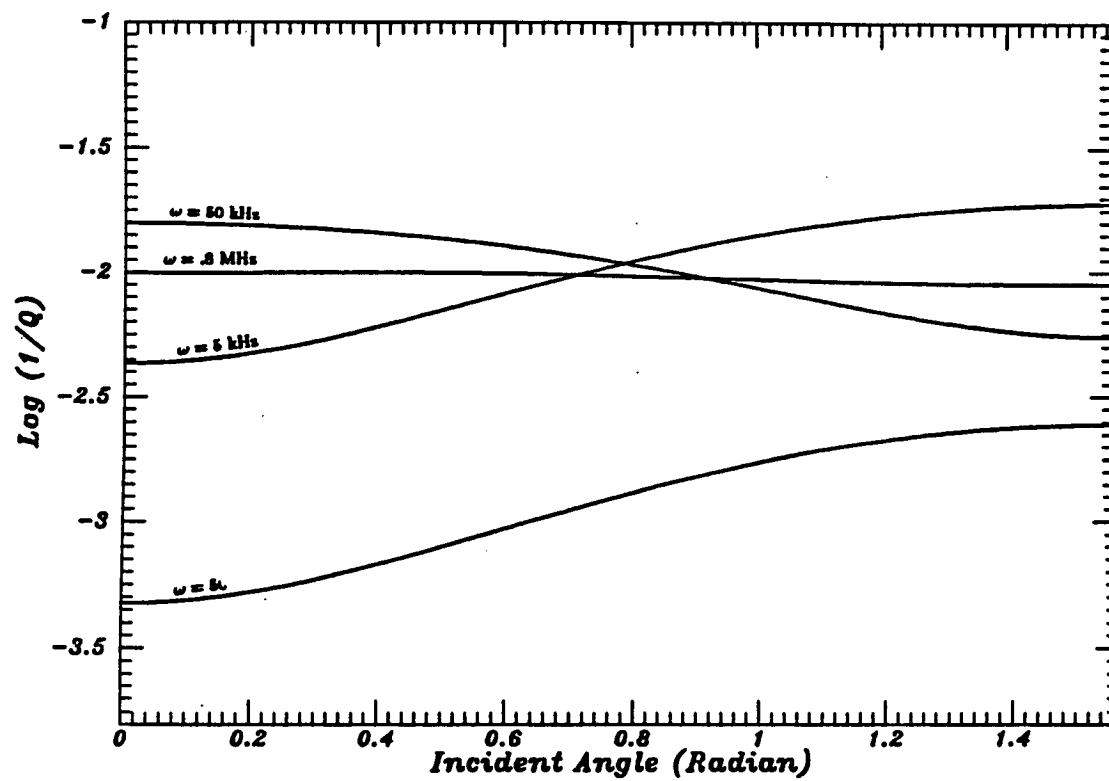


Fig. 2.6. $\log Q^{-1}$ versus incident angle δ for a rock with permeabilities .1 mD and 10 mD along two perpendicular directions for four frequencies $\omega = 500 \text{ Hz}$, 5 kHz, 50 kHz, and .8 MHz.

To clarify the role of the frequency, we repeat, the calculations of Figures 2.4, 2.5, and 2.6 in the following three plots (Figures 2.7, 2.8, and 2.9), by introducing the frequency in the third dimension.

Figure 2.7 is a three-dimensional extension to Figure 2.4 where we plot $\log Q^{-1}$ versus $\log k$ and versus $\log \omega$ for a rock with isotropic permeability. The slopes of the curves in the $\log Q^{-1} - \log k$ plane are always negative for small fixed frequencies. For larger frequencies, the slopes of $\log Q^{-1} - \log k$ curves are negative for large permeabilities and are positive for small permeabilities.

In Figure 2.8 we extended Figure 2.5 to a three-dimensional plot of $\log Q^{-1}$, incident angle δ , and frequency $\log \omega$ for a rock with $k_{min} = 100$ mD and $k_{max} = 1000$ mD along two perpendicular directions. For the whole frequency range, increasing the angle of incidence δ results in increasing Q^{-1} in the $Q^{-1} - \delta$ plane. This means that a maximum attenuation takes place when the wave front propagates perpendicular to the direction of the minimum permeability. This is due to the fact that for the large permeabilities chosen here (100 mD and 1000 mD), the attenuation is dominated by the lower permeability k_{min} (negative slopes in Figure 2.7). The single peak in the $\log Q^{-1} - \log \omega$ plane is due to $k_{min} = 100$ mD. We expect another peak that corresponds to $k_{max} = 1000$ mD at a higher frequency range.

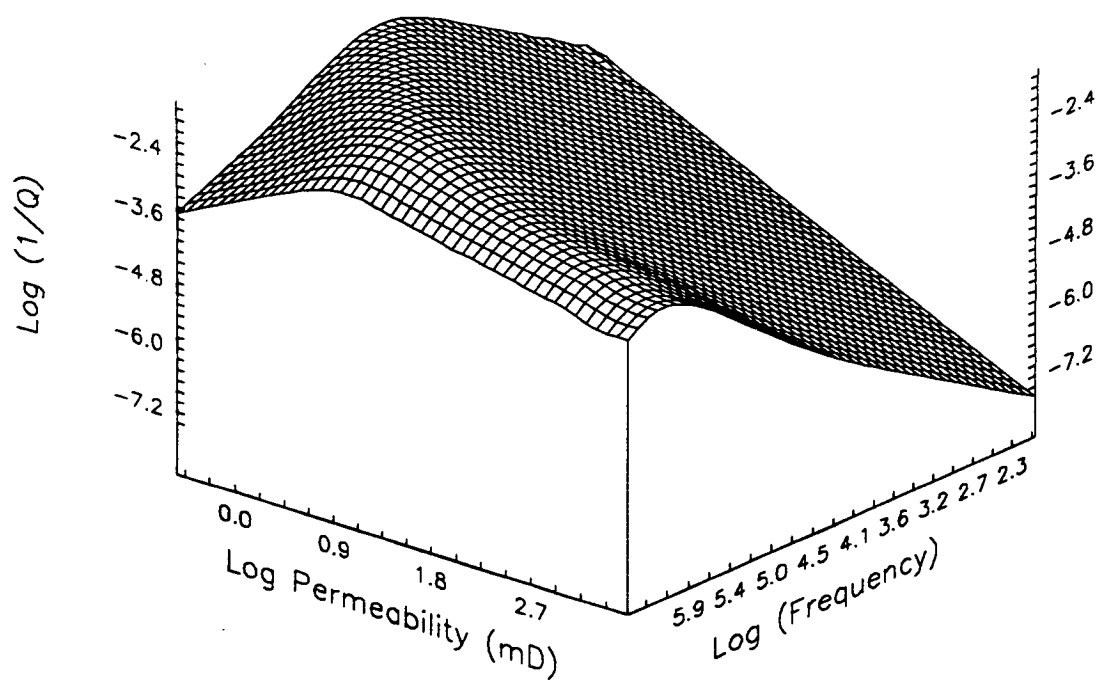


Fig. 2.7. A three-dimensional plot of $\log Q^{-1}$ versus permeability and versus frequency for a rock with isotropic permeability k .

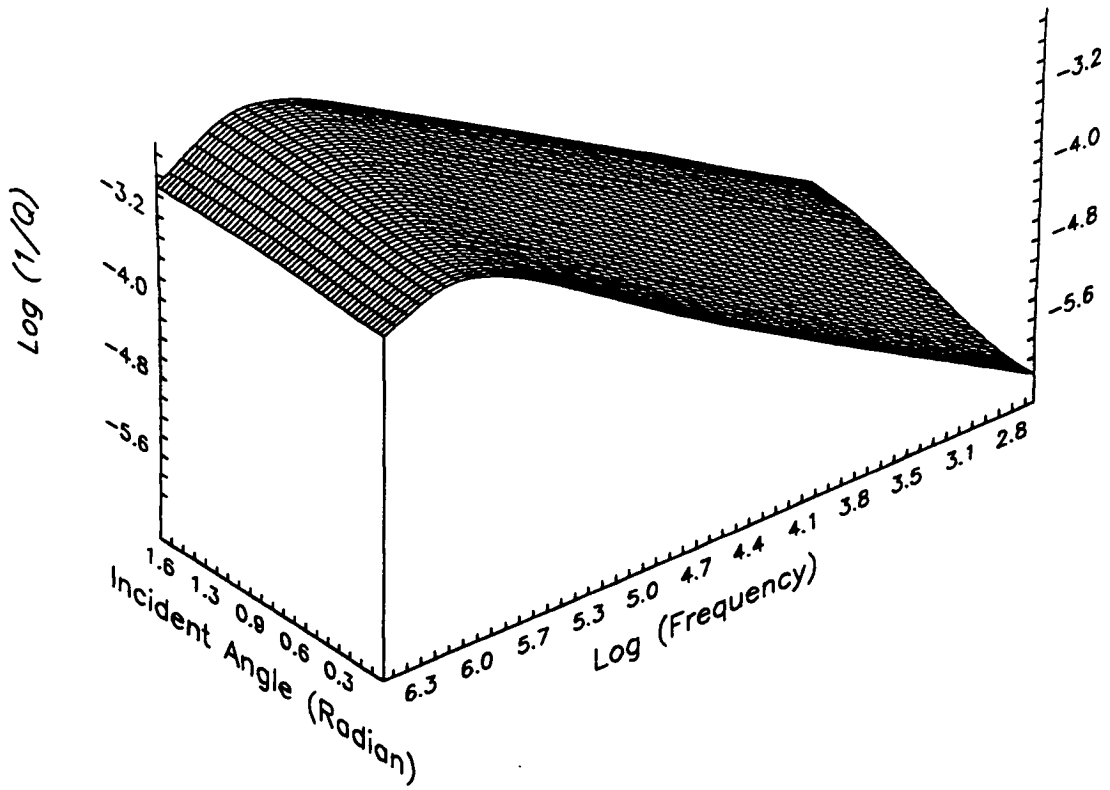


Fig. 2.8. A three-dimensional plot of $\log Q^{-1}$, incident angle, and frequency for a rock with permeabilities 100 mD and 1000 mD along two perpendicular directions.

Figure 2.9 is an extension of Figure 2.6 to a three-dimensional plot of $\log Q^{-1}$, δ , and $\log \omega$ for a rock with small permeabilities $k_{min} = .1$ mD and $k_{max} = 10$ mD along two perpendicular directions. We notice the existence of two distinct peaks in the $\log Q^{-1} - \log \omega$ plane. The first peak that occurs at low frequency ($\omega \approx 16$ kHz) is due to $k_{min} = .1$ mD. Therefore, the dominating permeability in this frequency range is k_{min} . As we move towards higher angles of incidences in the $\log Q^{-1} - \delta$ plane, $\log Q^{-1}$ increases with the incident angle δ . This means that maximum attenuation takes place when the wave propagates perpendicular to the direction of k_{min} .

The second peak is located at a higher frequency ($\omega \approx .56$ MHz) and is associated with $k_{max} = 10$ mD. The dominating permeability in this frequency range is k_{max} . The attenuation decreases with the increasing angle of incidences in the $\log Q^{-1} - \delta$ plane. This results in maximum attenuation when the propagation is perpendicular to the direction of k_{max} .

We notice that $Q_{\delta=0^\circ}^{-1}$ approaches $Q_{\delta=90^\circ}^{-1}$ for very large frequencies. This is due to the fact that attenuation depends weakly on incident angles for very high frequencies (Akbar et al., 1993).

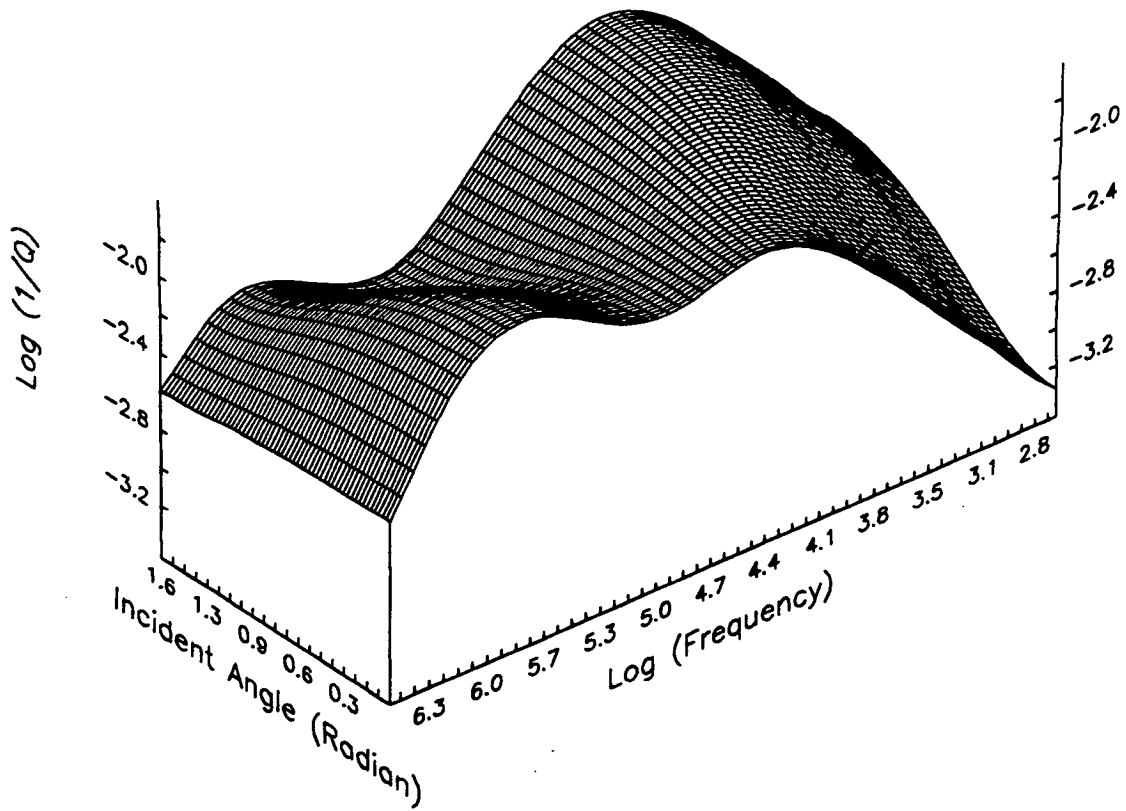


Fig. 2.9. A three-dimensional plot of $\log Q^{-1}$, incident angle, and frequency for a rock with permeabilities $k = .1$ mD and 10 mD along two perpendicular directions.

Effects of length of the fluid drop (Figures 2.10, 2.11)

In this section we use three-dimensional plots to study the effects of the length of the fluid drop on our previous results (Figures 2.5-2.9).

Consider a rock with k_{max} and k_{min} along two perpendicular directions. We assume that $k_{max} = Ck_{min}$, where $C > 1$ is the ratio of the permeabilities along the two perpendicular directions. In Figures 2.10 and 2.11 we use $C = 5$ and vary k_{max} along the x axis and the frequency ω along the y axis. The attenuation ratio $\tilde{R} = \frac{Q_{\delta=0^\circ}^{-1}}{Q_{\delta=90^\circ}^{-1}}$ is plotted along the z axis. \tilde{R} is greater than one if the attenuation is higher when the wave propagates perpendicular to the direction of k_{max} and is less than one if attenuation is higher when the propagation is perpendicular to the direction of k_{min} .

Figure 2.10 shows \tilde{R} versus $\log k_{max}$ and $\log \omega$ for a water-saturated rock with $L = 1$ mm. The plot shows that \tilde{R} is greater than one only for large frequencies and small permeabilities.

In Figure 2.11 we study the effects of increasing the length of the fluid drop on \tilde{R} , where we use $L = 4$ mm. As demonstrated by the plot, the range in the $\log k_{max} - \log \omega$ plane for which \tilde{R} is greater than one becomes larger by increasing the length of the fluid drop.

Figures 2.10 and 2.11 show that the direction of maximum permeability depends strongly on the length of the fluid drop for a high frequency wave. However, the dependence on the length of the fluid drop becomes less important for small frequencies where the maximum attenuation takes place when the propagation is perpendicular to the direction of minimum permeability.

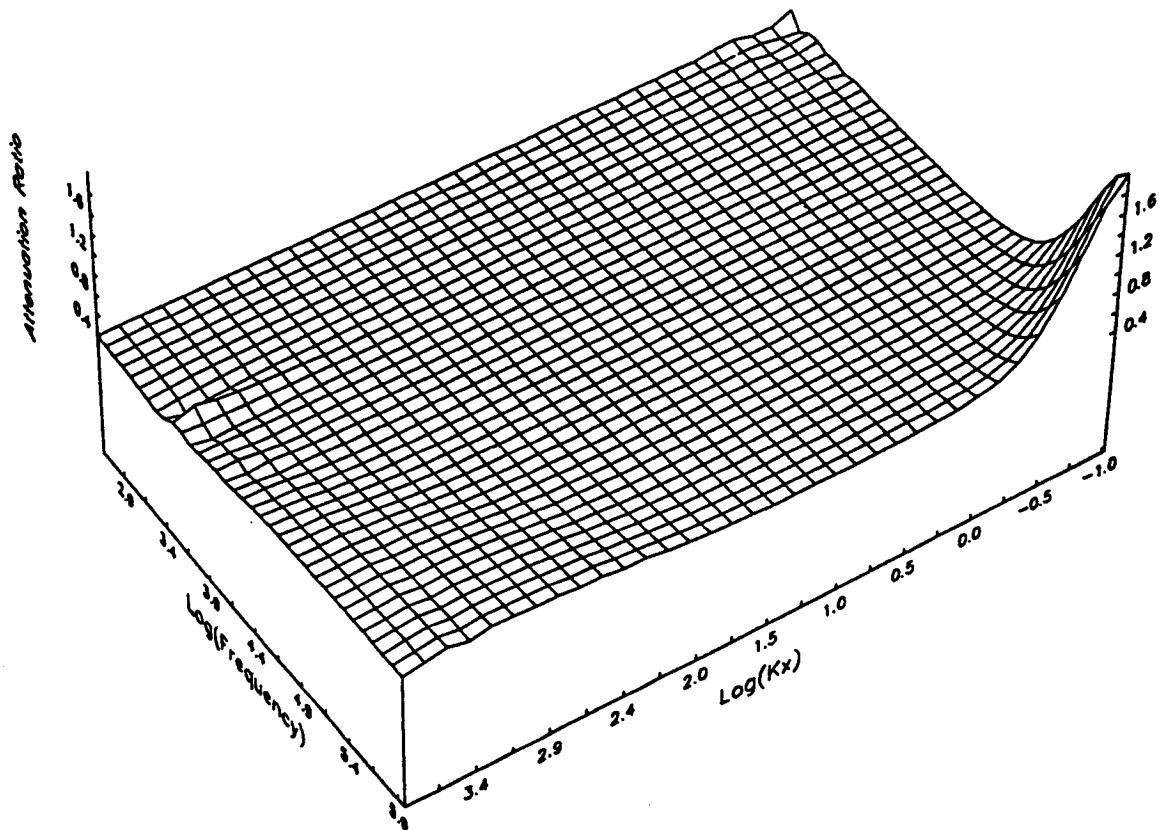


Fig. 2.10. The attenuation ratio versus $\log k_{max}$ and $\log \omega$ for a water-saturated rock with permeabilities $k_{max} = 5k_{min}$ along two perpendicular directions.

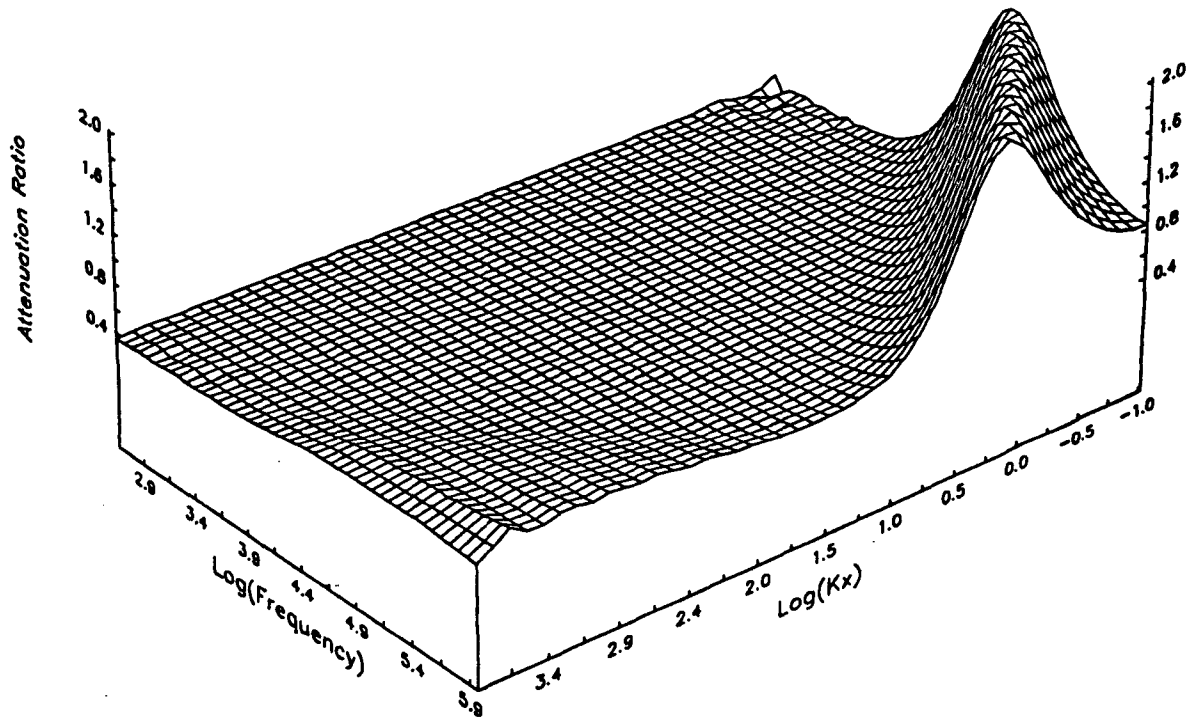


Fig. 2.11. The attenuation ratio versus k_{max} and ω for $\phi = 4.7\%$ and $L = 4$ mm.

COMPARISON WITH DATA

Effect of Frequency on Permeability-Attenuation Relation (Figure 2.12)

In this section, we model the experimental results from Lucet (1989) where attenuation was measured as a function of the applied external stress for five Fontainebleau sandstone samples (99% quartz) with known permeabilities and porosities. The attenuation of the extensional waves Q_e^{-1} was measured for sonic frequencies ($\omega \approx 1.14$ kHz - 6.5 kHz). For ultrasonic frequencies ($\omega \approx .5$ MHz), the attenuation of the compressional waves Q_p^{-1} was measured.

We estimated Q_p^{-1} for the sonic frequency range from the available data of Q_e^{-1} by using the following relation (Winkler, 1979):

$$(1 - \nu)(1 - 2\nu) Q_p^{-1} \approx (1 + \nu) Q_e^{-1} - 2\nu(2 - \nu) Q_s^{-1},$$

where ν is Poisson's ratio, and Q_s^{-1} is the attenuation of the shear waves.

The density of each rock ρ is also estimated from porosity:

$$\rho = \rho_m(1 - \phi) + \phi\rho_f,$$

where ρ_m is the density of the matrix (quartz), and ρ_f is the density of the fluid (water).

Tables 1.1 and 1.2 from chapter 1 summarize the measured and the estimated experimental data for ultrasonic and sonic frequencies respectively when the applied external stress is 5 MPa.

We model this data set by calculating the attenuation for each rock, characterized by its known porosity, permeability, and elastic moduli, for both ultrasonic ($\omega = .5$ MHz) and sonic ($\omega = 4$ kHz) frequencies. We use $\delta = 90^\circ$ as an incident angle, and the $L = 2$ cm as the length of the fluid drop (water). The representative pore's radius for each rock is found by using the following relation (Berryman and Blair, 1987):

$$r = \sqrt{\frac{8k}{\phi}},$$

where k and ϕ are found from the experimental data (Table 1.1, Chapter 1).

Tables 2.1 and 2.2 show our theoretical results for pore radii and attenuation $\log Q_p^{-1}$ for ultrasonic and sonic frequencies, respectively.

Figure 2.12 shows the measured and the calculated Q_p^{-1} (normalized by their maxima) for each rock versus permeability. Letters U and S denote the experimental data for ultrasonic and sonic frequencies, respectively. Points connected by lines and dashed lines represent the theoretical results for ultrasonic and sonic frequencies, respectively. The experimental and theoretical results show that attenuation decreases with increasing permeability for a wave with low frequency. For ultrasonic frequencies, the attenuation is small for low and high permeabilities and reaches a maximum at about $k = 1000$ mD.

Table 2.1. The calculated pore radii and attenuation $\log Q_p^{-1}$ for ultrasonic frequencies.

Sample #	ϕ %	k (mD)	Radius(μm)	$\text{Log}_{10} Q_p^{-1}$	$Q_p^{-1}(\text{Normalized})$
A6	6.7	6	0.846	-2.050	0.330
F60	13.6	670	6.278	-1.672	0.789
F5	14.8	720	6.238	-1.569	1.000
F64	15.5	1080	7.466	-1.649	0.833
A8	22	2800	10.09	-1.706	0.729

Table 2.2. The calculated pore radii and attenuation $\log Q_p^{-1}$ for sonic frequencies.

Sample #	ϕ %	k (mD)	Radius(μm)	$\text{Log}_{70} Q_p^{-1}$	$Q_p^{-1}(\text{Normalized})$
A6	6.7	6	0.846	-2.120	1.0000
F60	13.6	670	6.278	-2.921	0.0445
F5	14.8	720	6.238	-2.749	0.0661
F64	15.5	1080	7.466	-2.917	0.0449
A8	22	2800	10.09	-3.124	0.0279

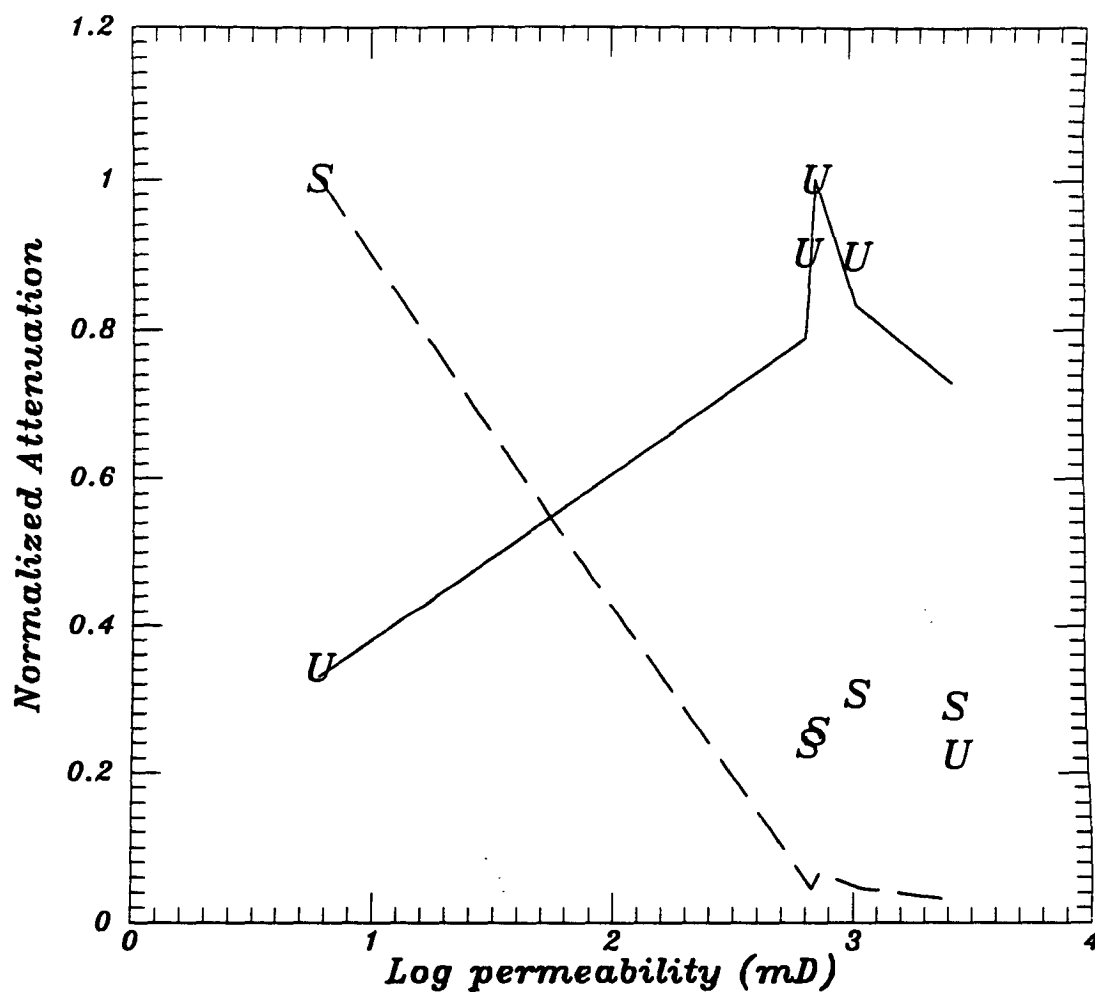


Fig. 2.12. The measured and the calculated Q_p^{-1} (normalized by their maxima) versus permeability for five samples of Fontainebleau sandstones. Letters *U* and *S* denote the experimental data for ultrasonic and sonic frequencies respectively. Points connected by lines and dashed lines represent the theoretical results for ultrasonic and sonic frequencies, respectively. Data are from Lucet (1989).

Permeabilities Along two Perpendicular Directions (Figure 2.13)

In this section, we model experimental results from Tarif (1986) for water-saturated Meule Vert sandstone sample. The compressional and shear velocities of the sample are: $V_p = 3.067$ km/s and $V_s = 1.625$ km/s, respectively. The porosity of the sample is 22.3%. The sample is homogeneous and contains mica sheets which show the orientation of the sedimentation. The average grain size is about 200 μm , and the permeabilities of the sample are 114 mD and 72 mD in the x and the z directions, respectively. Attenuations are measured in both directions (Q_x^{-1} and Q_z^{-1}) as functions of saturation. The frequency ranges from .25 MHz to .75 MHz with a central frequency of .5 MHz.

The experimental results show that for all saturations, the attenuation is minimum when the wave propagates perpendicular to the direction of the maximum permeability (i.e., \tilde{R} is less than one).

We model this experiment by calculating the attenuations from both directions for a high-frequency wave $\omega = .5$ MHz by considering a rock with the properties as given above. Our theoretical results best fit the data when the microscopic pore's length H is 5 mm. The length of the fluid drop L is found from the relation $H = L/S$, where S is saturation.

\tilde{R} is plotted in Figure 2.13 as a function of saturation. The experimental data and the theoretical results are represented by asterisks and the solid line, respectively.

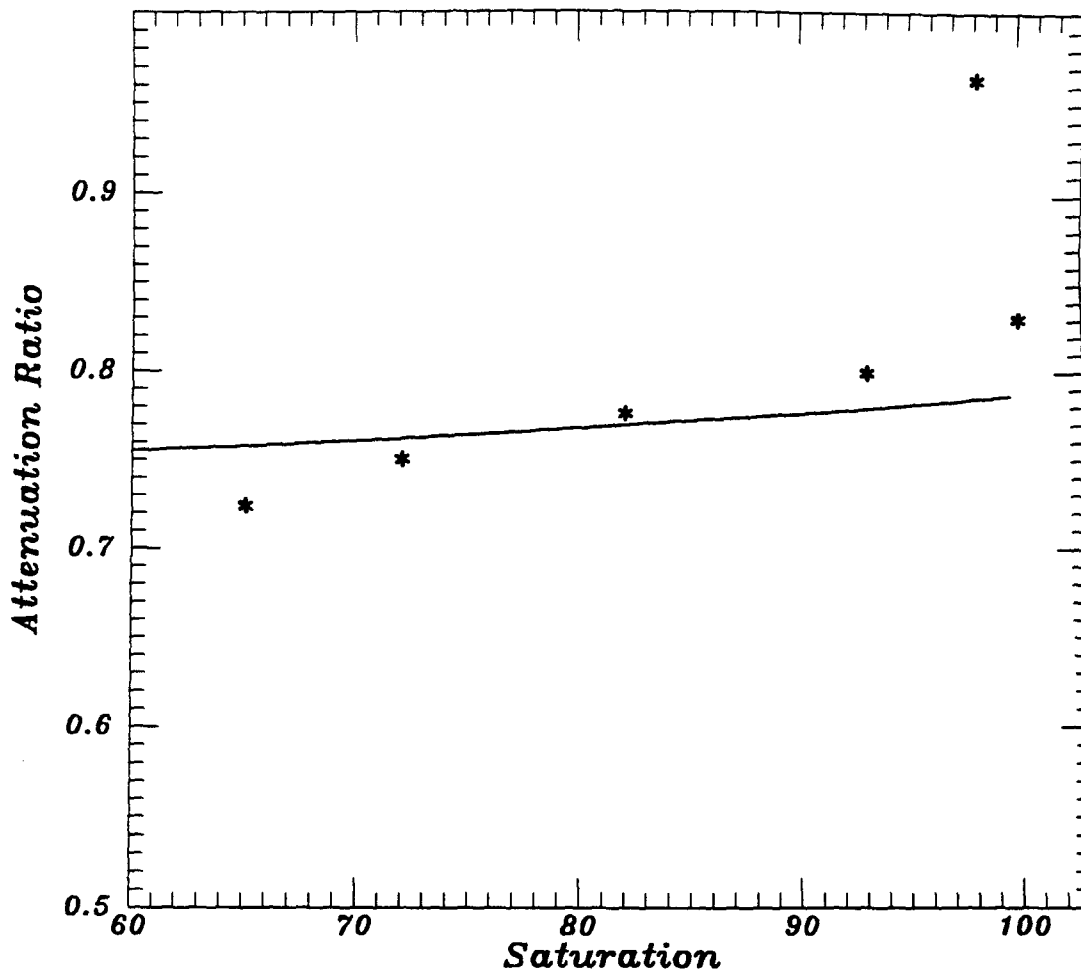


Fig. 2.13. The attenuation ratio \tilde{R} versus saturation for Meule Vert sandstone sample. The permeabilities of the samples were about 114 mD and 72 mD in the x and the z directions respectively. The data are from Tarif (1986).

CONCLUSIONS

We related permeability and attenuation of a P-wave to each other by independently calculating both of them as functions of pore size and orientation. A rock is modeled as an accumulation of identical typical cells containing circular pores that are partly filled with viscous fluid.

For a rock with isotropic permeability, we found that the variation of attenuation with permeability is characterized by a peak in attenuation which shifts towards a lower permeability as frequency decreases.

We followed by estimating the direction of maximum attenuation for a rock having permeabilities along two perpendicular directions. We studied the influence of frequency, length of the fluid drop, and the magnitude of permeability along each direction upon the direction of maximum attenuation.

We found that for rocks with small fractures and porosities, the attenuation of a low-frequency wave is minimum when the propagation is perpendicular to the direction of maximum permeability.

In the range of ultrasonic frequencies, the attenuation of a P-wave propagating perpendicularly to the direction of the maximum permeability is maximum when the magnitudes of the permeabilities are small, and is minimum when the magnitudes of the permeabilities are large. This result is not necessarily valid for high-porosity rocks having long pores saturated with high-viscosity fluid. Determining the direction of maximum attenuation for a wave with ultrasonic frequency requires a rigorous consideration of the specific values of crucial parameters.

REFERENCES

REFERENCES

- Akbar, N., Dvorkin, J., and Nur, A., 1993, Relating P-wave attenuation to permeability: *Geophysics*, **58**, 20-29.
- Berryman, J. G., and Blair, S. C., 1987, Kozeny-Carman relations and image processing methods for estimating Darcy's constant: *J. Appl. Phys.*, **62**, 2221-2228.
- Biot, M. A., 1956, Theory of propagation of elastic waves in a fluid-saturated porous solid, II higher frequency range: *J. Acoust. Soc. Am.*, **28**, 179-191.
- Mavko, G.M. and Nur, A., 1979, Wave attenuation in partially saturated rocks: *GEOPHYSICS*, **44**, 161-178.
- Lucet, N., 1989, Vitesse et atténuation des ondes élastiques soniques et ultrasoniques dans les roches sous pression de confinement: Thèse de Doctorat de l'Université Paris 6.
- Tarif, P., 1986, Mesure de l'atténuation des ondes compressionnelles dans les roches: Application à la mesure de l'anisotropie d'atténuation: Thèse de Doctorat de l'Université Paris 7.
- White, J.E., 1983, *Underground sound*: Elsevier.
- Winkler, K. W., 1979, The effects of pore fluids and frictional sliding on seismic attenuation: Ph.D. Thesis, Stanford University.

CHAPTER 3

Seismic Signatures of Reservoir Transport Properties and Pore Fluid Distribution

ABSTRACT

We investigate the effects of permeability, frequency, and fluid distribution on the viscoelastic behavior of rock. The viscoelastic response of rock to seismic waves depends on the relative motion of pore fluid with respect to the solid phase. Fluid motion depends, in part, on the internal wave-induced pore pressure distribution that relates to the pore microstructure of rock, and the scales of saturation. We consider wave-induced squirt fluid flow at two scales: (1) local microscopic flow at the smallest scale of saturation heterogeneity (e.g., within a single pore) and (2) macroscopic flow at a larger scale of fluid-saturated and dry patches. We explore the circumstances under which each of these mechanisms prevails. We examine such flows under the conditions of uniform confining (bulk) compression and obtain the effective dynamic bulk modulus of rock. The solutions are formulated in terms of generalized frequencies that depend on frequency, saturation, fluid and gas properties; and on the macroscopic properties of rock such as permeability, porosity, and dry bulk modulus. The study includes the whole range of saturation and frequency; therefore, we provide the missing link between the low-frequency limit (Gassmann's formula) and the high frequency limit given by Mavko and Jizba. Further, we compare our model with Biot's theory and introduce a geometrical factor whose numeric value gives an indication to whether the local fluid squirt or the global (squirt and/or Biot's) mechanisms dominate the viscoelastic properties of porous materials.

The important results of our theoretical modeling are: (1) a hysteresis of seismic velocity versus saturation due to variations in fluid distributions, and (2) two peaks of acoustic wave attenuation – one at low frequency (due to the global squirt flow) and another at higher frequency (due to the local flow). Both theoretical results are well supported by experimental data.

INTRODUCTION

Wave propagation in rocks is dominated by the two solid/fluid interactions: the Biot and the squirt-flow mechanisms. Traditionally, the Biot mechanism is referred to as a macroscopic flow because it can be expressed through such macroscopic parameters as: poroelastic constants, porosity, permeability, and fluid properties. The Biot theory (e.g., Biot, 1956a) presents the only existing treatment of the problem which directly relates seismic velocities and attenuation to measurable macroscopic characteristics of a rock. Berryman et al. (1988) and Dutta and Ode (1979) extend the theory to examine the effects of partial gas saturation.

There are conclusive experimental evidences to demonstrate that in certain cases the Biot theory fails to adequately predict velocity dispersion and attenuation (e.g., Wang and Nur, 1990; Mavko and Jizba, 1991). Further, the theory predicts that increasing fluid viscosity or decreasing permeability shifts relaxation towards higher frequencies. This contradicts the observed experimental data as noted by Dvorkin et al. (1993). Winkler (1985) showed that increasing oil viscosity in Berea sandstone shifts the relaxation towards lower frequencies. Akbar et al. (1993) theoretically observed that the relaxation shifts towards lower frequencies as permeability decreases in Fontainebleau sandstones.

The Biot theory ignores the effects of fluid distribution heterogeneity within a rock on its seismic properties. It has been shown, however, that this factor is a crucial element in interpreting experimental and field data, as it directly depends on the pore space structure and the history of saturation (e.g., Domenico, 1976; Cadoret et al., 1992; Endres and Knight, 1989; Knight and Nolen-Hoeksema, 1990).

The heterogeneity of fluid distribution in a partially saturated rock manifests itself locally (i.e., within pores) and/or globally on a much larger scale. During imbibition with high driving pressure drop, the wetting phase (e.g., water) tends to saturate large pores, whereas during drainage the non-wetting phase (e.g., oil or gas) fills those pores (e.g., Moore and Slobod, 1956; Murphy et al., 1986). The dynamic bulk

modulus is most sensitive to the saturation of the thinnest pores and therefore may depend strongly on the saturation process (Knight and Nolen-Hoeksema, 1990).

The amount of oil trapped in a reservoir depends strongly on the flow rate of the driving water (e.g., Dullien, 1992); therefore, a practical application for seismic interpretation is the evaluation of residual oil saturation in reservoirs during oil recovery processes.

The saturation process may have even a greater impact on global fluid distribution and thus strongly affect the viscoelastic response of a porous material. This is particularly important at low seismic frequencies that are typical frequencies of field measurements. Reservoirs with heterogeneous permeability distribution most often develop large gas or liquid-saturated pockets (patches) during infiltration processes. An important example of this case is viscous fingering in which injected fluid (e.g., water or gas) in the enhanced oil recovery process tends to advance in high permeability structures leaving behind oil-saturated zones with smaller permeabilities.

Mavko and Nolen-Hoeksema (1993) relate ultrasonic velocities to saturation and local fluid configurations when pore fluid is unrelaxed and fluid flow is consequently blocked. The results show a good correlation with experimental data for partially and fully saturated sandstone and granite samples. White (1975) studied the speed and attenuation of seismic waves in partially saturated rocks. The model is based on idealized geometry in which fluid flows from saturated regions into spherical gas pockets.

The examination of the squirt-flow mechanism in the literature has been restricted to the pore scale, requiring the consideration of specific pore or grain-contact geometries (e.g., Palmer and Traviolia, 1980; Murphy et al., 1986; Mavko and Nur, 1979). This approach limits practical usage of the squirt-flow theories as they are not directly connected to measurable macroscopic rock properties (permeability, porosity, etc.). On the other hand, models relating bulk properties to seismic velocities ignore the viscoelastic effects (i.e., frequency dependence). These include the high frequency limit in which fluid is unrelaxed (Mavko and Jizba, 1991; Mavko and Nolen-

Hoeksema, 1993), and the low frequency limit in which fluid is in the equilibrium state (Gassmann, 1951).

Recently, attempts have been developed to relate the squirt flow mechanism to macroscopic properties of rock for the whole frequency range. Dvorkin and Nur (1993) unified the squirt and Biot's mechanisms for partially saturated rocks. However, the squirt-flow mechanism may be important in fully saturated rocks (Mavko and Jizba, 1991). Akbar et al., (1993) related the squirt mechanism to permeability using a solution based on a simplified pore geometry (needle-like pores).

In this paper we relate, using the squirt-flow mechanism, the effective dynamic bulk modulus of rock to measurable parameters such as permeability, porosity, dry bulk modulus and fluid and gas properties. The study includes the whole range of saturation and frequency; therefore, we provide the missing connection between the low-frequency limit (Gassmann's formula) and the high frequency limit (Mavko and Jizba, 1991). We investigate the influence of the fluid distribution on the viscoelastic behavior of a porous material on both local and global scales. The study includes a detailed investigation of fluid/gas dynamic interaction in individual pores. In addition, we identify the rock parameter whose value allows us to determine the mechanism (local squirt, global squirt and/or Biot's) that dominates the viscoelastic response of a porous material.

BASIC ASSUMPTIONS AND DEFINITIONS

Microscopic Squirt Flow

Microscopic (local) squirt flow refers to fluid movement at the smallest scale of heterogeneity in porous material. The material is represented by elementary microscopic units (Figure 3.1) composed of thin conduits and stiff equidimensional pores (Murphy et al., 1986; Mavko and Jizba, 1991). Thin conduits represent the pore throats that connect the large pores and thus provide the channels for the macroscopic fluid flow (Figure 3.1b,c). The permeability of the rock depends mainly on the conduit size and geometry rather than on the dimension of the large pores (e.g., Dullien, 1992; Bourbié et al., 1987). Therefore, for the microscopic squirt, we explicitly model fluid flow in the thin conduits, and describe the stiff pores merely through their compressibilities, sizes, and the properties of fluid content (gas and/or liquid). The conduit is modeled by either a needle inclusion, a two-dimensional slit, a penny-shaped crack, or a pore of a transitional geometry.

The stiff pore is modeled as sphere-like and serves as a discharge buffer for the thin conduits. The size of the unit ℓ is the distance between two adjacent stiff pores and is of the order of the average grain size. It depends on the microscopic heterogeneity scale and increases with increasing grain size, increasing clay content and cement, and deteriorating sorting (Figure 3.1b). For clean granular materials with high permeability (e.g., glass beads and ocean sediments), ℓ is of the order of the grain contact area. On the other hand, for the low permeability fractured rocks (e.g., granite and consolidated rocks), ℓ is of the order of the fracture size. In the data section, we theoretically model experimental data and show that ℓ increases with decreasing permeability.

The local flow of a compressible pore fluid occurs as long as wave-induced pressures in the conduits and stiff pores are different. We use the term “uniform saturation” to describe the cases where each of the units has the same distribution of fluid and gas at any given global saturation.

Due to periodic repeatability of a unit structure and fluid distribution, the viscoelastic response of a uniformly saturated material is similar to the response of an isolated closed unit. In this case, fluid flows from a thin conduit where the induced pressure is large due to its large compressibility (Zimmerman, 1991), to the larger equidimensional pores where the induced pressure is small.

We note the saturations of the large pores and conduits as S_H and S_D , respectively. S_D and S_H are the volumetric ratios of fluid volumes in the conduit and in the stiff pore to the total volume of the pore space in the microscopic unit. The ratio $\frac{S_D}{S_H}$ depends on the saturation and the saturation process. The total saturation of the unit, S_u , can be found from S_D and S_H as (Appendix B):

$$\phi S_u = S_D \phi_D + S_H \phi_H, \quad (1)$$

where ϕ , ϕ_D , and ϕ_H are the total, conduit, and stiff pore porosities respectively, and are defined as the ratios of the respective void volumes to the total volume of the microscopic unit.

It is practically important to distinguish between fluid flow in thin conduits and large pores: if seismic velocities and attenuation are measured on a sample where fluid tends to saturate the conduits, these measurements are likely to be interpreted in terms of permeability. On the contrary, if the fluid tends to saturate the large pores, seismic data will not be directly related to permeability. Depending on the flow rate, the latter situation may be observed during imbibition.

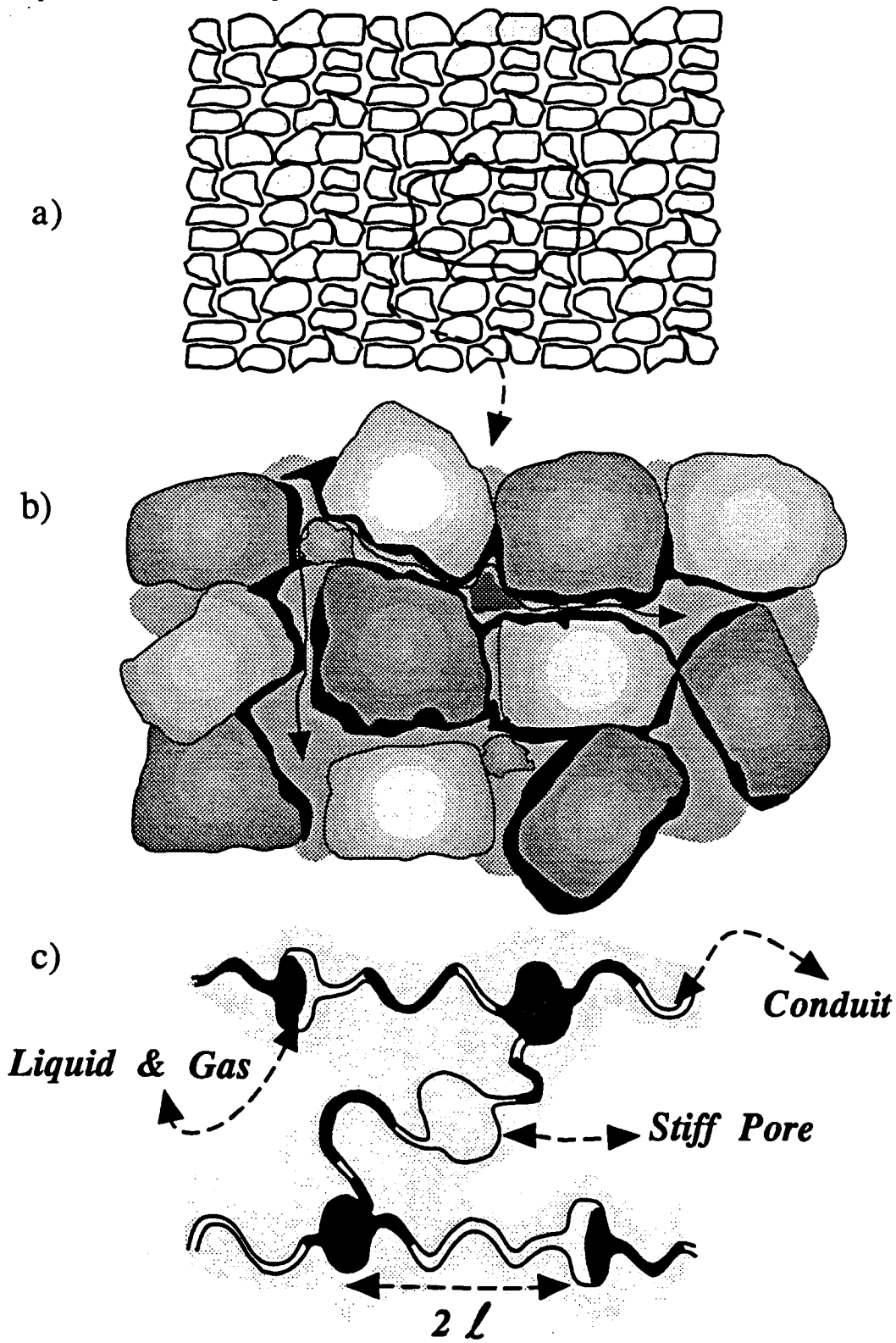


Fig. 3.1. (a) Rock is represented by an accumulation of microscopic units; (b) local fluid flow within a microscopic unit of dimension l ; and (c) a network of few microscopic units.

Macroscopic Squirt Flow

The macroscopic (global) squirt flow refers to fluid flow at the scale of fully-saturated “patches” that are much larger than the size of the microscopic unit. The macroscopic squirt flow takes place only when the saturation is spatially non-uniform. A non-uniform saturation refers to the cases when different regions of porous material have different fluid concentrations (Figure 3.2a). The sizes of the fully saturated regions depend on the saturation process and on the structure of the porous material. We represent a non-uniformly saturated porous material by a macroscopic unit of volume \tilde{V}_T that contains a single fully-saturated region of volume \tilde{R}^3 (Figure 3.2b). We introduce the symbol Ψ to denote the ratio of the volume of the fully-saturated region \tilde{R}^3 to the volume of the macroscopic unit:

$$\Psi = \frac{\tilde{R}^3}{\tilde{V}_T}. \quad (2)$$

Ψ is the measure of saturation heterogeneity in porous material. The material is uniformly saturated when $\tilde{R} = \ell$ whereas, the saturation is non-uniform when $\tilde{R} \gg \ell$. The effective saturation S can be expressed by the following equation (Appendix I):

$$S = \Psi + S_u(1 - \Psi), \quad (3)$$

where S_u is the saturation outside the fully saturated region \tilde{R}^3 and is defined by equation (1).

Ψ can be written in terms of the total saturation by introducing the symbol ψ such that $\Psi = \psi S$. Substituting this expression into equation (3), we have:

$$S = \psi S + S_u(1 - \psi S). \quad (4)$$

In other words, ψ is the volumetric ratio of the fluid that occupies \tilde{R}^3 to the total fluid volume in the macroscopic unit. If $\psi = 1$, then $S_u = 0$ and the fluid is concentrated in the volume \tilde{R}^3 .

Unlike the microscopic squirt, the macroscopic squirt can be fully described by the overall compressibility of the dry rock. We will show that the viscoelastic response of a porous material depends on both \tilde{R} and ψ .

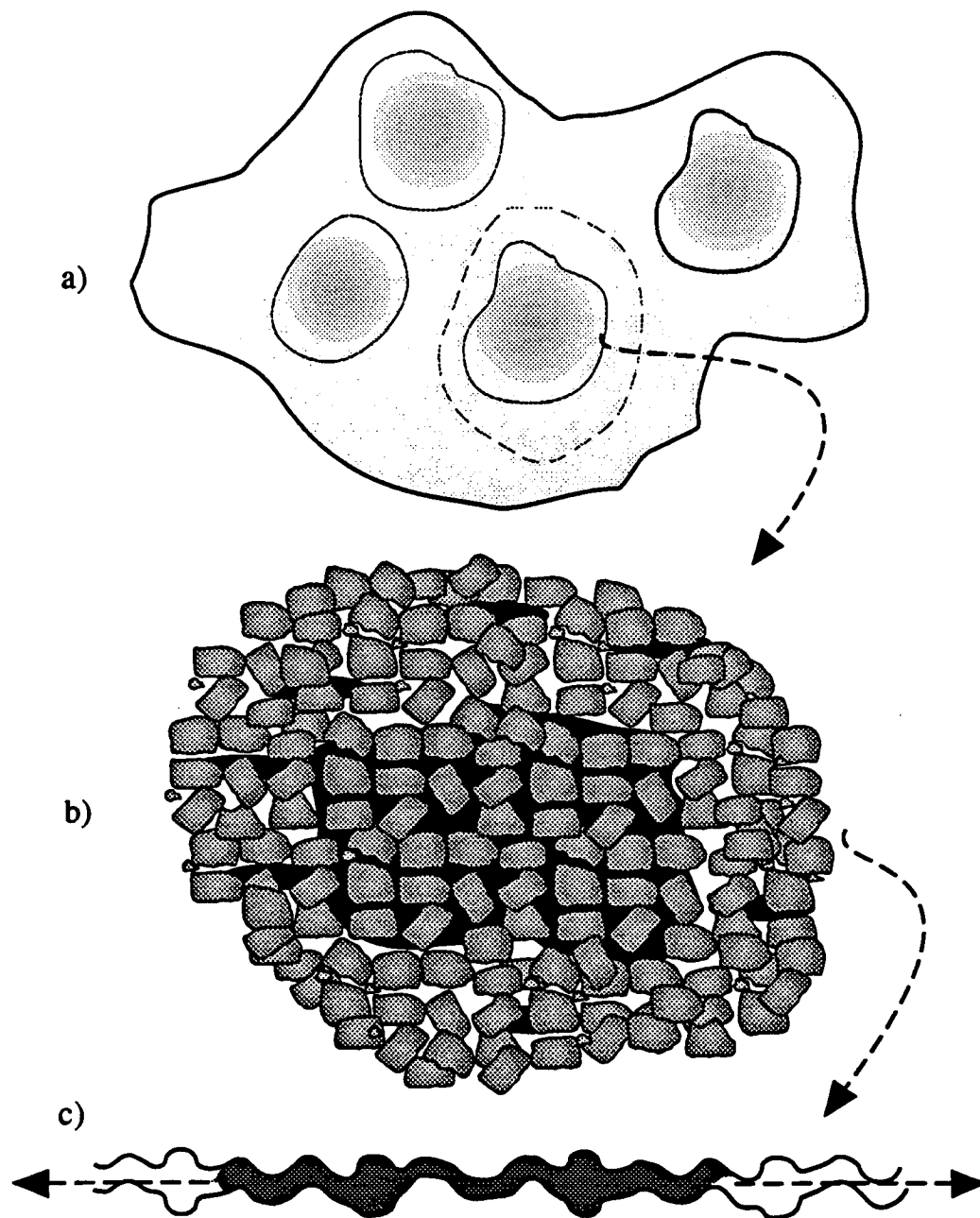


Fig. 3.2. (a) Non-uniformly saturated rock; (b) a macroscopic unit that contains a single fully-saturated region; and (c) a macroscopic conduit represented by the average pore size and compressibility.

Microscopic Versus Macroscopic Squirt

The viscoelastic effects in rock depend on the heterogeneity of internal fluid pressure. Fluid pressure is heterogeneous on the scale of the microscopic unit for uniform saturation, and on the larger macroscopic scale for non-uniform saturation.

The macroscopically saturated patch is analogous to anunjacketed fully saturated sample (fluid is allowed to escape the external boundary). If there is no flow at the sample's surface, squirt flow will occur only on the microscopic scale (jacketed sample). For low-frequency experiments (in situ and resonant-bar measurements) these boundary conditions are important. For high-frequency experiments (ultrasonic pulse transmission), these boundary conditions do not affect acoustic velocities.

Viscoelastic materials respond to wave excitation differently, depending on the frequency of the wave. At small frequencies, fluid is relaxed (small attenuation) causing small induced fluid pressure. At high frequencies, fluid is unrelaxed (small attenuation) and the induced fluid pressure is large (e.g., Akbar et al., 1993; Dvorkin and Nur, 1993). At an intermediate, critical frequency, a transition of the fluid phase from relaxed to unrelaxed modes takes place. This transition is usually accompanied with a peak in attenuation (Murphy, 1982).

We introduce the term “squirt number” (ξ) for both local (ξ_ℓ) and global (ξ_g) flows to describe the viscoelastic response of a saturated porous material. ξ_ℓ and ξ_g depend mainly on frequency ω , permeability k , porosity ϕ , saturation, fluid viscosity η , fluid compressibility C_f , and the compressibility of the dry rock C_o .

Using the Navier-Stokes equation for the pore fluid, we find approximate expressions for the squirt numbers ξ_ℓ and ξ_g for the above two modes of flow:

$$\xi_\ell \sim \frac{\omega \eta S^2 \ell^2 \Gamma (\phi C_f + C_o)}{\sqrt{3} k}, \quad (5)$$

$$\xi_g \sim \frac{\omega \eta \tilde{R}^2 \Gamma (\phi C_f + C_o)}{\sqrt{3} k}, \quad (6)$$

where Γ is a non-dimensional geometrical factor that depends on the nature of the fluid flow and ranges from 3/8 to unity (Appendix G).

The fluid is in the relaxed mode when $\xi \ll 1$, whereas, when $\xi \gg 1$ fluid is the unrelaxed mode. Viscoelastic effects are negligible in both of these extreme limits. $\xi \sim 1$ corresponds to a peak in attenuation. Therefore, letting $\xi_\ell = \xi_g = 1$ in equations (5) and (6), and solving for the frequency ω , we obtain an approximate relation between the critical frequencies ϖ_ℓ and ϖ_g at which attenuation peaks occur:

$$\frac{\varpi_\ell}{\varpi_g} \sim \left(\frac{\tilde{R}}{S\ell}\right)^2, \quad (7)$$

Experimentally, peaks in attenuation as a function of ξ are frequently observed. These include peaks in attenuation versus saturation (Winkelr, 1979; Murphy, 1982), versus permeability (Klimentos and McCann, 1990; Akbar et al., 1993), versus frequency and viscosity (Murphy et al., 1986; Jones, 1986; Vo-Thanh, 1990; Spencer, 1981), versus porosity (Ogushwitz, 1985), and versus grain size (Hamilton, 1972; Shumway, 1960).

In a fully saturated reservoir where fluid distribution is uniform, peak in attenuation occurs at relatively large frequencies. This is due to small values of ℓ .

When fluid distribution is non-uniform, two mechanisms contribute to attenuation. The macroscopic squirt dominates at low frequencies (since \tilde{R} is large) and occurs when $\xi_g \sim 1$. Dunn (1987) measured attenuation versus frequency in fluid-saturated porous cylinders with open boundaries (fluid was allowed to move in and out of the sample's surfaces). His results show that increasing size of the sample shifts attenuation peak towards lower frequencies. In our model, this phenomenon can be readily explained by equation (6) where \tilde{R} represents the size of the sample.

At higher frequencies, the fluid is macroscopically unrelaxed ($\xi_g \gg 1$), the macroscopic squirt attenuation decreases, and the system behaves as if it is uniformly saturated. In this case, the microscopic squirt dominates and results in another peak in attenuation at higher frequencies when $\xi_\ell \sim 1$ (since ℓ is small). A large liquid-saturated patch in a reservoir (\tilde{R} is large such that $\xi_g \gg 1$) is a special case for the microscopic squirt in which equation (5) can be used.

We expect that peaks resulting from the microscopic flow are wider than those resulting from the macroscopic flow since, in general, a porous material contains a wide spectrum of microscopic units ℓ . Two attenuation peaks can be observed only on experiments where the parameters that appear in equations (5) and (6) vary in such ranges that both local and global squirt flows contribute to attenuation. Such examples are observed in experimental data given by Paffenholz and Burkhardt (1989), Vo-Thanh (1990), and Nur et al., (1984).

THEORETICAL MODEL

Uniform Saturation

As described above, in a uniformly saturated rock, only the microscopic squirt mechanism takes place. Therefore, it is necessary to estimate the porosities and the compressibilities of the components that make up the microscopic unit.

Porosity estimates

The total porosity of a microscopic unit ϕ at any given confining pressure is:

$$\phi = \phi_D + \phi_H, \quad (8)$$

We assume that ϕ_H does not vary with confining pressure (Mavko and Jizba, 1991) and consequently any variation in ϕ (due to changes in confining pressure) corresponds to the equal variation in ϕ_D . Furthermore, we decompose ϕ_D into two parts:

$$\phi_D = \phi_C + \phi_N, \quad (9)$$

where ϕ_C decreases with the increasing overburden pressure, and represents the soft (crack-like) conduits; and ϕ_N represents the stiff needle or the elliptical pores that remain open at high overburden pressure.

Using equations (8) and (9), we have the following expression for the porosity:

$$\phi = \phi_C + \phi_N + \phi_H. \quad (10)$$

Denoting the porosity at high overburden pressure by ϕ_∞ , and assuming that $\phi_C = 0$ at this high pressure (Zimmerman, 1991; Mavko and Jizba, 1991), we have the following expression:

$$\phi_\infty = \phi_N + \phi_H. \quad (11)$$

Introducing parameter α such that

$$\phi_N = \alpha\phi_H, \quad (12)$$

we have the following two expressions:

$$\phi_H = \frac{\phi_\infty}{1 + \alpha}, \quad (13)$$

$$\phi_N = \frac{\alpha\phi_\infty}{1 + \alpha}. \quad (14)$$

The porosity of the conduit ϕ_D at any confining pressure is given in terms of α by the following expression (using equations 8 and 13):

$$\phi_D = \phi - \frac{\phi_\infty}{1 + \alpha}. \quad (15)$$

Compressibility estimates

In the following analysis (see Zimmerman, 1991, for a detailed review), we use the thermodynamic conventions in which applied external pressure and the induced-fluid pressure are positive quantities, while pore strains are negative. We use two types of pore-volume compressibility for a pore embedded in an elastic isotropic solid material. The first is C_{pc} , which represents pore compressibility at constant pore pressure and is defined as follows:

$$C_{pc} = \frac{-1}{V_o} \left[\frac{\partial V_o}{\partial \sigma_o} \right]_{\tilde{P}_p}, \quad (16)$$

where, V_o is the total volume of the pore; σ_o is the external confining pressure, and \tilde{P}_p is the internal pore pressure. The second type is C_{pp} and represents pore

compressibility at constant confining pressure and have the following expression:

$$C_{pp} = \frac{1}{V_o} \left[\frac{\partial V_o}{\partial \bar{P}_p} \right]_{\sigma_o}. \quad (17)$$

The relation between C_{pp} and C_{pc} is given by

$$C_{pp} = C_{pc} - C_s, \quad (18)$$

where C_s is the compressibility of the solid material surrounding the pore.

The bulk-volume compressibility C_{bc} of a body with volume V_T at a constant pore pressure is defined as

$$C_{bc} = -\frac{1}{V_T} \left[\frac{\partial V_T}{\partial \sigma_o} \right]_{\bar{P}_p}. \quad (19)$$

C_{bc} is the drained bulk compressibility that is equivalent to the bulk compressibility of the dry rock. The notation C_o will be used throughout this paper to denote this term.

Similarly, bulk-volume compressibility C_{bp} represents bulk compressibility at constant external pressure σ_o and has the following expression:

$$C_{bp} = \frac{1}{V_T} \left[\frac{\partial V_T}{\partial \bar{P}_p} \right]_{\sigma_o}. \quad (20)$$

The relation between C_o and C_{bp} is given by

$$C_{bp} = C_o - C_s. \quad (21)$$

The relations between C_o and pore compressibilities C_{pc} , and C_{pp} are

$$\phi C_{pc} = C_o - C_s, \quad (22)$$

$$\phi C_{pp} = (C_o - C_s) - \phi C_s. \quad (23)$$

In the case of multiple pores, we use the superscripts D , N , C , and H to denote the compressibilities of an average conduit, needle and crack-like conduits, and stiff pores, respectively. C_{pp}^H represents, for example, the stiff pore compressibility at constant confining pressure.

Consider that the total pore volume V_o is decomposed into two separate volumes V_o^D and V_o^H as follows:

$$V_o = V_o^D + V_o^H, \quad (24)$$

where V_o^D ($V_o^D = V_o^C + V_o^N$) and V_o^H are the volumes of the conduit and the stiff pore, respectively. V_o^C and V_o^N are the volumes of the crack-like and needle-like conduits, respectively.

Taking the derivative of equation (24) with respect to σ_o , and making use of equation (16), the overall effective compressibility \tilde{C}_{pc} of a two-pore system (the conduit and the stiff pore) with respect to the external stress can be written in the following form:

$$\phi \tilde{C}_{pc} = \phi_D \tilde{C}_{pc}^D + \phi_H C_{pc}^H, \quad (25)$$

with,

$$\phi_D \tilde{C}_{pc}^D = \phi_C C_{pc}^C + \phi_N C_{pc}^N, \quad (26)$$

where \tilde{C}_{pc}^D is the overall effective conduit compressibility. C_{pc}^C and C_{pc}^N are the compressibilities of the crack-like and needle-like conduits, respectively; $\phi = V_o/V_T$; $\phi_D = V_o^D/V_T$; $\phi_H = V_o^H/V_T$; $\phi_C = V_o^C/V_T$; and $\phi_N = V_o^N/V_T$.

The overall effective pore space compressibility \tilde{C}_{pc} can be written in terms of macroscopic measurable compressibilities C_o and C_s using equation (22) as follows:

$$\begin{aligned} \phi \tilde{C}_{pc} &= \phi_C C_{pc}^C + \phi_N C_{pc}^N + \phi_H C_{pc}^H \\ &= \phi_D \tilde{C}_{pc}^D + \phi_H C_{pc}^H \\ &= C_o - C_s. \end{aligned} \quad (27)$$

Similarly, taking the derivatives of both parts of equation (24) with respect to \tilde{P}_p , we can find the overall effective compressibility \tilde{C}_{pp} in the case of multiple pores with respect to the internal pore pressure. The result is:

$$\phi \tilde{C}_{pp} = \phi_D \tilde{C}_{pp}^D + \phi_H C_{pp}^H, \quad (28)$$

where,

$$\phi_D \tilde{C}_{pp}^D = \phi_C C_{pp}^C + \phi_N C_{pp}^N. \quad (29)$$

The effective pore space compressibility \tilde{C}_{pp} can be expressed through C_o and C_s using equation (23) as follows:

$$\begin{aligned} \phi \tilde{C}_{pp} &= \phi_C C_{pp}^C + \phi_N C_{pp}^N + \phi_H C_{pp}^H \\ &= \phi_D \tilde{C}_{pp}^D + \phi_H C_{pp}^H \\ &= (C_o - C_s) - \phi C_s. \end{aligned} \quad (30)$$

Taking the limit of equation (27) of high applied stress and noting that at high stress $\phi_C = 0$, we find:

$$C_o^\infty - C_s = \phi_N C_{pc}^N + \phi_H C_{pc}^H, \quad (31)$$

where C_o^∞ is the compressibility of the dry rock at high confining stress, at which thin cracks are closed (Mavko and Jizba, 1991; Zimmerman, 1991).

Following our approach in the porosity analysis, we introduce a parameter β such that:

$$C_{pc}^N = \beta C_{pc}^H. \quad (32)$$

Substituting with this expression into equation (31), and using the relation $\phi_N = \alpha \phi_H$, we obtain the following expressions for C_{pc}^N and C_{pc}^H :

$$C_{pc}^N = \beta \frac{C_o^\infty - C_s}{\phi_H(\gamma + 1)}, \quad (33)$$

$$C_{pc}^H = \frac{C_o^\infty - C_s}{\phi_H(\gamma + 1)}, \quad (34)$$

where the symbol γ is used instead of the group $\alpha\beta$

The importance of β is that it represents conduit compressibility at any pressure. This can be seen by substituting with equation (34) into equation (27), making use of the relation $\phi_N = \alpha \phi_H$, and solving for $\phi_D \tilde{C}_{pc}^D$:

$$\phi_D \tilde{C}_{pc}^D = C_o - C_s - \frac{C_o^\infty - C_s}{(\gamma + 1)}. \quad (35)$$

Similarly, \tilde{C}_{pp}^D may be expressed through C_o as follows. Solving for $\phi_D \tilde{C}_{pp}^D$ from equation (30), and making use of the relation $C_{pp}^H = C_{pc}^H - C_s$, that follows from equation (18), we obtain:

$$\phi_D \tilde{C}_{pp}^D = C_o - C_s - \phi C_s - \phi_H (C_{pc}^H - C_s).$$

Substituting into the previous equation with the value of C_{pc}^H from equation (34), and noting the relation $\phi_D = \phi - \phi_H$ that follows from equation (8), we obtain the following expression for $\phi_D \tilde{C}_{pp}^D$:

$$\phi_D \tilde{C}_{pp}^D = C_o - \phi_D C_s - \frac{C_o^\infty + \gamma C_s}{(\gamma + 1)}. \quad (36)$$

Comparing equation (35) with equation (36), we notice readily that a simple relation $\tilde{C}_{pp}^D = \tilde{C}_{pc}^D - C_s$ that is analogous to equation (18) is satisfied.

Equations (13), (14), (33), (34,) (35,) and (36) are the basis for transforming the microscopic parameters, via estimating α and β , into the macroscopic parameters C_o and C_s that can be estimated from available data.

Relations between α , β , ℓ , and the bulk properties

As will be shown later, the frequency-dependent pore fluid pressure depends on the microscopic details of the compressibilities and porosities of the conduits and the stiff pores. It is necessary, therefore, to relate these unknown microscopic parameters to the known macroscopic parameters such as porosity ϕ , permeability k , and the overall compressibility of the dry rock C_o .

Two parameters α and β are needed for relating the microscopic to the macroscopic parameters for a given rock. α is a numeric parameter that represents the ratio of conduits porosity to stiff pore porosity at high confining pressure; β represents the ratio of the compressibility of the conduit to the compressibility of the stiff pore at high confining pressure.

To estimate α and β , we require the evaluations of the parameters ϕ_∞ and C_o^∞ , that as described above, represent porosity and dry rock compressibility at high confining pressure.

It is worth noting that the effects of fluid flow on the induced pore pressure depends on the combination $\alpha\beta$ (see the hydrodynamic section of this paper), that was defined above by the symbol γ .

γ represents the volume-weighted ratio of the compressibilities of the conduit and the stiff pore at high confining pressure. Below, we relate γ to rock properties and show that γ is the geometrical factor that governs the viscoelastic response of a porous material.

Case $\alpha \sim 0$

We begin the description of our approach by investigating the case in which permeability decreases dramatically with increasing confining pressure, due to crack closure. The permeability and porosity for these types of rocks are small and depend on fracture size and distribution. Examples of this case can be seen in granite, quartzite, and consolidated and fractured rocks (Brace et al., 1969; Zoback, 1975; Coyner, 1977; and Walls, 1983).

In this case $\alpha \approx 0$, and the representative conduit is mainly composed of soft cracks (i.e., ℓ is large) that close up at high confining pressure (Zimmerman, 1991) while the stiff portion of the conduit is small, i.e., $\phi_N \approx 0$, see equation (14). In the data section, we show that ℓ increases with decreasing permeability. Therefore, the local fluid flow from crack-like conduits, where fluid pressure is large, to stiff pores intensifies at the expense of the macroscopic fluid flow which is effectively blocked due to thin cracks (Figure 3.3a). This theoretical picture agrees with the observed experimental data which show that local flow mechanism dominates the global Biot's effects for this type of rock (Mavko and Nur, 1979).

Joining the expression $\phi_H \approx \phi_\infty$ from equation (13) and with equation (8), we express the conduit porosity ϕ_D at any confining pressure in terms of the known values of ϕ and ϕ_∞ as follows:

$$\phi_D \approx \phi - \phi_\infty. \quad (37)$$

Similarly, using $\alpha \approx 0$ in equation (34), we express the unknown value of C_{pc}^H in terms of C_o^∞ and C_s , as follows:

$$\phi_H C_{pc}^H \approx C_o^\infty - C_s. \quad (38)$$

Case $\alpha \sim 1$

Granular rocks with intermediate permeabilities and porosities exhibit small decrease in permeability with increasing confining pressure. Permeability and porosity in this case are determined grain to grain contacts and fractures (Figure 3.3b). Therefore, the representative conduit is composed of both stiff pores that remain open and soft cracks that close up at high confining pressure. It follows that (when $\alpha \sim 1$) the conduit porosity ϕ_D increases and approaches ϕ_H , and the microscopic squirt distance ℓ for these type of rocks are smaller than the previous cases of fractured rocks. Therefore, fluid pressure in stiff pores approaches pressure in conduits, which reduces the effects of local fluid flow.

Equations (13) and (15) show that ϕ_H decreases with increasing α , while ϕ_D increases and approaches ϕ . Therefore, increasing α enhances the effects of macroscopic fluid flow at the expense of local fluid flow that occurs from conduit to stiff pore. Examples of this case can be seen in moderately sorted rocks with traces of clay and cement, e.g., Berea, Bandera, and Boise sandstones (Gregory, 1976).

Case $\alpha \sim \infty$

Well sorted clean granular materials (e.g., glass beads and ocean sediments) in which geometry of pore space is determined by grain to grain contacts tend to have large permeability and porosity. The variation of permeability with the confining pressure is negligible due to the absence of cracks. In this case, the microscopic squirt length ℓ is of the order of the grains contact area (Figure 3.3c). This corresponds to very large values of α , and the squirt flow of fluid from conduit to the stiff pore

is insignificant. This can be seen by noting that $\phi_H = 0$ in equation (13) when $\alpha \rightarrow \infty$. Therefore, the global mechanism dominates the viscoelastic response of porous material. This agrees with the fact that attenuation in saturated rocks with high permeability and porosity is dominated by the global Biot's mechanism (e.g., Johnston et al., 1978). Furthermore, substituting with α into equation (35), and noting that in this case $\phi_D = \phi$, that follows from equation (15), we obtain the following expression for conduit compressibility:

$$\phi \tilde{C}_{pc}^D = C_o - C_s. \quad (39)$$

This equation is similar to equation (22) that relates the compressibility of a single pore to the bulk compressibility.

Limits imposed on β

When β approaches unity ($\beta \approx 1$), the compressibility of the representative conduit at large confining pressure becomes close to the compressibility of the stiff pore. If we assume that the stiff pore can be represented by a sphere, then the representative conduit will have a needle-like shape (since the compressibility of a needle-like conduit is approximately equal to the compressibility of a sphere, Zimmerman, 1991).

On the other hand, the conduit compressibility is much larger than that of the stiff pore when β is large. This corresponds to a representative conduit with an elliptical cross section (Zimmerman, 1991).

Upper and lower bounds for the value of β are estimated as follows (Appendix J):

$$\frac{\pi \mu C_o^\infty (1 + \alpha)}{2\alpha(1 - \nu)\phi_\infty} - \frac{1}{\alpha} > \beta \geq 1, \quad (40)$$

where μ , ν are the shear modulus and Poisson's ratio of the matrix material (grains) respectively.

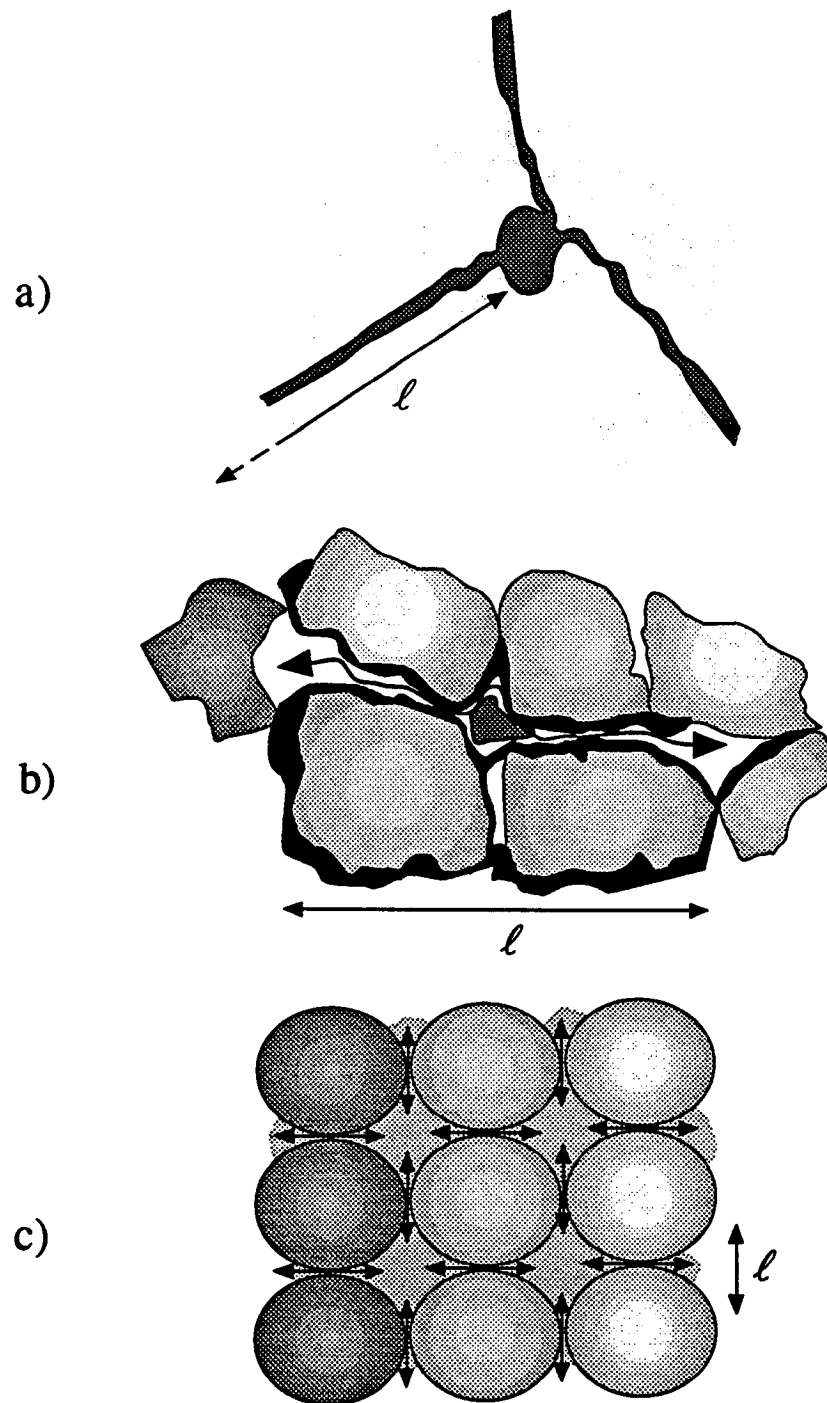


Fig. 3.3. Graphic images for the relations between the geometrical factor α and the microscopic structure of the rocks. (a) $\alpha \sim 0$ corresponds to fractured rocks; (b) $\alpha \sim 1$ corresponds to fractured granular materials; and (c) $\alpha \sim \infty$ corresponds to well-sorted clean granular materials.

Hydrodynamics

We examine the squirt-flow mechanism in a rock subject to bulk compression by specifying three distinct geometries of the conduits: a needle-like crack; a two-dimensional crack; and a penny-shaped crack. Fluid flow in the first two pores takes place along one direction (unidirectional flow), whereas in the penny-shape cracks, the flow diverges radially from the center of the fluid droplet (radial flow). One of our main goals is to investigate the effects of conduit geometry on the dynamically induced fluid pressure. This allows us to construct a general solution for the induced fluid pressure in a variety of conduit shapes.

We assume that the geometries of the needle-like conduit and the three-dimensional crack represent the end members of crack population (considering their effects on fluid pressure). This assumption is based on the fact that the compressibilities of these two geometries represent the end members of conduits of varying aspect ratio that is defined as the ratio of the minor to the major axes of conduit cross section (Zimmerman, 1991). At bulk compression, the conduit compressibility is maximum for a three-dimensional crack (small aspect ratio) and is minimum for a needle-like conduit (aspect ratio is unity).

The average induced fluid pressures for unidirectional flow (needle-like and two dimensional crack) are the same as long as the solutions are written in terms macroscopic parameters such as permeability and porosity (Appendix F).

The induced fluid pressure in the penny-shaped crack (Appendix E) is compared with the pressure in the unidirectional flow to estimate the effects of the nature of fluid flow (i.e., unidirectional versus radial) on the fluid pressure (Appendix G).

We find that the induced fluid pressure in the case of radial flow can be obtained from the formula for the unidirectional flow by introducing a non-dimensional factor Γ into the latter (Appendix G). Γ is unity for unidirectional flow, and is equal to $\frac{3}{8}$ for the radial flow. Therefore, the fluid pressure for any transitional conduit geometry between these end members, including the effects of fluid divergence, can be estimated from the unidirectional case by assigning a certain value to the factor Γ . This method is identical to that of Biot (1956b) in which “the structural factor” is introduced to correct for the pore geometry.

It is worth noting that the variation of Γ (i.e., $1 \geq \Gamma \geq \frac{3}{8}$) is insignificant with respect to the variations of the other parameters (such as permeability, frequency, squirt lengths, viscosity, etc.) involved in the calculation of the fluid pressure.

This observation has an important practical implication: the fluid pressure for a simple conduit geometry (e.g., needle) can be easily generalized to include other, more complex geometries, as long as the solution is written in terms of permeability and porosity. This result features the importance of permeability as a macroscopic parameter.

Average fluid pressure

In appendices C and D, we calculate the average fluid pressures \tilde{P}_1 and \tilde{P}_2 in a needle-like and a two-dimensional conduit respectively. \tilde{P}_1 and \tilde{P}_2 represent the end-members for unidirectional fluid flow in two-dimensional conduits with elliptical cross sections. In appendix F, we show that \tilde{P}_1 and \tilde{P}_2 can have the same expression \tilde{P}_u when both are expressed in terms of permeability and porosity. In appendix E, we calculate fluid pressure \tilde{P}_r in a three-dimensional conduit (radial fluid flow). \tilde{P}_u is compared with \tilde{P}_r in appendix G to estimate the effects of radial flow on fluid pressure, and find a general expression \tilde{P}_l for fluid pressure in terms of Γ .

The average induced fluid pressure \tilde{P}_l due to an external harmonic confining loading σ_o with a unit magnitude in any transitional conduit geometry, including the

effects of the radial flow, is (Appendix G):

$$\tilde{P}_\ell = \frac{\tilde{P}_\ell|_{\tilde{\Omega}_\ell=0} - \tilde{P}_\ell|_{\tilde{\Omega}_\ell=\infty}}{(1 - \tilde{C})(\tilde{\Omega}_\ell \coth \tilde{\Omega}_\ell - 1) + 1} + \tilde{P}_\ell|_{\tilde{\Omega}_\ell=\infty}, \quad (41)$$

where $\tilde{\Omega}_\ell$ is the generalized frequency for the local fluid flow. This parameter has the following expression:

$$\tilde{\Omega}_\ell^2 = \left(\frac{\omega \eta C_f \phi_D S_D^2 \ell^2}{k} \right) \mathcal{F}(C, S_u, \phi) i, \quad (42)$$

where i is $\sqrt{-1}$ and $\mathcal{F}(C, S_u, \phi)$ is given by:

$$\mathcal{F}(C, S_u, \phi) = \frac{(\tilde{C}_{pp}^D + C_f)\Gamma}{C_f}. \quad (43)$$

Γ is unity for unidirectional flow and is equal to $\frac{3}{8}$ for radial flow (Appendix G). $\tilde{P}_\ell|_{\tilde{\Omega}_\ell=0}$ is the fluid pressure in the conduit, \tilde{P}_ℓ , in the limit when $\tilde{\Omega}_\ell \rightarrow 0$ and is equal to:

$$\tilde{P}_\ell|_{\tilde{\Omega}_\ell=0} = \frac{C_o - C_s}{\phi C_e}. \quad (44)$$

$\tilde{P}_\ell|_{\tilde{\Omega}_\ell=\infty}$ is the fluid pressure in the conduit, \tilde{P}_ℓ , when $\tilde{\Omega}_\ell \rightarrow \infty$ and is given by:

$$\tilde{P}_\ell|_{\tilde{\Omega}_\ell=\infty} = \frac{(C_o - C_o^\infty) + \gamma(C_o - C_s)}{(C_o - C_o^\infty) + \gamma(C_o - C_s) + \phi_D(1 + \gamma)(C_f - C_s)}. \quad (45)$$

\tilde{C} is given in terms of compressibilities C_h , and C_e as follows:

$$\tilde{C} = \frac{\phi_D C_h}{\phi C_e}, \quad (46)$$

where C_h is the effective compressibility of the saturated part of the conduit and is given by

$$\phi_D C_h = \frac{(C_o - C_o^\infty) + \gamma(C_o - C_s) + \phi_D(1 + \gamma)(S_D C_f - C_s)}{1 + \gamma}. \quad (47)$$

C_e represents the effective static compressibility of the whole pore space and its constituents, and is given by the following expression:

$$\phi C_e = C_o - C_s(1 + \phi) + S_u \phi C_f + (1 - S_u) \phi C_g, \quad (48)$$

where C_g is the gas compressibility.

The pressure in the gas and in the fluid that occupies the equidimensional pore is (Appendix B):

$$\tilde{P}_H = \frac{\tilde{P}_\ell|_{\tilde{\Omega}_\ell=0} - \tilde{C}\tilde{P}_\ell}{1 - \tilde{C}}. \quad (49)$$

The volumetric average pressure in the whole pore space \tilde{P}_E is:

$$\tilde{P}_E = \frac{S_D\phi_D}{\phi} \{\tilde{P}_\ell - \tilde{P}_H\} + \tilde{P}_H. \quad (50)$$

Comparing equations (44) and (45), we notice that the average fluid pressure depends on the details of pore structure in the limit $\tilde{\Omega}_\ell \rightarrow \infty$. This dependence is through the parameters α and β . In the limit when $\tilde{\Omega}_\ell \rightarrow 0$, the fluid pressure depends merely on the bulk compressibility C_o .

Furthermore, equations (41), (49), and (50) indicate that in the limit of $\tilde{\Omega}_\ell \rightarrow 0$, $\tilde{P}_\ell = \tilde{P}_H = \tilde{P}_E$. This equality reflects the state of equilibrium in the pore space at small $\tilde{\Omega}_\ell$.

Setting the second derivative of the fluid pressure with respect to frequency, as given by equation (41), to zero, one can show that a transition of the fluid phase in the conduit from relaxed to unrelaxed modes takes place whenever the following numeric condition is satisfied:

$$\left(\frac{\omega\eta C_f \phi_D S_D^2 \ell^2}{k}\right) \mathcal{F}_c(C, S_u, \phi) = 1, \quad (51)$$

where $\mathcal{F}_c(C, S_u, \phi)$ is related to $\mathcal{F}(C, S_u, \phi)$ by the following expression:

$$\mathcal{F}_c(C, S_u, \phi) = \frac{1 - \tilde{C}}{\sqrt{3}} \mathcal{F}(C, S_u, \phi). \quad (52)$$

Equation (51) can be used to find, for example, the critical frequency ω_ℓ ($\omega_\ell = 2\pi f$) at which the state of the fluid in the conduit changes from relaxed to unrelaxed modes:

$$\omega = \omega_\ell = \frac{k}{\eta C_f S_D^2 \phi_D \ell^2} \frac{1}{\mathcal{F}_c(C, S_u, \phi)}. \quad (53)$$

Non-Uniform Saturation

In the previous section, we calculated fluid pressure in a special case when fluid is uniformly distributed throughout the rock. Below, we investigate the general case in which fluid is arbitrary distributed throughout the rock.

Consider the case where different parts of the porous material have different fluid concentrations (Figure 3.2a). We model this case by a representative macroscopic unit of volume \hat{V}_T that contains a single fully-saturated region of volume \tilde{R}^3 . By definition, the volume \tilde{R}^3 is surrounded by either a dry or partially saturated region with saturation S_u . We introduce a new parameter Ψ (Ψ is a saturation coefficient) defined as the ratio: $\Psi = \tilde{R}^3/\hat{V}_T$.

Since fluid phase is continuous throughout \tilde{R}^3 , any variation in pore volume, due to a harmonic confining stress acting on the external boundaries of the body, will result in increasing fluid pressure. At small frequencies, fluid behaves as if it is incompressible, and consequently, the flow from the region \tilde{R}^3 will depend mainly on the average pore shape and compressibility that can be related to the permeability, porosity, and to the bulk compressibility of the rock. This observation is confirmed by equation (44) where fluid pressure in a microscopic unit depends on the average pore space compressibility at small frequencies. At certain larger frequencies, the details of the microstructure become important, and fluid flow within the volume \tilde{R}^3 takes place on both microscopic and macroscopic scales.

At high frequencies, fluid is macroscopically unrelaxed (Akbar et al., 1993), and fluid flow takes place only within the microscopic units that make up the volume \tilde{R}^3 . The latter case corresponds to the previously discussed microscopic squirt flow when $S_u = 1$.

In our model, we calculate the average induced fluid pressure \tilde{P}_G when the microscopic fluid flow is negligible with respect to the macroscopic flow. Therefore, fluid flow depends on the average pore size (total porosity ϕ), permeability k , and average pore compressibilities defined by equations (22) and (23) (Figure 3.2c).

Average fluid pressure

We examine the macroscopic squirt-flow mechanism within the region \tilde{R}^3 subject to a harmonic bulk compression. Fluid flow takes place in a macroscopic conduit with compressibilities defined by the effective pore compressibilities \tilde{C}_{pc} and \tilde{C}_{pp} which are related to C_o and C_s through equations (22) and (23).

The induced fluid pressure \tilde{P}_G in any transitional conduit geometry, including the effects of the radial flow is (Appendix H):

$$\tilde{P}_G = \tilde{P}_G|_{\tilde{\Omega}_g=\infty} \left[1 - \frac{1}{\tilde{\Omega}_g \coth(\tilde{\Omega}_g)} \right], \quad (54)$$

where $\tilde{\Omega}_g$ is the generalized frequency for the global fluid flow and has the following expression:

$$\tilde{\Omega}_g^2 = \left(\frac{\omega \eta C_f \phi \tilde{R}^2}{k} \right) \mathcal{X}(C, \phi) i, \quad (55)$$

$$\mathcal{X}(C, \phi) = \frac{(\tilde{C}_{pp} + C_f)}{C_f} \Gamma. \quad (56)$$

The term $\mathcal{X}(C, \phi)$ can be expressed through C_o and C_s by using equation (30).

$\tilde{P}_G|_{\tilde{\Omega}_g=\infty}$ is the average fluid pressure in the macroscopic conduit at $\tilde{\Omega}_g \rightarrow \infty$, and is given as follows (Appendix H):

$$\tilde{P}_G|_{\tilde{\Omega}_g=\infty} = \frac{(C_o - C_s)}{(C_o - C_s) + \phi(C_f - C_s)}. \quad (57)$$

Analogous to the above-described microscopic case, a transition from relaxed to unrelaxed modes takes place whenever the following numeric condition is satisfied:

$$\left(\frac{\omega \eta C_f \phi \tilde{R}^2}{k} \right) \mathcal{X}_c(C, \phi) = 1, \quad (58)$$

where $\mathcal{X}_c(C, \phi)$ is related to $\mathcal{X}(C, \phi)$ by the following expression:

$$\mathcal{X}_c(C, \phi) = \frac{\mathcal{X}(C, \phi)}{\sqrt{3}}. \quad (59)$$

The critical frequency ω_g at which fluid flow in the average conduit changes from the relaxed to unrelaxed mode is:

$$\omega = \omega_g = \frac{k}{\eta C_f \phi \tilde{R}^2} \frac{1}{\mathcal{X}_c(C, \phi)}. \quad (60)$$

Approximated Relations Between Local and Global Characteristic Frequencies

In this section, we give qualitative relations for the local and global characteristic frequencies. The compressibilities of the dry rock and the macroscopic conduit are related to the compressibilities of the individual pores (soft and stiff pores) that make up the macroscopic conduit. In first approximation, the stiff pore compressibility C_{pp}^H is much smaller than the conduit's compressibility \tilde{C}_{pp}^D ; and the compressibility of the dry rock C_o is much larger than the compressibility of the grains C_s . Using these approximations in equation (30), we have the following expression:

$$\phi_D \tilde{C}_{pp}^D \approx C_o. \quad (61)$$

When a small portion of pore space is occupied with gas, the term \tilde{C} is close to 0, which follows from equations (46), (47), and (48) since the gas compressibility is much larger than the fluid compressibility. An approximate expression for $\mathcal{F}_c(C, S_u, \phi)$, which follows from equation (52) is then:

$$\mathcal{F}_c(C, S_u, \phi) \approx \frac{(\tilde{C}_{pp}^D + C_f)\Gamma}{\sqrt{3}C_f}. \quad (62)$$

Equation (5) is found by joining equations (61), (62), and (51) and letting $\phi_D \sim \phi$ and $S_D \sim S$.

Similarly, equation (6) is found by joining equations (58), (59) and (61).

DYNAMIC BULK MODULUS AND APPLICATIONS

Using the reciprocity theorem (Appendix I), we find the dynamic bulk modulus of a saturated rock as

$$\tilde{K} = \frac{1}{C_o - (1 - \Psi)[\phi_D \tilde{C}_{pp}^D \tilde{P}_t + \phi_H C_{pp}^H \tilde{P}_H + \phi C_s \tilde{P}_E] - \Psi \tilde{P}_G (C_o - C_s)}. \quad (63)$$

Equation (63) gives the bulk modulus for a non-uniformly saturated body for the whole frequency and saturation ranges. The body contains regions with different fluid concentrations (fully or partially-saturated patches) scaled by Ψ and is surrounded by partially saturated regions that scaled by the combination $1 - \Psi$. It is assumed that the wavelength is much larger than the size of the heterogeneity. When the wavelength is of the order of the size of the heterogeneity (or less), then each heterogeneous medium can be considered separately. In the latter case, the average wave velocity can be calculated using the ray theories (e.g., Widess, 1973). Below, we present some examples to clarify the physical meaning of Ψ .

Uniform Fluid Distribution

This case corresponds to fully or partially saturated rocks without global heterogeneities (i.e., no patches), and can be subdivided into the following cases:

$\Psi = 0$: Fluid distribution is heterogeneous at the grain scale and the effect of fluid distribution (i.e., conduit versus stiff pore saturations) is contained in \tilde{P}_t , \tilde{P}_H , and \tilde{P}_E through the saturation terms S_u , S_D and S_H . Special cases for $\Psi = 0$ are: 1) measurement on a jacketed fully-saturated sample for the whole frequency range, and 2) measurement on unjacketed fully-saturated sample when the macroscopic squirt number ξ_g is much larger than unity (fluid is globally unrelaxed).

$\Psi = 1$: This is the case of low-frequency measurements on an unjacketed fully-saturated sample such that $\xi_g \sim 1$. In this case, the effects of fluid flow from conduits to stiff pores is negligible since $\xi_t \ll 1$.

Non-Uniform Fluid Distribution

In many cases of practical interest, fluid distribution in partially saturated porous material is heterogeneous at both local and global scales. The heterogeneity of fluid distribution depends strongly on the magnitude of the applied driving pressure drop of the injected fluid, and on the heterogeneity of the porous medium itself. Below, we investigate these cases separately.

Heterogeneous fluid distribution due to saturation processes

We examine a porous medium with homogeneous permeability and porosity. We distinguish between the following cases:

Fully saturated patches

$0 < \Psi < 1$: This is an important case in which the heterogeneity of fluid distribution manifests itself in terms of fully saturated patches within partially saturated medium. We distinguish between the following cases:

1) $\xi_g \gg 1$: This case corresponds to unrelaxed patches, where fluid flow takes place within the microscopic units that make up the macroscopic unit (patch). In this case the last term in equation (63) can be written as (Appendix I):

$$\Psi \tilde{P}_G(C_o - C_s) \longrightarrow \Psi[\phi_D \tilde{C}_{pp}^D \tilde{P}_\ell + \phi_H C_{pp}^H \tilde{P}_H + \phi C_s \tilde{P}_E]_{S_u=1}, \quad (64)$$

where we used the limit $S_u = 1$, since the patch is fully saturated. Applications for this situation are: a) ultrasonic pulse transmission for partially saturated rocks, and b) low-frequency measurements in reservoirs with large patches (since $\xi_g \gg 1$ due to large \tilde{R}).

2) $\xi_g \sim 1$: This corresponds to small relaxed patches, where fluid flow takes place at both microscopic (within the partially-saturated regions) and macroscopic (within the fully saturated region) scales. An example is the resonant-bar measurements. In the data section, we give an example to explain the procedures of estimating Ψ .

Partially saturated patches

This refers to cases in which a given region of the rock is partially saturated with fluid concentration that is different from the surrounding medium. In this situation, the last term in equation (63) is replaced by:

$$\Psi \tilde{P}_G(C_o - C_s) \longrightarrow \Psi[\phi_D \tilde{C}_{pp}^D \tilde{P}_t + \phi_H C_{pp}^H \tilde{P}_H + \phi C_s \tilde{P}_E]_{S_p}, \quad (65)$$

where S_p represent the saturation of the partially saturated patch.

Effects of medium heterogeneity at global scale

In this case the medium contains regions with different permeabilities which result in heterogeneous fluid distribution. This situation can be accounted for by rewriting the last term in equation (63) as

$$\Psi \tilde{P}_G(C_o - C_s) \longrightarrow \Psi[\phi_D \tilde{C}_{pp}^D \tilde{P}_t + \phi_H C_{pp}^H \tilde{P}_H + \phi C_s \tilde{P}_E]_P, \quad (66)$$

where the subscript P indicates that the term is calculated for parameters (fluid content, permeability, saturation, etc.) that characterize the heterogeneous portion of the medium (Appendix I). Equation (66) is based on the assumption that rock compressibility is uniform throughout the whole medium.

SEISMIC WAVE VELOCITIES

In this section, we calculate the velocities and attenuation of seismic waves. The calculations are based on merging the calculated bulk modulus given above by equation (63) with the solution that relates the bulk and shear moduli given by Mavko and Jizba (1991) and Dvorkin et al., (1993).

Mavko and Jizba (1991) derived a relation between the unrelaxed (high-frequency limit) bulk and shear moduli. This relation is given by the following expression:

$$\frac{1}{\mu_{dry}} - \frac{1}{\mu_u} \approx \frac{4}{15} \left(\frac{1}{K_{dry}} - \frac{1}{K_u} \right), \quad (67)$$

where μ_{dry} , and μ_u are the dry and the unrelaxed frame shear moduli of the rock, respectively. K_{dry} and K_u are the dry and the unrelaxed frame bulk moduli of the rock, respectively.

Dvorkin et al., (1993) show that equation (67) is valid for full saturation and for the whole frequency range using the following assumptions: (1) the induced fluid pressure due to the shear stress and the compressibility of thin conduit are determined by the normal component of the shear stress, and (2) the effect of this normal component is identical to that for bulk compression (Dvorkin et al., 1993).

To account for partially saturated rock, we assume that fluid in stiff pore does not affect the fluid pressure. Therefore, the shear modulus at any saturation can be calculated using the following relation:

$$\frac{1}{\mu_u} \approx \frac{1}{\mu_{dry}} - \frac{4}{15} \left(\frac{1}{K_{dry}} - \frac{1}{\tilde{K}_p} \right), \quad (68)$$

where the term \tilde{K}_p is the calculated bulk modulus at partial saturation, i.e., when fluid saturates the conduit only ($S_H = 0$).

Compressional and shear wave velocities can then be calculated from the bulk modulus given by equation (63) and from the estimated shear modulus given by equation (68).

COMPARISON WITH OTHER MODELS

Low/High frequency limits

One of the most obvious differences between fluid pressures in the uniform and non-uniform saturation is that fluid pressure in the latter case approaches zero when $\tilde{\Omega} \rightarrow 0$. Thus Gassmann's equation can be derived from our model when fluid motion is blocked. Therefore, using $\Psi = 0$ and using the limits at zero frequency ($\tilde{\Omega}_\ell = 0$) and full saturation, $S_D = S_H = S_u = 1$, in equations (41), (49), and (50), and substituting into equation (63), we arrive at Gassmann's equation (Bourbié et al., 1987):

$$\tilde{K} = \frac{\phi[C_s - C_f] + C_s - C_o}{\phi C_o[C_s - C_f] + C_s[C_s - C_o]} \quad (69)$$

Similarly, the high frequency limit given by Mavko and Jizba (1991) can be obtained by using the limit $\tilde{\Omega}_\ell \rightarrow \infty$ in equation (63).

O'Connell and Budiansky (1977)

O'Connell and Budiansky (1977) studied the frequency dependent elastic properties of a fractured solid by distinguishing among three separated regimes. In the first regime, fluid moves into (or out of) individual cracks. When fluid is connected with the external boundaries of the sample, then, at low frequency, fluid pressure will be equal to its ambient value (the drained case). The modulus of the rock in this case is unaffected by the presence of the fluid.

Second is the case when fluid is allowed to move from a crack to another without bulk flow (saturated isobaric). Third, is the case in which fluid is not allowed to move from a given crack (saturated isolated). The second case is an intermediate stage between the drained and the saturated isolated cases.

Another limit is recognized as the high fluid viscosity limit. In this case fluid is unrelaxed and crack surfaces behave as if they were glued together and the effective moduli of the solid will be unaffected by the presence of the cracks. The model predicts that two peaks in attenuation occur with characteristic frequencies ω_1 and ω_2 :

$$\frac{\omega_1 \eta C_s a^2}{8k} = 1,$$

$$\frac{\omega_2 \eta a}{c\mu} = 1,$$

where a , and c are the major and minor semiaxes of the ellipsoidal cavity, and μ is the shear modulus of the unfractured rock.

The peak at ω_2 is due to the transition from relaxed to unrelaxed shear stresses which is not considered in our model. The peak at ω_1 is due to the transition from the drained to the saturated isolated regimes. This corresponds to a special case in our model in which local flow takes place within a single conduit ($S_H = 0$ and gas pressure is small at the end of the droplet, as in Appendices B, C).

The form of the critical frequency ω_1 can be written in a form that is close to our prediction, shown by equation (5), by noting that $\ell^2 S_D^2 \sim a^2$ (see Appendix F).

The Biot's theory, Biot (1956a,b)

In this section we discuss some of the fundamental differences between the Biot and the squirt-flow mechanisms.

1) Effects of permeability and fluid distribution

Wave propagation through porous material causes two main components of solid/fluid relative displacements. The first one occurs when both solid and fluid move in the same direction which is the mechanism used in Biot's theory. Fluid pressure in this case is the same along the fluid path (i.e., along the direction of fluid flow) and does not depend on the length of the fluid channel that is related strongly to pore space tortuosity and consequently to permeability (Biot 1956b). Indeed, the tortuosity of

two different porous materials having the same permeability might be totally different. However, the length of the fluid droplet depends on the tortuosity for a given saturation (see Appendix F).

This important fact can not be considered in this described mechanism. Therefore, the permeability introduced into Biot's model merely through the thickness of the average conduit will result in a weak relation between the viscoelastic behavior, permeability, and saturation.

The second type of the solid/fluid motion occurs when the solid and fluid phases move in perpendicular directions which is the squirt flow mechanism. Fluid pressure in this case builds up as the length of the fluid droplet increases (Akbar et al., 1993; Dvorkin and Nur, 1993). The length of the fluid droplet depends on the tortuosity (for a given saturation) and consequently on the permeability. Therefore, the tortuosity affects the viscoelastic response of porous material as an independent parameter through the length of the fluid droplet. As a result, the permeability introduced into our model takes into account the thickness and the tortuosity of the pore space as well as the effects of fluid distribution (saturation patterns).

2) Critical frequencies

Dvorkin and Nur (1993), and Dvorkin et al., (1993), noted a fundamental difference between the squirt and the Biot's predictions. The critical frequency in Biot's model is written as:

$$\frac{\omega_c \rho k}{\eta \phi} = 1, \quad (70)$$

where ρ is the fluid density (Biot, 1956a). This equation predicts that increasing viscosity of the fluid and/or decreasing permeability shift the relaxation towards higher frequencies. This contradicts our predictions of equation (5) as well as some of the observed experimental data, as discussed above.

It worth noting that global squirt dominates attenuation at very small frequencies (since \tilde{R} is large) while the Biot's effects dominate at much higher frequencies. Biot's mechanism neglects the effects of local fluid flow between adjacent pores on

the viscoelastic behavior of porous material. These effects are accounted for in our squirt-flow model by introducing the parameters ℓ , α , and β . Therefore, combining the predictions of our model as given by equations (53) and (60) with the Biot's model given by equation (68), we obtain a complete description of the viscoelastic behavior of a porous material.

COMPARISON WITH DATA

Uniform Fluid Distribution

In this section, we present data sets for uniform fluid distribution where fluid flow takes place within the microscopic units while the global squirt flow does not occur (jacketed samples and/or ultrasonic frequencies).

Effects of confining pressure

Coyner (1977), measured dynamic bulk modulus, compressional V_p and shear V_s wave velocities, permeability, and porosity versus differential pressure P_{df} for dry and fully water and benzene saturated samples of Berea sandstone. The differential pressure is defined as $P_{df} = P_c - P_p$, where P_c and P_p are the external applied pressure and the internal pore pressure, respectively. The pore pressure was maintained at 100 bar throughout the measurements while the confining pressure increased from $P_c = P_p = 100$ bar to the highest pressure, $P_c = 1000$ bar. The permeability k at $P_{df} = 0$ is 70.7 mD and reduces to $k = 64.87$ mD at $P_{df} = 500$ bar. The porosity of the sample is $\phi = 17.8\%$ at $P_{df} = 0$ and is equal to $\phi_\infty = 16.98\%$ at $P_{df} = 1000$ bar.

To estimate \tilde{K} , we substitute into equation (63) parameters derived from the data: Bulk moduli of grains, water, and benzene at small confining pressure are 390, 21.8, and 11.2 kbar, respectively; $S_D = S_H = S_u = 1$ (full saturation), $\eta_w = 1$ cp (water viscosity), $\eta_b = .6$ cp (benzene viscosity), frequency $f = 0.9$ MHz, $C_o^\infty = 6.374 \times 10^{-11}$ Pa⁻¹. The bulk modulus of the water and benzene increases up to 23.4 kbar and 13.9 kbar at confining pressure of 300 bar, respectively. The dry rock compressibility, C_o , is given as a function of the confining pressure (Coyner, 1977).

Because the measurements are at very high frequency, we use $\Psi = 0$. ϕ_D at each P_{df} is calculated from the relation $\phi_D = \phi - \phi_H$, where ϕ is taken as a function of P_{df} . ϕ_H is obtained from equation (13). Figure 3.4 shows the measured bulk modulus for dry, water, and benzene-saturated Berea sandstone. Solid lines are our theoretical predictions when $\alpha = 0.15$, $\beta = 250$, $\ell = .8$ mm, and Γ varies linearly as a function of P_{df} from 1 to 3/8.

The choice of Γ is based on data fitting and the assumption that the conduit geometry for this type of rock changes from needle-like ($\Gamma = 1$) to crack-like ($\Gamma = 3/8$) as confining pressure increases. The choice of $\alpha = 0.15$ is based on the fact that permeability of Berea sandstone varies slightly with confining pressure (see discussion above on relating α to bulk properties for the case $\alpha \sim 1$).

In Figures 3.5-3.9, we calculate the attenuation and velocities of seismic waves for Berea sandstone using the same parameters used in Figure 3.4. Figures 3.5 and 3.6 show the measured V_p and V_s for water and benzene-saturated Berea sandstone, respectively. Solid lines are our theoretical predictions. Figure 3.7 shows the calculated bulk attenuation versus confining pressure for water and benzene-saturated Berea sandstone. Figure 3.8 shows the calculated attenuation for compressional wave versus confining pressure for water and benzene-saturated Berea sandstone. Figure 3.9 shows the calculated shear wave attenuation versus confining pressure for water and benzene-saturated Berea sandstone.

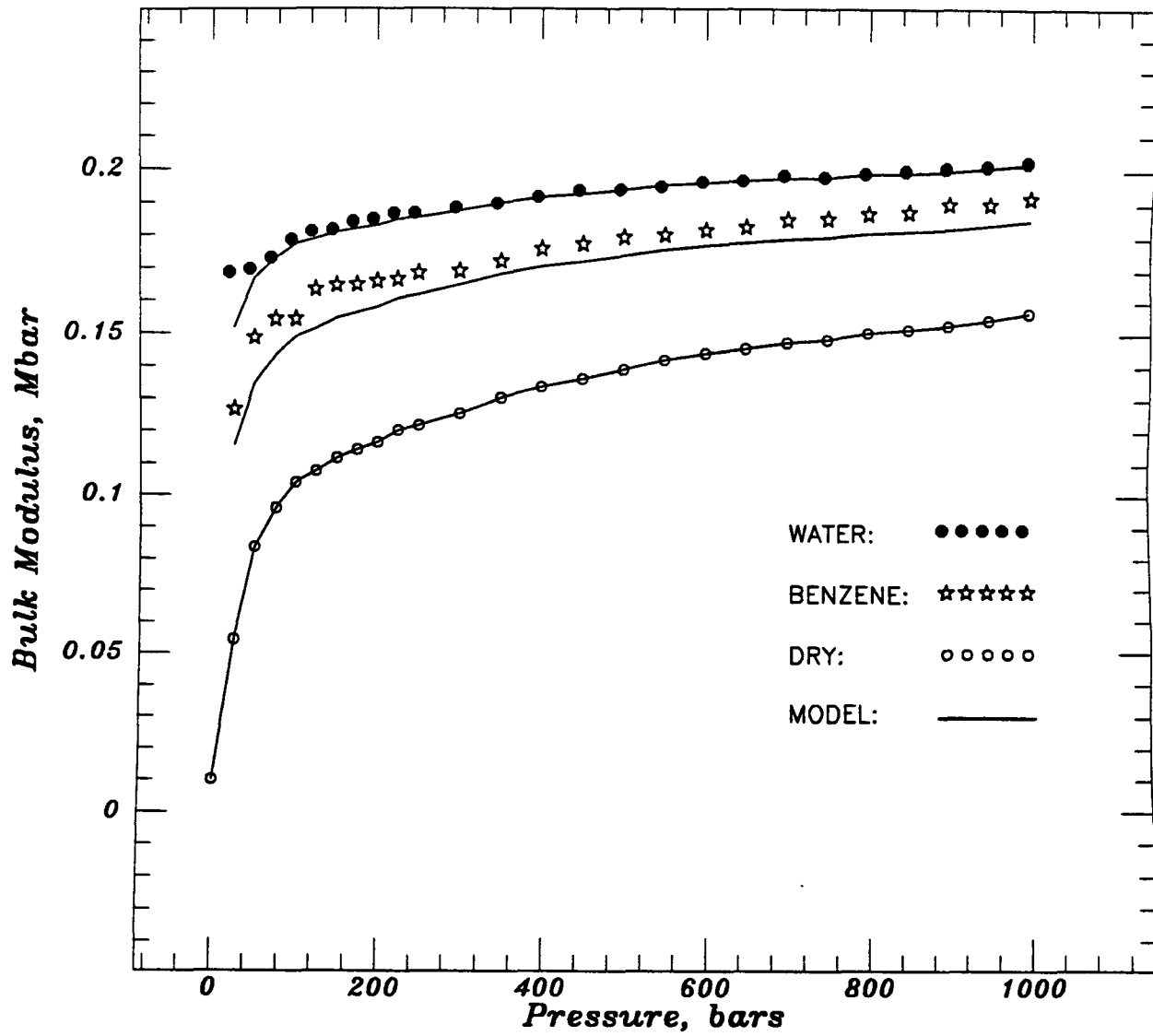


Fig. 3.4. Measured bulk modulus for dry, water-saturated, and benzene-saturated Berea sandstone versus differential pressure (Coyner, 1977). Solid lines are our theoretical predictions.

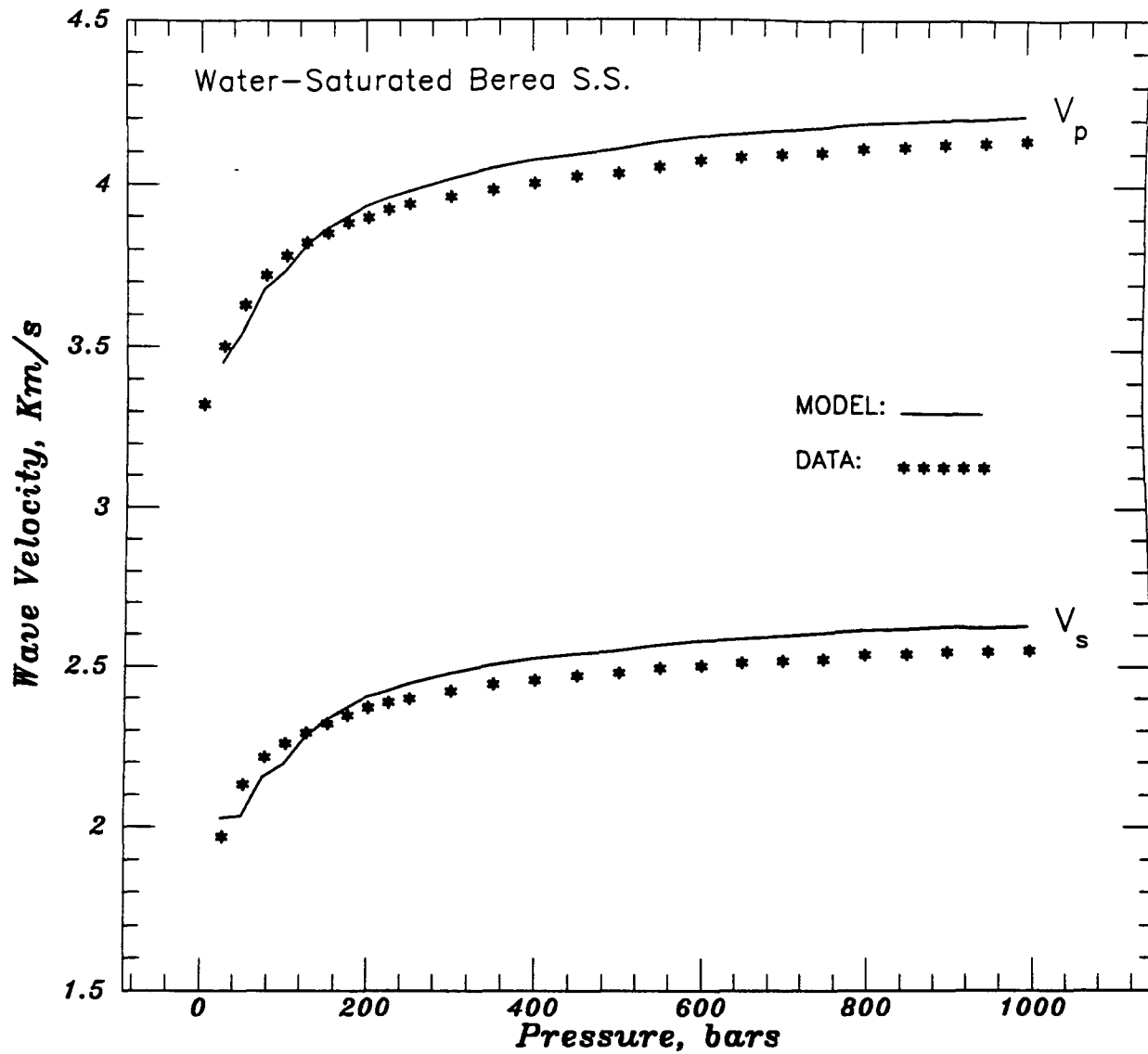


Fig. 3.5. Measured compressional and shear wave velocities V_p and V_s for water-saturated Berea sandstone versus differential pressure (Coyner, 1977). Solid lines are our theoretical predictions.

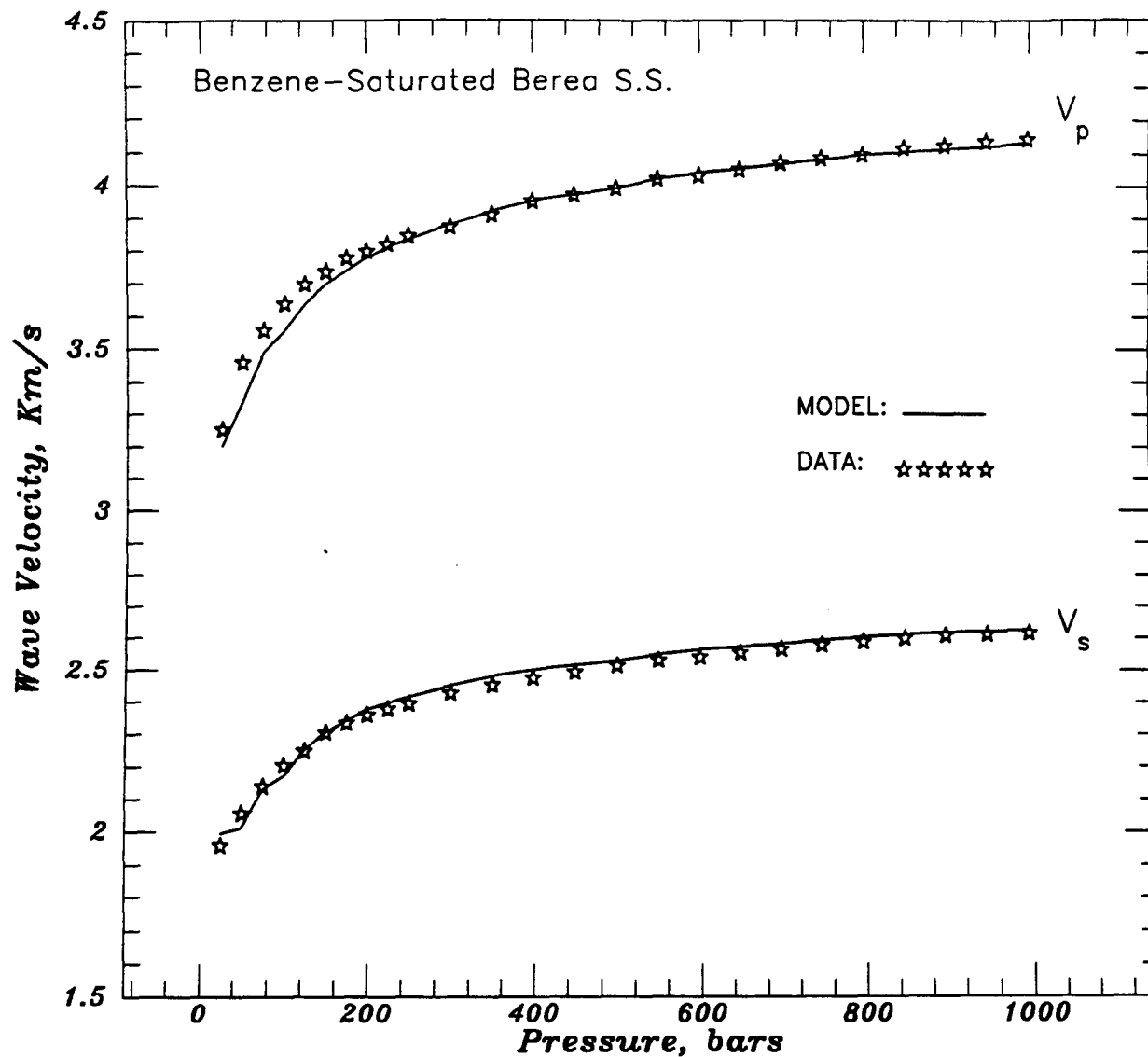


Fig. 3.6. Measured compressional and shear wave velocities V_p and V_s for benzene-saturated Berea sandstone versus differential pressure (Coyner, 1977). Solid lines are our theoretical predictions.

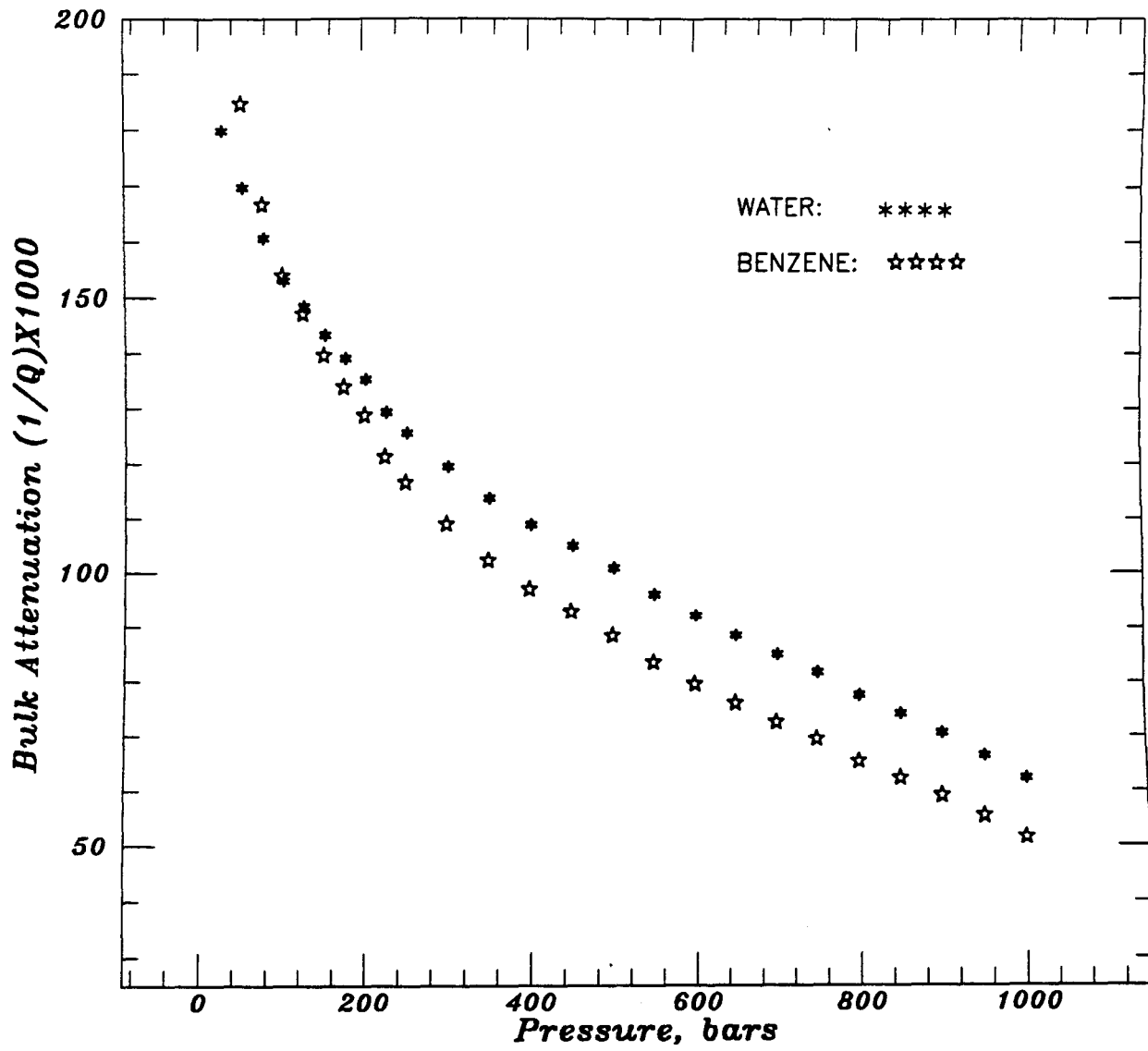


Fig. 3.7. Calculated bulk attenuation versus confining pressure for water and benzene-saturated Berea sandstone.

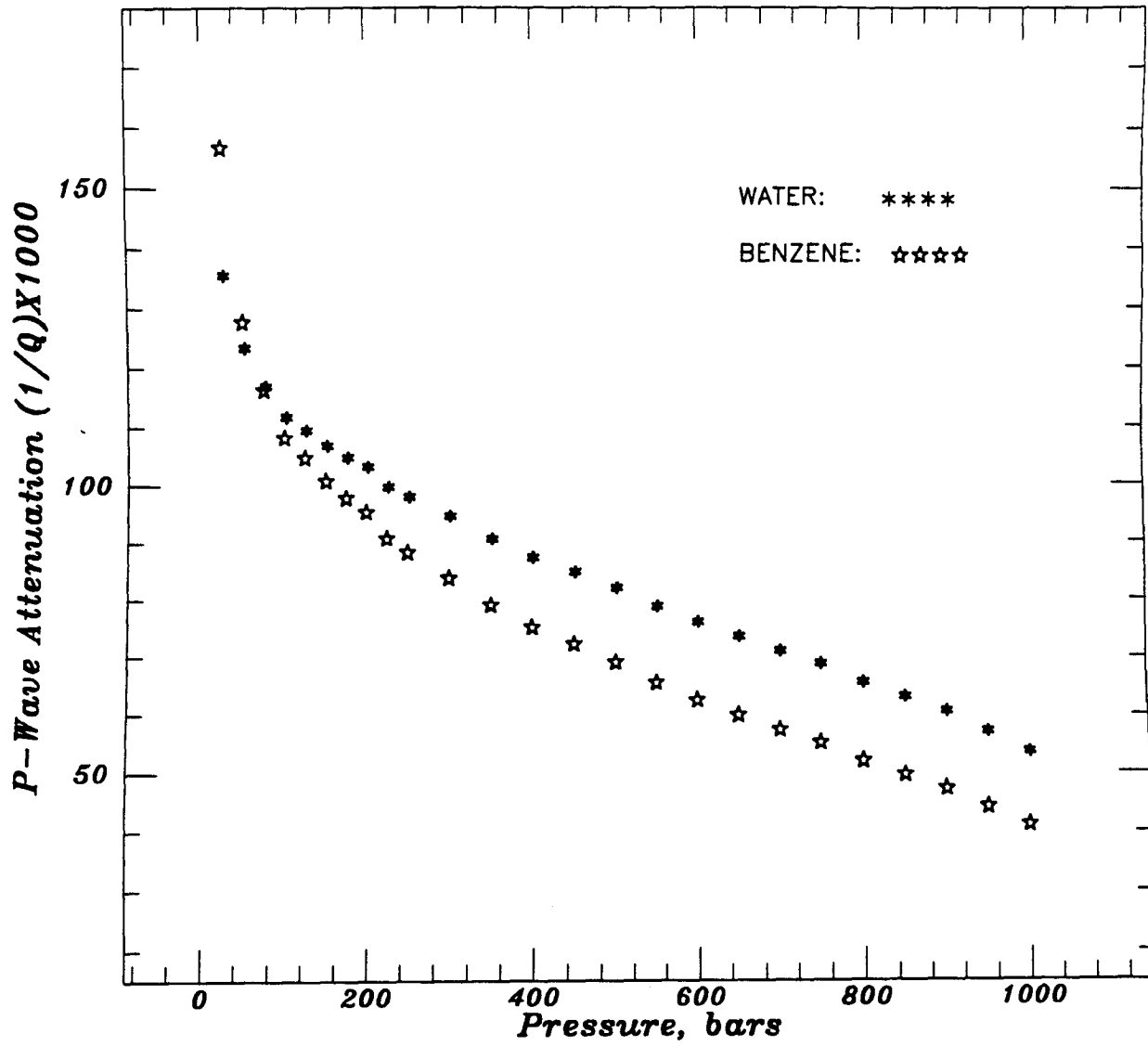


Fig. 3.8. Calculated attenuation for compressional wave versus confining pressure for water and benzene-saturated Berea sandstone.

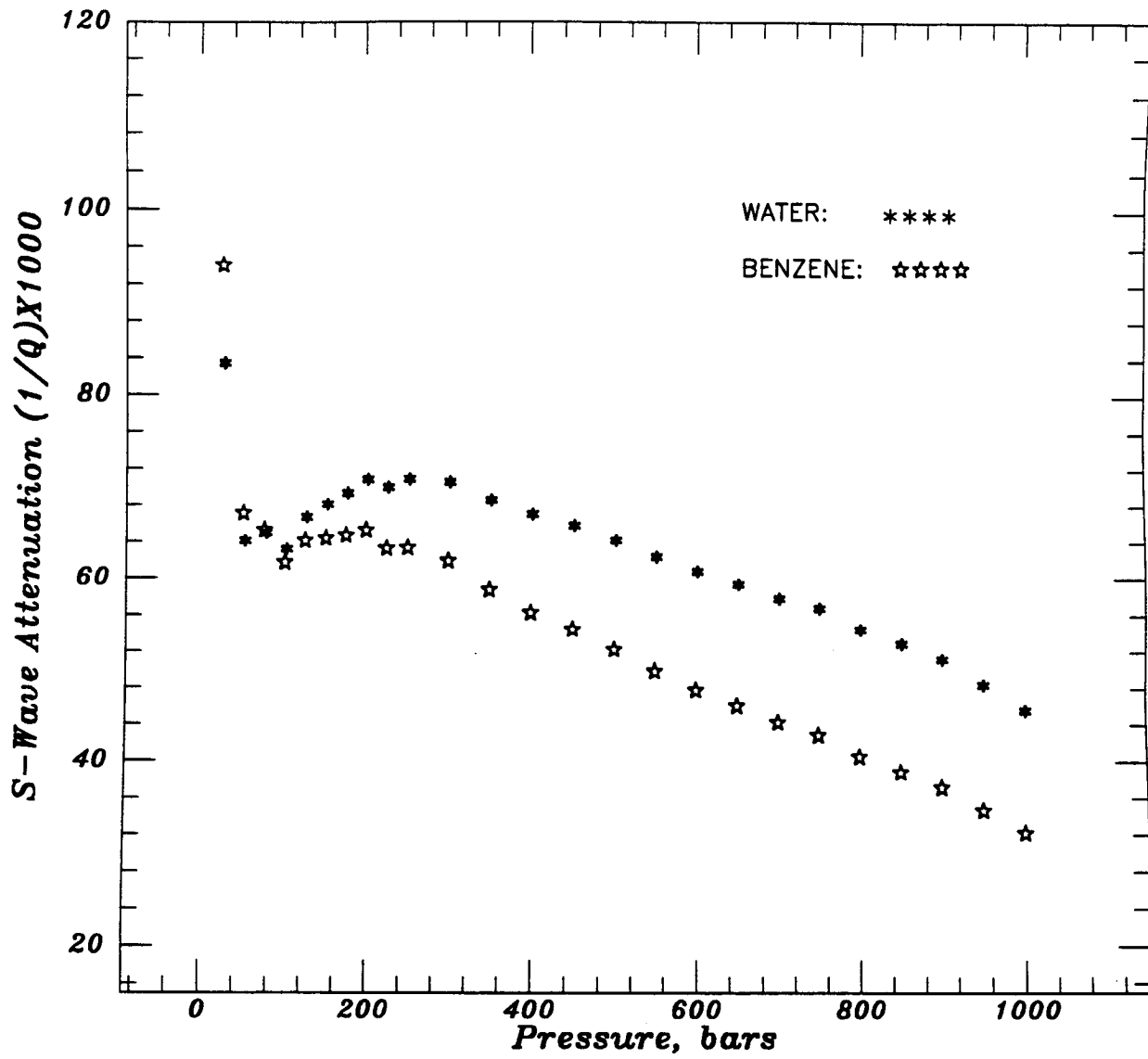


Fig. 3.9. Calculated attenuation for shear wave versus confining pressure for water and benzene-saturated Berea sandstone.

Effects of saturation hysteresis

As discussed earlier, fluid is macroscopically unrelaxed in rocks with non-uniform fluid distribution when $\xi_g \gg 1$. In this case fluid flow occurs locally within the microscopic unit (conduit and stiff pores). This mode is typical of ultrasonic measurements conducted on rocks of small permeability. In the following experimental data, frequency and permeability are of the order of 1 MHz and 1 μD , which gives an estimate for squirt number $\xi_g \sim 10^9$ (equation 6).

Knight and Nolen-Hoeksema (1990) measured compressional V_p and shear V_s wave velocities in tight gas sandstones versus water saturation during imbibition and drainage. The authors found that during imbibition V_p shows little variation with increasing saturation S until $S = 80\%$, at which point V_p increased dramatically from 3 km/s to 4 km/s. When S decreased (drainage), pronounced saturation hysteresis was observed in the range $30\% < S < 100\%$ with V_p during drainage greater than V_p during imbibition. They explained these results by different microscopic fluid distributions during saturation and drainage. At any given global saturation, the percentage of fluid that occupies thin cracks during drainage is larger than the percentage of fluid that occupies cracks during imbibition.

The parameters of the sample are: permeability $k=1.23 \mu\text{D}$, porosity $\phi = 5.2\%$, grain bulk modulus $K_s = .38 \text{ Mbar}$, and grain density $\rho_s = 2.630 \text{ g/cm}^3$. The frequency f were 1 MHz and .6 MHz for V_p and V_s respectively.

To estimate \tilde{K} we use: the crack porosity $\phi_C = .39\%$ (Mavko and Jizba, 1991), the rock bulk compliance at which cracks close $C_0^\infty = 3.45 \times 10^{-11} \text{ Pa}^{-1}$ (Jizba, 1991), $\Psi = 0$ (since fluid is macroscopically unrelaxed), and the size of the microscopic unit $\ell = .125 \text{ mm}$, $\Gamma = 3/8$ (thin fractures) (Walls, 1987), and frequency $f = .8 \text{ MHz}$.

We use $\beta = 50$, and $\alpha = .001$. This choice of small value for α is based on the fact that permeability for this rock decreases rapidly with confining pressure due to crack closure (Walls, 1987).

Figure 3.10 gives bulk modulus as a function of the global water saturation. This modulus was calculated separately for two different conduit saturation functions. Solid lines represent our theoretical predictions calculated from equation (63). The measured bulk modulus (calculated from V_p and V_s) is represented by letters D for drainage and B for imbibition. Figure 3.11 shows the two saturation functions used in these calculations.

A qualitative relation between permeability and the scale of the microscopic heterogeneity

As discussed earlier, the size of the microscopic unit ℓ is the distance between two adjacent stiff pores and depends on the microscopic heterogeneity scale. ℓ increases with increasing grain size, increasing clay content, and deteriorating sorting (Figure 3.1b). These factors affect permeability k such that increasing grain size acts to increase k while the other factors result in decreasing k (Nolen et al., 1992). It is possible, therefore, to relate qualitatively permeability to the microscopic heterogeneity of porous material. Equation (5), along with experimental data that exhibit peaks in attenuation, gives a unique relationship between k and ℓ , whenever a peak in attenuation is observed, provided that other parameters are known.

Figure 3.12 shows the scale of the microscopic heterogeneity ℓ versus $\text{Log}_{10} k$ for different rock samples. The figure shows that decreasing permeability results in increasing ℓ . Table 3.1 shows rock and fluid properties used in plotting Figure 3.12.

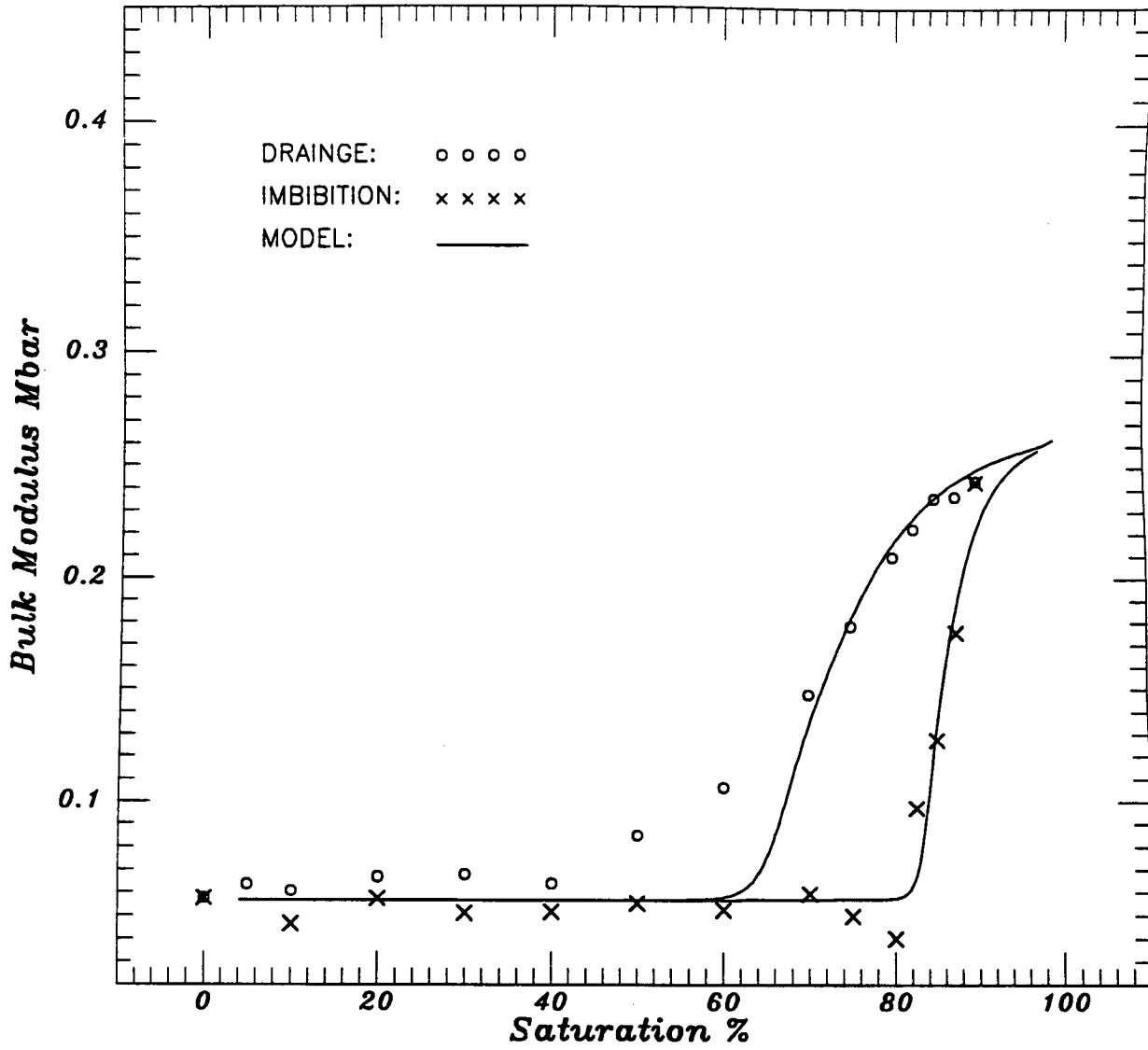


Fig. 3.10. Bulk modulus calculated from measured V_p and V_s versus saturation for drainage and imbibition in a tight gas sandstone (Knight and Nolen-Hoeksema, 1990). Solid lines are our theoretical predictions.

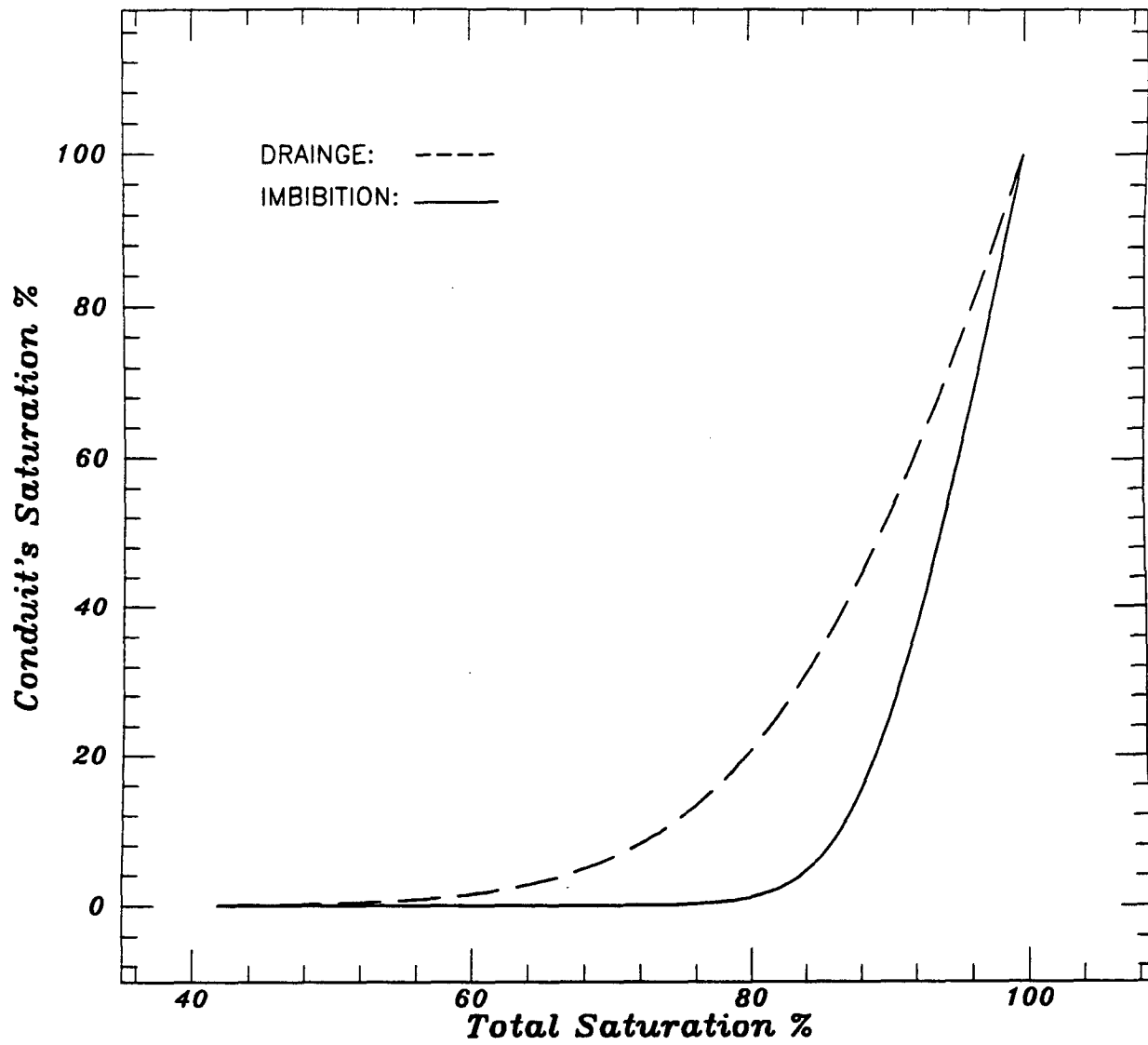


Fig. 3.11. Conduit saturation versus overall saturation for drainage and imbibition. These functions were used in calculating bulk modulus shown in Figure 3.10.

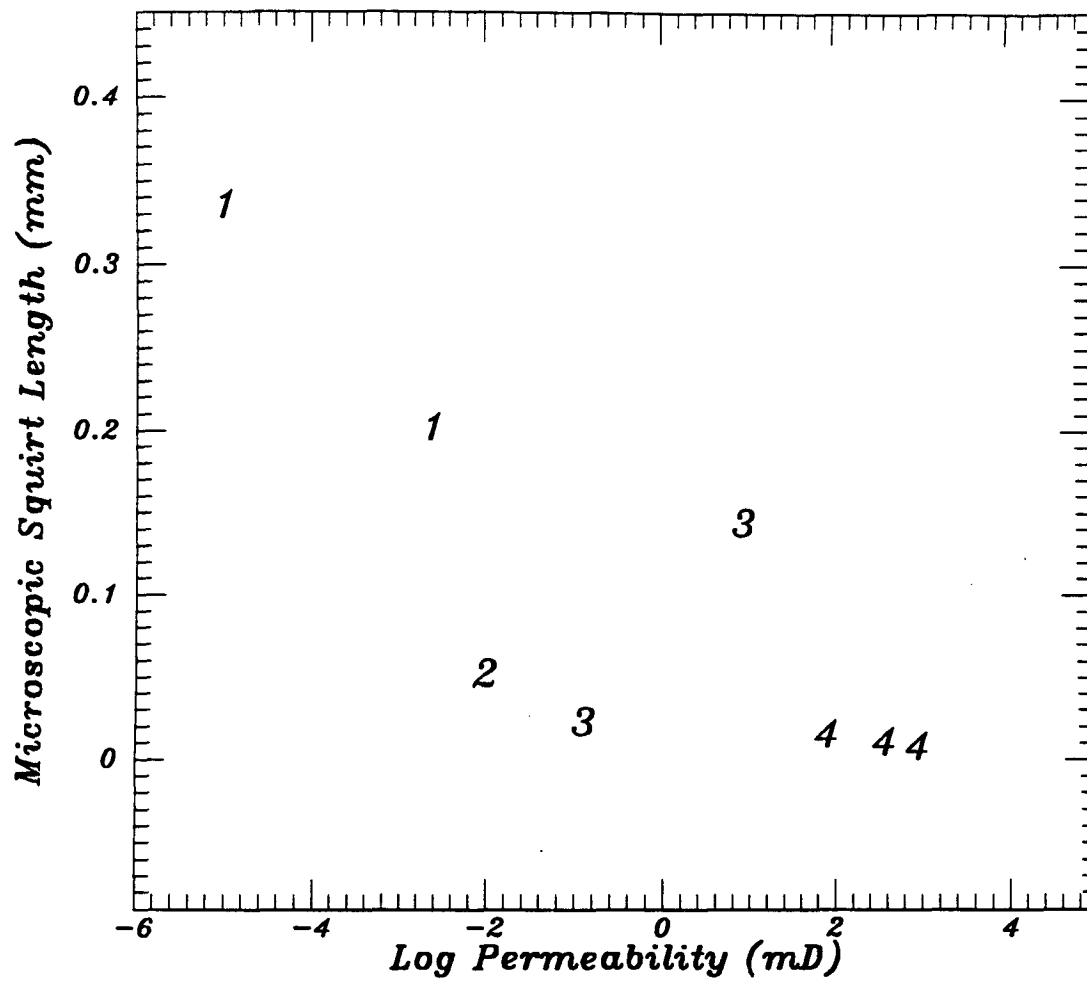


Fig. 3.12. The scale of the microscopic heterogeneity ℓ versus permeability for different rock samples.

Table 3.1. Rock and fluid properties used in plotting Figure 3.12.

Data Source	Rock Type	Fluid Type	$\text{Log } k_{10} \text{ (mD)}$	$\phi \%$	$f \eta C_f$	S %	$l \text{ (mm)}$
1	Grawacke	Water	-5.00	1.1	2.2×10^{12}	100.	0.336
1	Quartzite	Water	-2.60	3.8	4.4×10^{10}	100.	0.202
2	Vycor porous glass	Water	-2.0	28.0	3.0×10^9	100.	0.052
3	Sandstone	Water	-0.89	15.0	4.4×10^7	100.	0.023
3	Sandstone	Water	0.97	28.0	4.4×10^7	100.	0.144
4	Beara S.S.	Glycerol	1.90	18.0	1.1×10^3	68	0.016
4	Beara S.S.	Glycerol	2.60	22.0	1.1×10^2	62	0.011
4	Boise S.S.	Glycerol	2.96	30.0	3.5×10^2	60	0.008

Data from: 1) Paffenholz and Burkhardt, 1989; 2) Murphy, 1982;
3) Klimentos and McCann, 1990; and 4) Vo-Thanh, 1990.

Non-Uniform Fluid Distribution

In this section, we present data sets for non-uniform fluid distribution where fluid flow takes place within the microscopic and the macroscopic units.

Effects of frequency

Paffenholz and Burkhardt (1989), measured attenuation of extensional Q_E^{-1} and shear Q_S^{-1} waves versus frequency for graywacke ($k \sim .01 \mu\text{D}$, $\phi \sim 1.1\%$), Harz quartzite ($k = 2.5 \mu\text{D}$, $\phi = 3.8\%$), and Obemkirchner sandstone ($k = 9 \text{ mD}$, $\phi = 18.7\%$). For full saturation, a single broad peak that ranges from $f_c \sim 1$ to $f_c \sim 100$ Hz (centered at 5 Hz in a log scale) was observed for the graywacke ($\omega_c = 2\pi f_c$), two peaks for the quartzite at $f_c \sim 0.03$ Hz and $f_c \sim 1000$ Hz, and a single peak for the Obemkirchner sandstone at $f_c \sim 50$ Hz.

For full saturation, \tilde{R}^3 is of the order of the known volume of the sample \tilde{V}_T (\tilde{R} 6.6 cm).

For a qualitative analysis, equations (5) and (6) will have the same form except for the squirt length ℓ and \tilde{R} . Substituting into equation (5) with k , ϕ , and critical frequencies (5 Hz, 1000 Hz, .03 Hz, 1000 Hz, and 50 Hz) of the samples given above and using $\xi = 1$ and the following numeric constants derived from data: $\eta = 1$ cp, $C_f \sim 4.4 \times 10^{-10} \text{ Pa}^{-1}$, and $S = 1$, we have the following relations between the squirt length and the critical frequencies:

$$f_c = 5 \text{ Hz} : \ell = 0.34 \text{ mm, (graywacke)}$$

$$f_c = .03 \text{ Hz} : \tilde{R} = 3.7 \text{ cm, (quartzite)}$$

$$f_c = 1000 \text{ Hz} : \ell = 0.2 \text{ mm, (quartzite)}$$

$$f_c = 50 \text{ Hz} : \tilde{R} = 2.5 \text{ cm, (Obemkirchner sandstone)}$$

The peak observed in the graywacke ($f_c = 5$ Hz) and in the quartzite (the second peak at $f_c = 1000$ Hz) are due to the local flow mechanism since the calculated squirt length $\ell = 0.34$ mm and $\ell = 0.2$ mm are of the order of the size of the microscopic channels. The squirt length for the graywacke, however, is larger than that of the

quartzite. This can be explained in terms of the tortured channels that might be observed in the graywacke due to abundance of clay. This conclusion agrees with our previous results (Figure 3.12).

The peaks observed at $f_c = .03$ Hz (quartzite) and at $f_c = 50$ Hz (Obemkirchner sandstone) are due to the global squirt mechanism since the calculated squirt length $\tilde{R} = 3.7$ cm, and $\tilde{R} = 2.5$ cm are close to the estimated squirt length (i.e., $\tilde{R} = 6.6$ cm).

This qualitative analysis demonstrates the importance of permeability in studying the viscoelastic behavior of porous materials.

We model the attenuation data quantitatively for the quartzite when the sample is partially saturated with $S = 20\%$. We represent the pores by crack-like conduits which results in $\alpha, \phi_H, \phi_N \sim 0$ (see the discussion on relating α to the bulk properties when $\alpha \sim 0$). We also use $\phi_C \approx \phi_D \approx \phi = 3.8\%$ that follows from equation (10); and $\Gamma = 3/8$. The rock compressibility C_o is calculated from the available measurements of Young's and shear moduli at zero frequency for small saturation ($S = 20\%$) and is $C_o = 1.04 \times 10^{-10}$ Pa $^{-1}$. The compressibility term C_o^∞ is assumed to be $C_o^\infty = 0.8C_o$. We use the elastic properties of α -quartz ($C_s = 2.6 \times 10^{-11}$ Pa $^{-1}$ and Poisson's ratio $\nu \sim 0.08$) for the unknown values of C_s and ν . Assuming $\psi = 0.52$, we have $S_u = S_D = 10.7\%$, that follows from equation (4).

Using the relation $\Psi = \psi S = \tilde{R}^3 / \tilde{V}_T$, given by equation (2), and the known volume of the sample $V_T \sim 295$ cm 3 , and solving for the macroscopic squirt length \tilde{R} , we find that $\tilde{R} \sim 3.13$ cm. Bulk attenuation Q_K^{-1} is found as $Q_K^{-1} = \frac{Im(\tilde{K})}{Re(\tilde{K})}$. The solid line in Figure 3.13 is the calculated attenuation when the microscopic squirt length $\ell = 2$ mm. Circles represent the data points obtained from the relation $\frac{1-2\nu}{Q_K} = \frac{3}{Q_e} - \frac{2(1+\nu)}{Q_s}$ (Winkler, 1979); where Q_E^{-1} and Q_S^{-1} are the measured attenuation values of extensional and shear waves respectively.

We notice that for $S = 20\%$: $[\frac{f}{f_g}]_{data} \sim 33.0 \times 10^3$ Hz; and $[\frac{f}{f_g}]_{theory} \sim (\frac{\tilde{R}}{S\ell})^2 \sim 32.0 \times 10^3$ Hz.

Therefore, our theoretical prediction, obtained from equation (7), is extremely

close to the data.

Figures 3.14 and 3.15 show the attenuation of extensional and shear waves for the same sample modeled in Figure 3.13. The solid lines are our theoretical predictions.

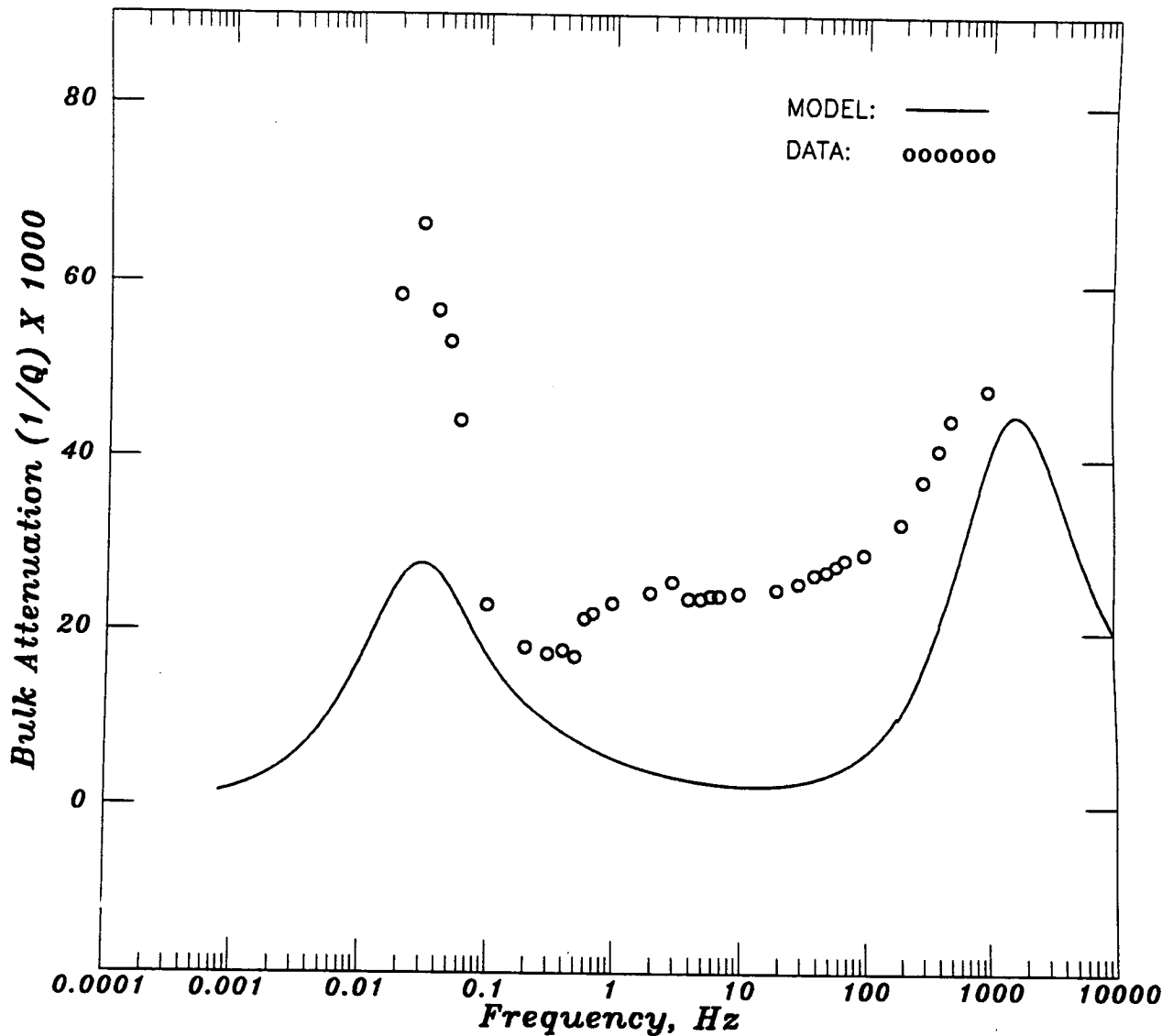


Fig. 3.13. Attenuation Q_K^{-1} as calculated from measured Q_E^{-1} and Q_S^{-1} versus frequency for Harz quartzite (Paffenholz and Burkhardt, 1989). The solid line is our theoretical prediction.

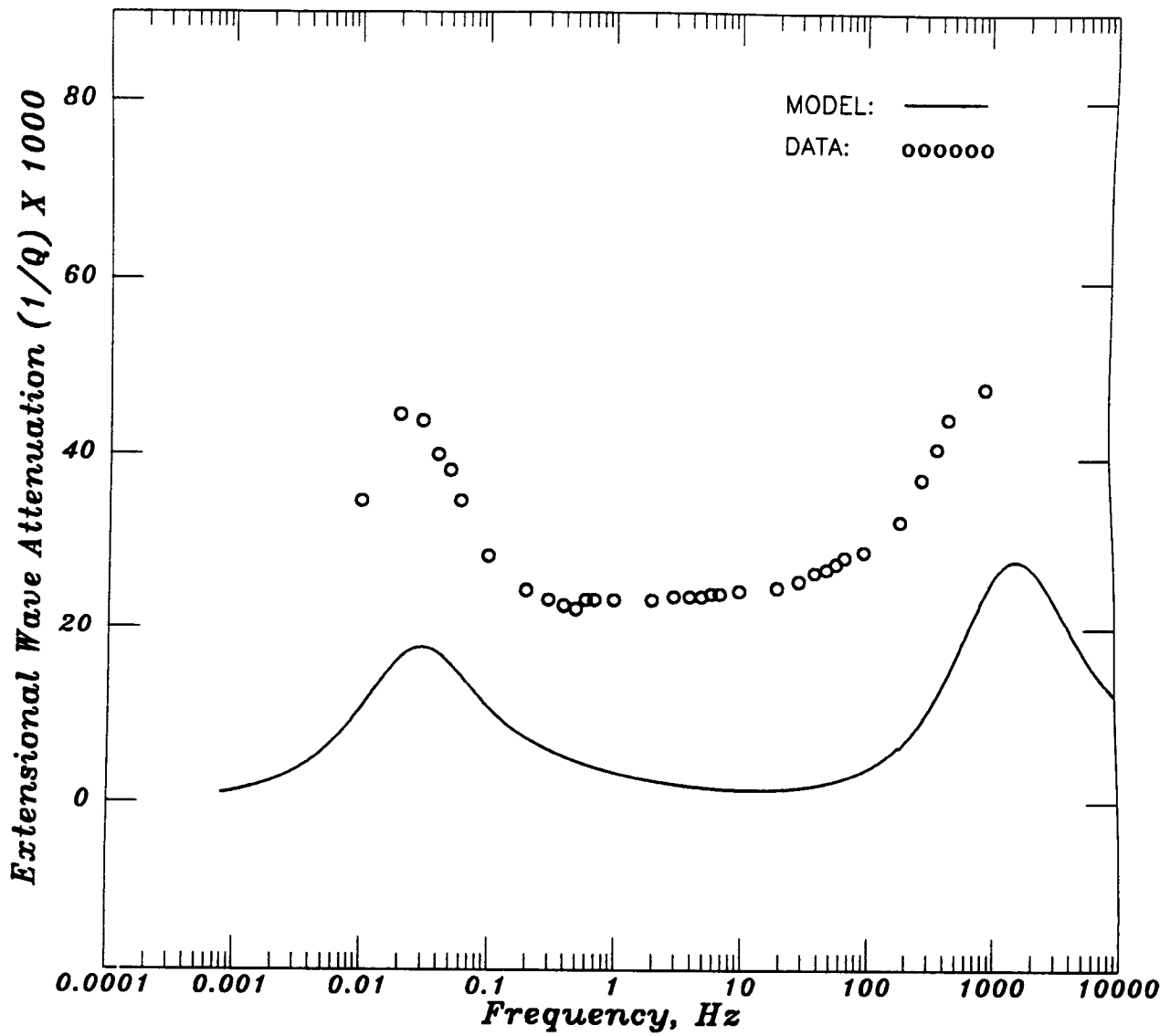


Fig. 3.14. Attenuation of extensional wave Q_E^{-1} versus frequency for Harz quartzite (Paffenholz and Burkhardt, 1989). The solid line is our theoretical prediction.

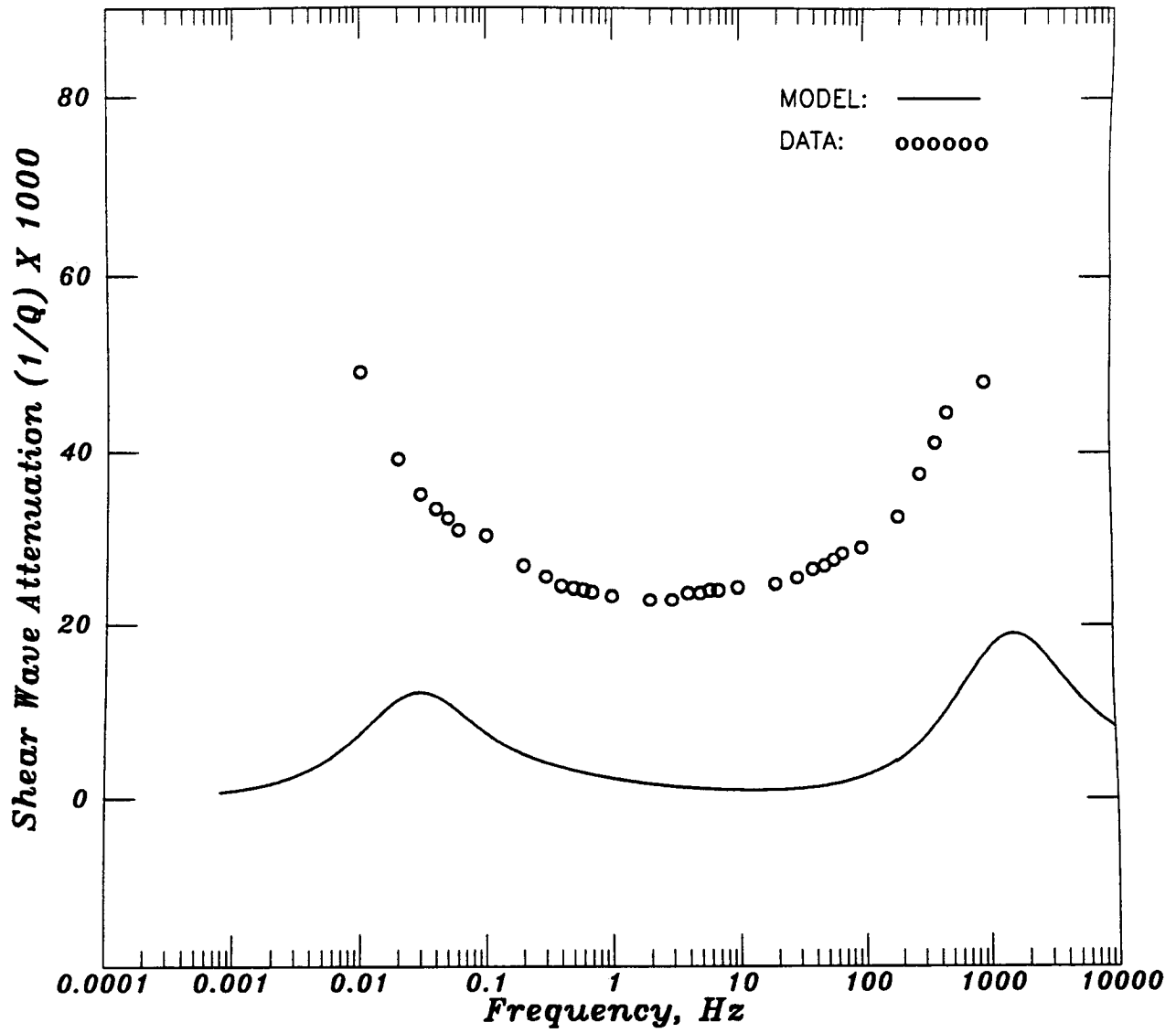


Fig. 3.15. Shear wave attenuation Q_s^{-1} versus frequency for Harz quartzite (Paffenholz and Burkhardt, 1989). The solid line is our theoretical prediction.

CONCLUSIONS

We used the squirt flow mechanism to study the effects of permeability, frequency, and saturation on the velocities and attenuation of seismic waves at two scales of fluid distribution: (1) local flow at the smallest scale of saturation heterogeneity and (2) global flow at a larger scale of fluid-saturated and dry patches. We found the circumstances under which each of these mechanisms prevails.

We formulated the solution in terms of characteristic frequencies ξ_ℓ and ξ_g that depend on the scale of fluid distribution, frequency, saturation, fluid and gas properties; and the macroscopic properties of rock such as permeability, porosity, and dry bulk modulus. The approximate expressions for ξ_ℓ and ξ_g are:

$$\xi_\ell \sim \frac{\omega\eta S^2 \ell^2 \Gamma(\phi C_f + C_o)}{\sqrt{3}k},$$

$$\xi_g \sim \frac{\omega\eta \bar{R}^2 \Gamma(\phi C_f + C_o)}{\sqrt{3}k}.$$

We showed that the solution satisfies Gassmann's equation (low frequency limit) and the high frequency limit given by Mavko and Jizba (1991). We demonstrated using experimental data that, in many cases, the squirt mechanism dominates the Biot's mechanism. We observed two peaks of acoustic wave attenuation due to the global squirt flow and the local squirt flow.

ACKNOWLEDGEMENTS

This work was sponsored by SRB and SAUDI ARAMCO, we thank T. Mukerji for helpful discussions.

Appendix A: Volumetric Strains

In this appendix, we calculate the pore volume strain and the associated pore wall displacements due to external confining stress with a unit magnitude σ_o applied to the external boundaries of a body that contains pores inside. \tilde{P}_p denotes the internal induced pore pressure normalized with respect to σ_o .

Single pores

Consider a single pore embedded in an elastic isotropic solid with total volume V_T and compressibility C_s . The volumetric strain of the pore $\epsilon_p < 0$ can be written in the following form:

$$\epsilon_p = \frac{\Delta V_o}{V_o}, \quad (A-1)$$

where ΔV_o is the reduction in the pore volume with $\Delta V_o = \tilde{V}_o - V_o$, where V_o and \tilde{V}_o are the original and the deformed pore volumes, respectively. ϵ_p can be expressed through pore compressibility C_{pc} as (Zimmerman, 1991):

$$\epsilon_p = -C_{pc}(\sigma_o - \tilde{P}_p) - C_s \tilde{P}_p. \quad (A-2)$$

Rearranging and noting that $C_{pp} = C_{pc} - C_s$, as in equation (18), we have:

$$\epsilon_p = -(C_{pc}\sigma_o - C_{pp}\tilde{P}_p). \quad (A-3)$$

Multiple pores

Consider decomposing the original pore volume V_o into two smaller portions with volumes V_{o1} and V_{o2} such that $V_o = V_{o1} + V_{o2}$. We assume that volumes V_{o1} and V_{o2} are connected and that the elastic properties of these pores are independent (no elastic interaction). The reduction in the total pore volume ΔV_o ($\Delta V_o < 0$) can be written in the following form:

$$\Delta V_o = (\tilde{V}_{o1} - V_{o1}) + (\tilde{V}_{o2} - V_{o2}), \quad (A-4)$$

where \tilde{V}_{o1} and \tilde{V}_{o2} denote volumes reduced due to applied stress σ_o . Using equation (A-1), the previous equation can be written in the following form:

$$\Delta V_o = V_{o1}\epsilon_p^{(1)} + V_{o2}\epsilon_p^{(2)}, \quad (A-5)$$

where $\epsilon_p^{(1)}$ and $\epsilon_p^{(2)}$ are the volumetric pore strains defined by equation (A-3). Dividing both parts of equation (A-5) by the total volume V_T , and using equation (A-1), we have:

$$\phi\tilde{\epsilon}_p = \phi_1\epsilon_p^{(1)} + \phi_2\epsilon_p^{(2)}, \quad (A-6)$$

where $\phi = \frac{V_o}{V_T}$, $\phi_1 = \frac{V_{o1}}{V_T}$, and $\phi_2 = \frac{V_{o2}}{V_T}$. Using equation (A-3), the previous equation can be written in the following form:

$$\phi\tilde{\epsilon}_p = -\phi_1[C_{pc}^{(1)}\sigma_o - C_{pp}^{(1)}\tilde{P}_p^{(1)}] - \phi_2[C_{pc}^{(2)}\sigma_o - C_{pp}^{(2)}\tilde{P}_p^{(2)}]. \quad (A-7)$$

Pore wall displacements

For a needle-like conduit with length H and radius a_o (Figure 3.16b), the volumetric strain is, as derived from equation (A-1):

$$\epsilon_p = \frac{\pi H(a_o - \Delta a)^2 - \pi H a_o^2}{\pi H a_o^2}, \quad (A-8)$$

where $\Delta a = a_o - \tilde{a}$, and \tilde{a} is the radius of the uniformly deformed conduit. Using equation (A-3) and noting that $(\Delta a)^2 \ll 2a_o\Delta a$, we have the following expression for Δa :

$$\Delta a = \frac{a_o}{2}(C_{pc}\sigma_o - C_{pp}\tilde{P}_p). \quad (A-9)$$

Deformed pore radius \tilde{a} is then:

$$\tilde{a} = a_o - \Delta a = a_o[1 - \frac{1}{2}(C_{pc}\sigma_o - C_{pp}\tilde{P}_p)]. \quad (A-10)$$

For a two-dimensional crack-like conduit, equation (A-1) can be written in the following form:

$$\epsilon_p = \frac{H[b_o - \Delta b]^2 d - H b_o^2 d}{H b_o^2 d}, \quad (A-11)$$

where, $2H$, $2d$, and $2b_o$ are the length, width, and the thickness of the crack, respectively (Figure 3.16c). $2\Delta b$ is the reduction in pore thickness due to applied stress. Solving for Δb and using equation (A-3), we have:

$$\Delta b = b_o(C_{pc}\sigma_o - C_{pp}\tilde{P}_p).$$

Deformed pore thickness \tilde{b} ($\tilde{b} = b_o - \Delta b$) is then:

$$\tilde{b} = b_o[1 - (C_{pc}\sigma_o - C_{pp}\tilde{P}_p)]. \quad (A - 12)$$

In a similar way, it can be readily seen that Deformed pore thickness \tilde{b} for a three-dimensional crack, with radius H , is given by equation (A-12) .

Appendix B: Gas Pressure

In this appendix, we calculate induced average fluid pressure (liquid and/or gas) in the equidimensional stiff pores. The solution is written using as yet unknown induced fluid pressure \tilde{P}_D in the conduit that is connected to the stiff pore (Figure 3.16a).

The decrement in the total pore space volume ΔV_o that is due to external confining pressure with unit magnitude can be written in the following form, using equation (A-6):

$$\Delta V_o = \tilde{V} - V_o = -V_{o1}[C_{pc}^D - C_{pp}^D\tilde{P}_D] - V_{o2}[C_{pc}^H - C_{pp}^H\tilde{P}_S]. \quad (B - 1)$$

The first and second terms in the right-hand side of equation (B-1) represent the reduction in the volumes of the conduit and stiff pore, respectively. \tilde{P}_D and \tilde{P}_S are induced fluid pressures in the conduit and stiff pore, respectively.

As pore surfaces contract, the reduction in the pore fluid volume ΔV_f ($\Delta V_f < 0$) is:

$$\Delta V_f = -V_f^D\tilde{P}_DC_f - V_f^H\tilde{P}_SC_f, \quad (B - 2)$$

where V_f^D and V_f^H are fluid volumes in the conduit and stiff pore, respectively. The first term denotes the reduction in fluid volume in the conduit, while the second term represents the reduction in fluid volume in the stiff pore.

The reduction in gas volume ΔV_g ($\Delta V_g < 0$) in both the conduit and stiff pore is then:

$$\Delta V_g = \Delta V_o - \Delta V_f. \quad (B-3)$$

Gas pressure is calculated as:

$$\tilde{P}_g = -\frac{\tilde{\epsilon}_g}{C_g}, \quad (B-4)$$

where $\tilde{\epsilon}_g$ is the strain of the gas $\tilde{\epsilon}_g = \frac{\Delta V_g}{V_g}$, C_g and V_g are the compressibility and the original volume of the gas. Substituting with equations (B-1), (B-2), and (B-3) into (B-4), we find:

$$\tilde{P}_g = -\frac{1}{C_g V_g} \{-V_o^D C_{pc}^D - V_o^H C_{pc}^H + \tilde{P}_D [V_o^D C_{pp}^D + C_f V_f^D] + \tilde{P}_S [V_o^H C_{pp}^H + V_f^H C_f]\}.$$

Fluid pressure in stiff pores is spatially uniform since the fluid is not allowed to move. Therefore, \tilde{P}_S is equal to gas pressure \tilde{P}_g (due to pressure continuity at the interface of gas and fluid in stiff pores). Using the term \tilde{P}_H to denote both \tilde{P}_S and \tilde{P}_g and solving the previous equation for \tilde{P}_H , we have:

$$\tilde{P}_H = \frac{[V_o^D C_{pc}^D + V_o^H C_{pc}^H] - [V_o^D C_{pp}^D + C_f V_f^D] \tilde{P}_D}{C_g V_g + V_o^H C_{pp}^H + V_f^H C_f}.$$

Dividing the numerator and the denominator of this equation by the total volume of the unit V_T , and using the relations: $\phi = \frac{V_o}{V_T}$, $\phi_D = \frac{V_o^D}{V_T}$, $\phi_H = \frac{V_o^H}{V_T}$, $S_D = \frac{V_f^D}{V_o^D}$, $S_H = \frac{V_f^H}{V_o^H}$, and $V_g/V_T = (V_o - V_f^D - V_f^H)/V_T = \phi - \phi_D S_D - \phi_H S_H$, we have:

$$\tilde{P}_H = \frac{[\phi_D C_{pc}^D + \phi_H C_{pc}^H] - \phi_D [C_{pp}^D + S_D C_f] \tilde{P}_D}{C_g [\phi - \phi_D S_D - \phi_H S_H] + \phi_H [C_{pp}^H + S_H C_f]}.$$

Noting that $\phi = \phi_D + \phi_H$, the previous equation can be rearranged into the following form:

$$\tilde{P}_H = \frac{[\phi_D C_{pc}^D + \phi_H C_{pc}^H] - \phi_D [C_{pp}^D + S_D C_f] \tilde{P}_D}{C_g [\phi_D (1 - S_D) + \phi_H (1 - S_H)] + \phi_H [C_{pp}^H + S_H C_f]}. \quad (B-5)$$

The saturation of the unit S_u given by equation (1) is the total fluid volume divided by the total pore volume:

$$S_u = \frac{S_D V_o^D + S_H V_o^H}{V_o^D + V_o^H} = \frac{S_D \phi_D + S_H \phi_H}{\phi}.$$

Adding and subtracting the term $(\phi_D C_{pp}^D + S_D \phi_D C_f)$ from the denominator of equation (B-5), and making use of equation (1), we have the following expression for \tilde{P}_H :

$$\tilde{P}_H = \frac{[\phi_D C_{pc}^D + \phi_H C_{pc}^H] - \phi_D [C_{pp}^D + S_D C_f] \tilde{P}_D}{\phi C_g (1 - S_u) + S_u \phi C_f + (\phi_D C_{pp}^D + \phi_H C_{pp}^H) - \phi_D [C_{pp}^D + S_D C_f]}.$$

Using equations (27) and (28), we write the previous equation in the following form:

$$\tilde{P}_H = \frac{\phi \tilde{C}_{pc} - \phi_D [C_{pp}^D + S_D C_f] \tilde{P}_D}{\phi C_g (1 - S_u) + S_u \phi C_f + \phi \tilde{C}_{pp} - \phi_D [C_{pp}^D + S_D C_f]}. \quad (B-6)$$

Using the following short-hand notations:

$$C_h = \tilde{C}_{pp}^D + S_D C_f, \quad (B-7)$$

$$C_e = \tilde{C}_{pp} + S_u C_f + (1 - S_u) C_g, \quad (B-8)$$

equation (B-6) can be written in the following form:

$$\tilde{P}_H = \frac{\phi \tilde{C}_{pc} - \phi_D C_h \tilde{P}_D}{\phi C_e - \phi_D C_h}.$$

Dividing the previous equation by ϕC_e , we arrive at:

$$\tilde{P}_H = \frac{\frac{\tilde{C}_{pc}}{C_e} - \tilde{C} \tilde{P}_D}{1 - \tilde{C}}, \quad (B-9)$$

where,

$$\tilde{C} = \frac{\phi_D C_h}{\phi C_e}. \quad (B-10)$$

The compressibility term C_e can be written in the form of equation (48) by using equation (30). C_h can be written in the form shown in equation (47) by substituting with the value of \tilde{C}_{pp}^D from equation (36).

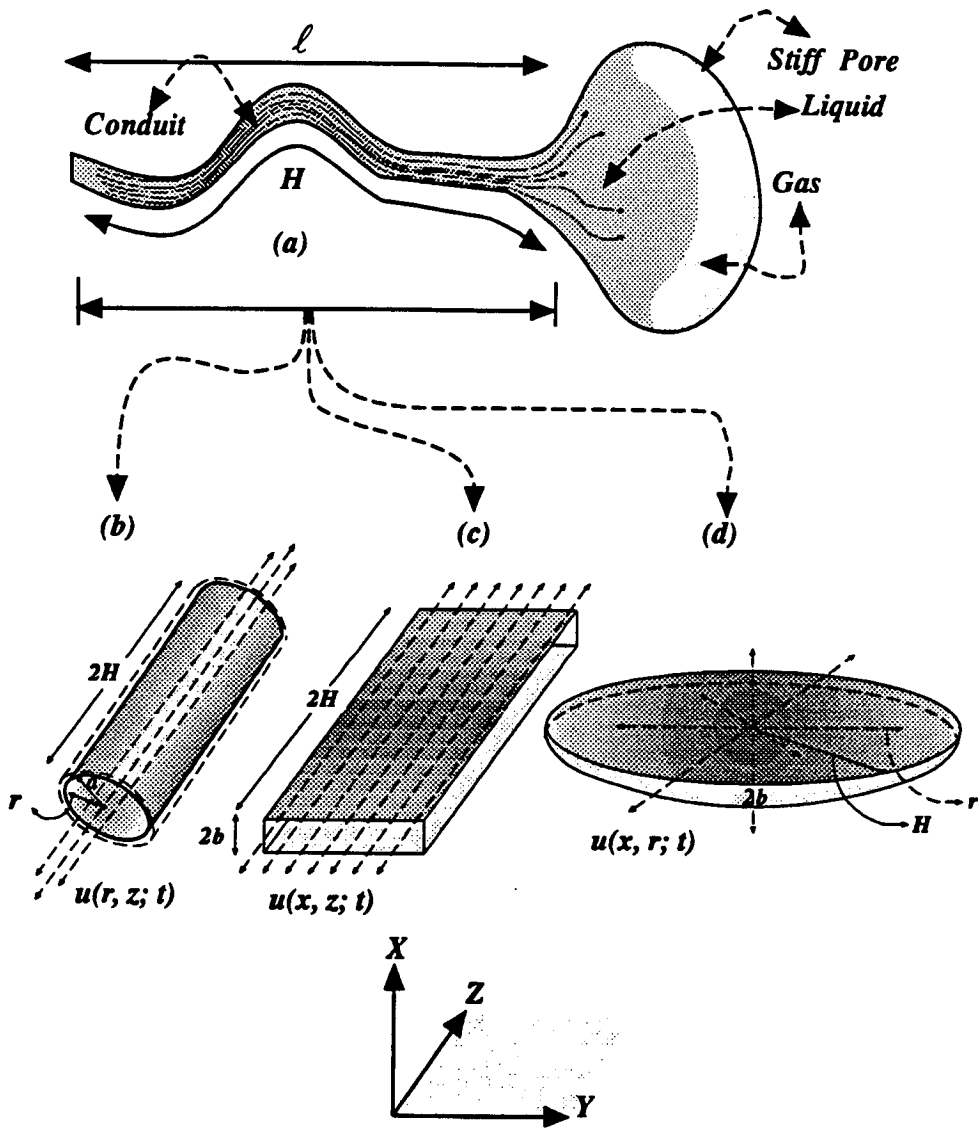


Fig. 3.16 (a) A microscopic unit composed of partially saturated stiff pore and a conduit; (b) a needle-like conduit; (c) a two-dimensional conduit; and (d) a penny-shaped conduit.

Appendix C: Fluid Pressure in a Needle-Like Conduit

In this appendix, we calculate the average induced fluid pressure due to applied stress in a needle-like conduit that is connected with a stiff pore. Fluid occupies the distance between $z = -L$ and $z = +L$ in the conduit and partially saturates the stiff pore (Figure 3.16b).

In the analysis below, it is assumed that all dynamic quantities are harmonically time-dependent with a harmonic factor $e^{i\omega t}$.

The average dynamic thickness of the pore \tilde{a} is, as in equation (A-10):

$$\tilde{a} = a_o - \frac{1}{2}a_o[C_{pc}^D - C_{pp}^D P_1(z)], \quad (C-1)$$

where, a_o is the average original radius of the conduit, and $P_1(z)$ is the fluid pressure.

For a laminar flow, fluid pressure gradient and fluid velocity u along the z direction satisfy the following equation:

$$\rho \frac{\partial u}{\partial t} = -\frac{\partial P_1}{\partial z} + \eta \left[\frac{\partial^2 u}{\partial r^2} + \frac{1}{r} \frac{\partial u}{\partial r} \right], \quad (C-2)$$

where r is the radial coordinate in the $x-y$ plane. For small deformation of the pore ($a \approx a_o$), the no-slip boundary condition for velocity $u(z, r, t)$ is $u(z, a_o, t) \approx 0$. The solution of equation (C-2) is then:

$$u_o(r, z) = \frac{1}{i\omega\rho} \frac{\partial P_1}{\partial z} \left[\frac{J_o(\sqrt{-i\omega/\nu}r)}{J_o(\sqrt{-i\omega/\nu}a_o)} - 1 \right], \quad (C-3)$$

where J_o is Bessel's function of the first kind and zero order, $\nu = \eta/\rho$ is kinematic viscosity, and ρ is fluid density. The continuity equation for axisymmetrical compressible flow in the cylindrical coordinate system (r, z) is:

$$\frac{1}{r} \frac{\partial}{\partial r}(r\rho\tilde{v}) + \frac{\partial\rho}{\partial t} + \frac{\partial(\rho u)}{\partial z} = 0, \quad (C-4)$$

where \tilde{v} is fluid velocity in the r direction. This velocity satisfies the boundary condition: $\tilde{v}_{r=\tilde{a}} = \frac{\partial\tilde{a}}{\partial t}$.

Fluid compressibility can be expressed in the following forms:

$$\frac{\partial \rho}{\partial t} = \frac{1}{v_f^2} \frac{\partial P_1}{\partial t} = \frac{i\omega}{v_f^2} P_1,$$

$$d\rho \ll \rho_0,$$

where ρ_0 is the reference fluid density at the initial pressure, and v_f is the velocity of sound in the fluid. By multiplying equation (C-4) by r and integrating in the r direction from 0 to \tilde{a} , we rewrite the first term in equation (C-4) as:

$$r\rho\tilde{v}|_0^{\tilde{a}} \approx \tilde{a}\rho_0 \frac{\partial \tilde{a}}{\partial t} = \frac{1}{2}i\omega\rho_0 a_0^2 [C_{pp}^D P_1(z) - C_{pc}^D]. \quad (C-5)$$

The second term of equation (C-4) can be approximated as:

$$\int_0^{\tilde{a}} \frac{\partial \rho}{\partial t} r dr \approx \frac{1}{2}i\omega\rho a_0^2 C_f P_1(z), \quad (C-6)$$

where the approximate expression $\tilde{a}^2 \approx a_0^2$ has been used, and $C_f = \frac{1}{\rho v_f^2}$. Substituting with u from (C-3) into the third term of (C-4), we find:

$$\int_0^{\tilde{a}} \frac{\partial(\rho u)}{\partial z} r dr \approx -\frac{a_0^2}{2i\omega} \left[1 - 2\frac{J_1(\lambda_1)}{\lambda_1 J_0(\lambda_1)}\right] \frac{\partial^2 P_1}{\partial z^2}, \quad (C-7)$$

where J_1 is Bessel's function of the first kind and first order, $\lambda_1 = \sqrt{\frac{-i\omega a_0^2}{\nu}}$. Adding (C-5), (C-6), and (C-7), we have:

$$\frac{\partial^2 P_1}{\partial r^2} - \Theta_1^2 P_1 - N_1 = 0, \quad (C-8)$$

where,

$$\Theta_1^2 = -\frac{\omega^2 \rho (C_{pp}^D + C_f)}{1 - \frac{2J_1(\lambda_1)}{\lambda_1 J_0(\lambda_1)}}, \quad (C-9)$$

$$N_1 = \frac{\omega^2 \rho C_{pc}^D}{1 - \frac{2J_1(\lambda_1)}{(\lambda_1)J_0(\lambda_1)}}.$$

Boundary condition for equation (C-8) is:

$$P_1(z = \pm L) = \tilde{P}_H. \quad (C-10)$$

The general solution of equations (C-8) and (C-10) is:

$$P_1 = 2G_1 \cosh(\Theta_1 z) + \frac{C_{pc}^D}{C_{pp}^D + C_f}, \quad (C-11)$$

where G_1 is a constant of integration.

Average fluid pressure in the conduit as expressed through constant G_1 is:

$$\bar{P}_1 = \frac{1}{2L} \int_{-L}^L P_1(z) dz = \frac{2G_1 \sinh(\Theta_1 L)}{\Theta_1 L} + \frac{C_{pc}^D}{C_{pp}^D + C_f}. \quad (C-12)$$

Using this value of \bar{P}_1 in equation (B-9) (Appendix B), we have:

$$\bar{P}_H = \frac{\frac{\check{C}_{pc}}{C_e} - \check{C} \left[\frac{2G_1 \sinh(\Theta_1 L)}{\Theta_1 L} + \frac{C_{pc}^D}{C_{pp}^D + C_f} \right]}{1 - \check{C}}. \quad (C-13)$$

Using equation (C-13) as the boundary condition in equations (C-10) and (C-11), and solving for constant G_1 , we have:

$$G_1 = \frac{\frac{\check{C}_{pc}}{C_e} - \frac{C_{pc}^D}{C_{pp}^D + C_f}}{2\check{C} \frac{\sinh(\Theta_1 L)}{\Theta_1 L} + 2(1 - \check{C}) \cosh(\Theta_1 L)}. \quad (C-14)$$

Substituting with G_1 into the expression for average fluid pressure (C-12), and using non-dimensional parameter Ω_1 instead of $\Theta_1 L$, we arrive at:

$$\bar{P}_1 = \frac{\frac{\check{C}_{pc}}{C_e} - \frac{C_{pc}^D}{C_{pp}^D + C_f}}{(1 - \check{C})(\Omega_1 \coth \Omega_1 - 1) + 1} + \frac{C_{pc}^D}{C_{pp}^D + C_f}. \quad (C-15)$$

Appendix D: Fluid Pressure in a Two-Dimensional Conduit

We calculate the average fluid pressure due to harmonic uniform loading in a two-dimensional conduit with length H and average thickness $2b_0$ (Figure 3.16c). Fluid occupies space between $z = -L$ and $z = +L$ in the conduit. The deformed thickness of the crack \bar{b} is, from equation (A-12):

$$\bar{b} = b_0 - b_0 \{C_{pc}^D - C_{pp}^D P_2(z)\}, \quad (D-1)$$

where $P_2(z)$ is fluid pressure. Fluid pressure gradient and fluid velocity u along the z direction satisfy the following equation:

$$\rho \frac{\partial u}{\partial t} = -\frac{\partial P_2}{\partial z} + \eta \frac{\partial^2 u}{\partial x^2}. \quad (D-2)$$

The no-slip boundary condition results in the following solution:

$$u(x, z) = -\frac{1}{i\omega\rho} \frac{\partial P_2}{\partial z} \left[1 - \frac{\cosh(\sqrt{\frac{i\omega x^2}{\nu}})}{\cosh(\sqrt{\frac{i\omega b_0^2}{\nu}})} \right]. \quad (D-3)$$

The continuity equation for this case is:

$$\frac{\partial \rho}{\partial t} + \frac{\partial(\rho\tilde{v})}{\partial x} + \frac{\partial(\rho u)}{\partial z} = 0, \quad (D-4)$$

where \tilde{v} is the velocity component of fluid along the x direction, and satisfies the boundary condition $\tilde{v}|_{x=\tilde{b}} = \frac{\partial \tilde{b}}{\partial t}$. Integrating equation (D-4) in the x direction from 0 to \tilde{b} , we have:

$$\int_0^{\tilde{b}} \frac{\partial \rho}{\partial t} dx = \frac{i\omega P_2 \tilde{b}}{v_f^2} \approx i\omega \rho b_0 C_f P_2(z), \quad (D-5)$$

$$x\rho\tilde{v}|_0^{\tilde{b}} \approx \tilde{b}\rho_0 \frac{\partial \tilde{b}}{\partial t} \approx i\omega \rho_0 b_0^2 [C_{pp}^D P_2(z) - C_{pc}^D], \quad (D-6)$$

where the approximate expression $\tilde{b}^2 \approx b_0^2$ has been used,

$$\int_0^{\tilde{b}} \frac{\partial(\rho v)}{\partial x} dx \approx -i\omega \rho_0 b_0 [C_{pc}^D - C_{pp}^D P_2(z)], \quad (D-7)$$

$$\int_0^{\tilde{b}} \frac{\rho u}{\partial y} dx \approx \frac{ib_0}{\omega} \left[1 - \frac{\tanh(\lambda_2)}{\lambda_2} \right] \frac{\partial^2 P_2}{\partial z^2}, \quad (D-8)$$

where $\lambda_2 = \sqrt{\frac{i\omega b_0^2}{\nu}}$. Adding equations (D-5), (D-6), (D-7), and (D-8), we have

$$\frac{\partial^2 P_2}{\partial z^2} - \Theta_2^2 P_2 - N_2 = 0. \quad (D-9)$$

With boundary conditions

$$P_2(z = \pm L) = \tilde{P}_H, \quad (D-10)$$

where,

$$N_2 = \frac{\rho_0 \omega^2 C_{pc}^D}{1 - \frac{\tanh(\lambda_2)}{\lambda_2}}, \quad (D-11)$$

$$\Theta_2^2 = -\frac{\rho \omega^2 (C_{pp}^D + C_f)}{1 - \frac{\tanh(\lambda_2)}{\lambda_2}}. \quad (D-12)$$

\tilde{P}_H is calculated in appendix B in equation (B-9) through fluid pressure \tilde{P}_2 in the conduit.

The general solution of equations (D-9) and (D-10) with G_2 as a constant of integration is:

$$P_2 = 2G_2 \cosh(\Theta_2 z) + \frac{C_{pc}^D}{(C_{pp}^D + C_f)}. \quad (D-13)$$

The average fluid pressure in the conduit is:

$$\tilde{P}_2 = \frac{1}{2L} \int_{-L}^L P_2(z) dz = \frac{2G_2 \sinh(\Omega_2)}{\Omega_2} + \frac{C_{pc}^D}{(C_{pp}^D + C_f)}, \quad (D-14)$$

where the symbol Ω_2 is used instead of $\Theta_2 L$. Following the analysis in appendix C, we find \tilde{P}_H as a function of constant G_2 , then use the resulting value of \tilde{P}_H as a boundary condition in equation (D-10); and solve for constant G_2 . substituting with G_2 into equation (D-14), we find the following expression for the average fluid pressure in a two-dimensional conduit:

$$\tilde{P}_2 = \frac{\frac{\tilde{C}_{pc}}{C_e} - \frac{C_{pc}^D}{C_{pp}^D + C_f}}{(1 - \tilde{C})(\Omega_2 \coth \Omega_2 - 1) + 1} + \frac{C_{pc}^D}{C_{pp}^D + C_f}. \quad (D-15)$$

Appendix E: Fluid Pressure in a Penny-Shaped Crack

We examine radial flow induced by crack wall displacement in a cylindrical coordinate system (r, x) , where r is the radial coordinate in the $y-z$ plane (Figure 3.16d). The thickness of the crack is, as given by equation (A-12):

$$\tilde{b} = b_o - b_o[(C_{pc}^D - C_{pp}^D P_r(r))]. \quad (E-1)$$

The approximate equation of fluid flow can be written as:

$$\rho \frac{\partial u}{\partial t} = -\frac{\partial P_r}{\partial r} + \eta \frac{\partial^2 u}{\partial x^2}, \quad (E-2)$$

where u is radial fluid velocity in the $y-z$ plane. Using the no-slip boundary condition $u(x, r, t) \approx u(b_o, r, t) = 0$, we have:

$$u(x, r) = -\frac{1}{i\omega\rho} \frac{\partial P_r}{\partial r} \left[1 - \frac{\cosh(\sqrt{\frac{i\omega x^2}{\nu}})}{\cosh(\sqrt{\frac{i\omega b_o^2}{\nu}})} \right]. \quad (E-3)$$

The continuity equation in the cylindrical coordinate system (r, x) is:

$$\frac{\partial(\rho v)}{\partial x} + \frac{\partial \rho}{\partial t} + \frac{\partial(\rho u)}{\partial r} + \frac{\rho u}{r} = 0, \quad (E-4)$$

where v is the component of fluid velocity along the x direction. This component satisfies boundary condition $v|_{x=\bar{b}} = \frac{\partial \bar{b}}{\partial t}$.

Integrating equation (E-4) in the x direction from 0 to \bar{b} , and using a procedure similar to that described in appendix C, we express equation (E-4) as:

$$\frac{\partial^2 P_r}{\partial r^2} + \frac{1}{r} \frac{\partial P_r}{\partial r} + \Theta_3^2 P_r - N_3 = 0. \quad (E-5)$$

This equation has to be solved with the following boundary condition:

$$P_r(r_0, t) = \tilde{P}_H, \quad (E-6)$$

where

$$N_3 = \frac{\rho_0 \omega^2 C_{pc}^D}{1 - \frac{\tanh(\lambda_3)}{\lambda_3}},$$

$$\Theta_3^2 = \frac{\rho \omega^2 (C_{pp}^D + C_f)}{1 - \frac{\tanh(\lambda_3)}{\lambda_3}}, \quad (E-7)$$

and $\lambda_3 = \sqrt{\frac{i\omega b_0^2}{\nu}}$.

The solution of equations (E-5) and (E-6) for finite values at the origin is:

$$P_r = G_3 J_0(\Theta_3 r) + \frac{C_{pc}^D}{(C_{pp}^D + C_f)},$$

where G_3 is a constant of integration. The average fluid pressure expressed through constant G_3 is:

$$\begin{aligned} \tilde{P}_r &= \frac{1}{\pi r_0^2} \int_0^{2\pi} d\theta \int_0^{r_0} P_r r dr \\ &= 2G_3 \frac{J_1(\Omega_r)}{\Omega_r} + \frac{C_{pc}^D}{(C_{pp}^D + C_f)}, \end{aligned}$$

where the symbol Ω_r is used instead of $\Theta_3 r_0$. Following the analysis in appendix A, we find average fluid pressure for a penny-shaped crack \tilde{P}_r as:

$$\tilde{P}_r = \frac{\frac{\tilde{C}_{pc}}{C_e} - \frac{C_{pc}^D}{(C_{pp}^D + C_f)}}{(1 - \tilde{C}) \left\{ \frac{\Omega_r J_0(\Omega_r)}{2J_1(\Omega_r)} - 1 \right\} + 1} + \frac{C_{pc}^D}{(C_{pp}^D + C_f)}. \quad (E-8)$$

Using the following approximation for thin conduits:

$$\lim_{\lambda_3 \rightarrow 0} \left\{ 1 - \frac{\tanh \lambda_3}{\lambda_3} \right\} \rightarrow \frac{1}{3} \lambda_3^2,$$

and taking λ_3 from equation (E-7), we arrive at:

$$\Omega_r^2 = \frac{-3\omega\eta r_o^2 (C_{pp}^D + C_f)}{b_o^2} i. \quad (E-9)$$

Appendix F: A Unified Expression for Fluid Pressure for Unidirectional Flow

In this appendix, we show that average fluid pressures in a needle-like crack, as in equation (C-15) and a two-dimensional crack, as in equation (D-15), can be expressed in the same form.

Equations (C-15) and (D-15) show that \tilde{P}_{1D} and \tilde{P}_{2D} have the same form except for the hydrodynamic part represented by $\Omega_1 = \Theta_1 L$ as in equation (C-9) and $\Omega_2 = \Theta_2 L$ as in equation (D-12). However, we will show that for thin conduits, both Ω_1 and Ω_2 will have the same form, when expressed in terms of permeability and porosity.

From equation (C-9), we have:

$$\Omega_1^2 = \Theta_1^2 L^2 = -\frac{\omega^2 \rho (C_{pp}^D + C_f)}{1 - \frac{2J_1(\lambda_1)}{\lambda_1 J_0(\lambda_1)}}, \quad (F-1)$$

where λ_1 is defined in equation (C-7). Term $1 - \frac{2J_1(\lambda_1)}{\lambda_1 J_0(\lambda_1)}$ can be expanded for thin conduits as follows:

$$1 - \frac{2J_1(\lambda_1)}{\lambda_1 J_0(\lambda_1)} \approx -\frac{\lambda_1^2}{8 - 2\lambda_1^2} \approx \frac{\omega \rho a_o^2}{8\eta} i.$$

This expansion results in the following expression for Ω_1 :

$$\Omega_1^2 = \frac{8\omega\eta L^2 (C_{pp}^D + C_f)}{a_o^2} i. \quad (F-2)$$

For a needle-like conduit, the permeability can be estimated by Kozeny-Carman's equation (e.g., Berryman and Blair, 1987):

$$k = \frac{a_o^2 \phi_D}{8T^2}.$$

Using the following expressions for tortuosity: $T = H/\ell$, and saturation in the conduit: $S_D = L/H$, we have

$$k = \frac{a_o^2 \phi_D \ell^2 S_D^2}{8L^2} \quad (F-3).$$

Expressing Ω_1 through k , we have:

$$\Omega_1^2 = \frac{\omega \eta (C_{pp}^D + C_f) S_D^2 \ell^2 \phi_D}{k} i. \quad (F-4)$$

For a two-dimensional crack, as in equation (D-12), we have:

$$\Omega_2^2 = \Theta_2^2 L^2 = -\frac{\rho \omega^2 (C_{pp}^D + C_f)}{1 - \frac{\tanh(\lambda_2)}{\lambda_2}},$$

where λ_2 is defined by equation (D-8).

Using the following approximation for thin cracks:

$$1 - \frac{\tanh(\lambda_2)}{\lambda_2} \approx \lambda_2^2/3, \quad (F-5)$$

one can write Ω_2 as:

$$\Omega_2^2 = \frac{3\omega \eta L^2 (C_{pp}^D + C_f)}{b_o^2} i.$$

For a crack-like conduit, permeability has the following form (e.g., Berryman and Blair, 1987):

$$k = \frac{b_o^2 \phi_D}{3T^2}.$$

Using expressions $T = H/\ell$ and $S_D = L/H$, we have:

$$k = \frac{b_o^2 \phi_D \ell^2 S_D^2}{3L^2}. \quad (F-6)$$

Expressing Ω_2 through k , we obtain:

$$\Omega_2^2 = \frac{\omega \eta S_D^2 \ell^2 \phi_D}{k} (C_{pp}^D + C_f) i. \quad (F-7)$$

Comparing equations (F-7) and (F-4), we find that $\Omega_1 = \Omega_2$ when both are expressed in terms of permeability and porosity. We use term Ω_u to denote the unified expression of Ω_1 and Ω_2 for unidirectional flow as given by equations (C-15) or (D-15).

Therefore, fluid pressure for unidirectional flow (needle-like or 2-D conduits) will have the following expression:

$$\tilde{P}_u = \frac{\frac{\tilde{C}_{pc}}{C_e} - \frac{C_{pc}^D}{C_{pp}^D + C_f}}{(1 - \tilde{C})(\Omega_u \coth \Omega_u - 1) + 1} + \frac{C_{pc}^D}{C_{pp}^D + C_f}, \quad (F - 8)$$

with

$$\Omega_u^2 = \frac{\omega \eta (C_{pp}^D + C_f) S_D^2 \ell^2 \phi_D}{k} i. \quad (F - 9)$$

Appendix G: Effects of Radial Flow on Fluid Pressure

In the following analysis, we examine the effects of fluid flow geometry (i.e., unidirectional versus radial) on fluid pressure.

Fluid pressure is expressed in equations (F-8), and (F-9) for unidirectional flow (a needle or a two-dimensional crack) and in equations (E-8) and (E-9) for radial flow (a three-dimensional crack). Pore geometries affect fluid pressure through the magnitude of pore compressibility. A pore with large compressibility has larger pore wall displacements that result in high fluid pressure.

In the limits $\omega \rightarrow 0$ (fluid is relaxed) and $\omega \rightarrow \infty$ (fluid is unrelaxed) the effects of fluid flow disappear from equations (F-8) and (E-8), and induced pressure is the same for both geometries. This observation implies that the dynamic (frequency-dependent) fluid pressure for both geometries differ merely due to their geometrical nature. This suggests the existence of as yet an unknown factor Γ associated with the nature of fluid flow, which is contained in Ω_u as in equation (F-9) for a unidirectional flow and in Ω_r as in equation (E-9) for a radial flow.

Therefore, equating the magnitudes of the compressibilities and the fluid pressures for both geometries as in (F-8) and (E-8), one can estimate the remaining effects of pore geometry on fluid pressure. This allows us to obtain a general formula for fluid pressure for any flow geometry in terms of parameter Γ .

Equating fluid pressures from equations (F-8) and (E-8), we have the necessary condition for fluid pressures in both geometries to be equal:

$$\{\Omega_u \coth(\Omega_u) - 1\} = \left\{ \frac{\Omega_r J_0(\Omega_r)}{2J_1(\Omega_r)} - 1 \right\}. \quad (G-1)$$

Approximating these functions by first terms of Taylor's expansions, we have in thin conduits:

$$\lim_{x \rightarrow 0} \frac{x J_0(x)}{2J_1(x)} - 1 \longrightarrow -\frac{x^2}{8},$$

$$\lim_{x \rightarrow 0} [x \coth(x) - 1] \longrightarrow \frac{x^2}{3},$$

and thus

$$\frac{\Omega_u^2}{3} = -\frac{\Omega_r^2}{8}. \quad (G-2)$$

We introduce the as yet unknown parameter Γ into Ω_u^2 and define $\tilde{\Omega}_\ell$ such that:

$$\tilde{\Omega}_\ell = \Gamma \Omega_u^2. \quad (G-3)$$

Therefore, equation (G-2) can be written as:

$$\tilde{\Omega}_\ell^2 = -\Omega_r^2. \quad (G-4)$$

Equations (G-3) and (G-4) show that fluid pressure for any pore geometry can be obtained from (E-8) or (F-8) by choosing an appropriate value for Γ .

If equation (F-8) is used as a basis in calculating fluid pressure, then Γ is unity for unidirectional flow and $\Gamma = \frac{3}{8}$ for radial flow. Now equation (F-8) has the following form:

$$\tilde{P}_\ell = \frac{\frac{\tilde{C}_{pc}}{C_e} - \frac{\tilde{C}_{pc}^D}{\tilde{C}_{pp}^D + C_f}}{(1 - \tilde{C})\{\tilde{\Omega}_\ell \coth \tilde{\Omega}_\ell - 1\} + 1} + \frac{\tilde{C}_{pc}^D}{\tilde{C}_{pp}^D + C_f}, \quad (G-5)$$

where \tilde{P}_ℓ is the unified average fluid pressure. We used the terms \tilde{C}_{pc}^D and \tilde{C}_{pp}^D instead of C_{pc}^D and C_{pp}^D to denote effective conduit compressibilities that might result from a combination of more than one specific geometry. $\tilde{\Omega}_\ell$ is obtained from equation (F-9) by introducing Γ and has the following expression:

$$\tilde{\Omega}_\ell^2 = \left(\frac{\omega \eta C_f S_D^2 \phi_D \ell^2}{k} \right) \mathcal{F}(C, S_u, \phi) i, \quad (G-6)$$

where

$$\mathcal{F}(C, S_u, \phi) = \frac{(C_{pp}^D + C_f)\Gamma}{C_f}. \quad (G-7)$$

Γ is a numerical parameter that describes the effects of flow divergence on fluid pressure and ranges from 1 for a unidirectional flow to $\frac{3}{8}$ for a radial flow. In particular, for thin conduit, fluid pressure for a unidirectional flow \tilde{P}_u given by equation (F-8) can be obtained from equation (G-5) when Γ is unity. When Γ is equal to $\frac{3}{8}$ (radial flow), equations (G-5) and (E-8) give the same expression for fluid pressure.

Using limit $\lim_{\tilde{\Omega}_\ell \rightarrow 0} (\tilde{\Omega}_\ell \coth \tilde{\Omega}_\ell) \rightarrow 1$ in equation (G-5), we obtain:

$$\tilde{P}_\ell|_{\tilde{\Omega}_\ell \rightarrow 0} \rightarrow \frac{\tilde{C}_{pc}}{C_e}. \quad (G-8)$$

Similarly, using limit $\lim_{\tilde{\Omega}_\ell \rightarrow \infty} (\tilde{\Omega}_\ell \coth \tilde{\Omega}_\ell) \rightarrow \infty$ in equation (G-5), we have:

$$\tilde{P}_\ell|_{\tilde{\Omega}_\ell \rightarrow \infty} \rightarrow \frac{\tilde{C}_{pc}^D}{\tilde{C}_{pp}^D + C_f}. \quad (G-9)$$

Equation (G-8) can be written in the form of equation (44) by making use of equation (27). Equation (G-9) can be written in the form that appears in equation (45) by using equations (35) and (36). Finally, equation (41) can be found by substituting with equations (G-8) and (G-9) into equation (G-5).

Noting that $\frac{\tilde{C}_{pc}}{C_e} = \tilde{P}_\ell|_{\tilde{\Omega}_\ell \rightarrow 0}$, fluid pressure in the stiff pore \tilde{P}_H as in equation (B-9) can be written in the form of equation (49).

The overall average fluid and gas pressure \tilde{P}_E in the whole pore space (i.e., in the conduit and stiff pore) is:

$$\tilde{P}_E = \frac{1}{V_o} [\tilde{P}_\ell V_f^D + \tilde{P}_H (V_g + V_f^H)].$$

Using the values of V_o , V_f^D , V_f^H , and V_g from Appendix A, \tilde{P}_E can be readily transformed into the expression given by (50).

Appendix H: Fluid Pressure in a Macroscopic Conduit

In Appendix G, we showed that the effects of the conduit geometry on the average fluid pressure can be expressed through an appropriate choice of the geometrical

factor Γ . Therefore, any conduit geometry will result in the same formula for the fluid pressure in the macroscopic conduit. Here, we adapt the procedures used in obtaining fluid pressure in a needle-like conduit (Appendix C), and solve for the fluid pressure in a macroscopic conduit with length $2H_G$. Fluid occupies the space between $z = -\tilde{L}$ and $z = +\tilde{L}$ in the conduit. The average dynamic thickness of the macroscopic conduit \tilde{a} can be written in the form (Appendix C):

$$\tilde{a} = a_o - \frac{1}{2}a_o[\tilde{C}_{pc} - \tilde{C}_{pp}P_G(z)], \quad (H-1)$$

where \tilde{C}_{pc} and \tilde{C}_{pp} are the compressibilities of the average conduit. Following the procedures in appendix C, we have:

$$\frac{\partial^2 P_G}{\partial r^2} - \Theta_G^2 P_G - N_G = 0, \quad (H-2)$$

where $\lambda_G = \sqrt{\frac{-i\omega a_o^2}{\nu}}$, and

$$\Theta_G^2 = -\frac{\omega^2 \rho (\tilde{C}_{pp} + C_f)}{1 - \frac{2J_1(\lambda_G)}{\lambda_G J_0(\lambda_G)}}, \quad (H-3)$$

$$N_G = \frac{\omega^2 \rho \tilde{C}_{pc}}{1 - \frac{2J_1(\lambda_G)}{\lambda_G J_0(\lambda_G)}}.$$

The boundary conditions for equation (H-2) is:

$$P_G(z = \pm\tilde{L}) = 0. \quad (H-4)$$

The solution of equations (H-2) and (H-4) is:

$$P_G = \frac{\tilde{C}_{pc}}{\tilde{C}_{pp} + C_f} \left[1 - \frac{\cosh(\Theta_G z)}{\cosh(\Theta_G \tilde{L})} \right]. \quad (H-5)$$

The average fluid pressure in the conduit is:

$$\tilde{P}_G = \frac{1}{2\tilde{L}} \int_{-\tilde{L}}^{\tilde{L}} P_G(z) dz = \frac{\tilde{C}_{pc}}{\tilde{C}_{pp} + C_f} \left[1 - \frac{1}{\tilde{\Omega}_G \coth(\tilde{\Omega}_G)} \right], \quad (H-6)$$

where $\tilde{\Omega}_G = \Theta_G \tilde{L}$. Taking the high frequency limit of equation (H-6), we have as in equation (55):

$$\tilde{P}_G|_{\tilde{\Omega}_G \rightarrow \infty} = \frac{\tilde{C}_{pc}}{\tilde{C}_{pp} + C_f}. \quad (H-7)$$

Equation (58) can be derived by substituting with equations (22) and (23) into equation (H-7).

Appendix I: Bulk Modulus Calculations

We obtain the compressibility of the unit shown in Figure (3.2b) by calculating the strain energy of the system due to uniform confining loading of unit magnitude. Saturation S is defined as the ratio of the total fluid volume to the volume of pore space V_o , and can be expressed as follows:

$$S = \frac{\phi \tilde{R}^3 + (V_T - \tilde{R}^3) \phi S_u}{V_o}, \quad (I-1)$$

where the first term in the numerator is fluid volume in the fully-saturated region \tilde{R}^3 , and the second term is fluid volume in the partially saturated region of volume $V_T - \tilde{R}^3$. Equation (I-1) can be written in the form of equation (3) by noting that $V_o = \phi V_T$ and using the definition $\Psi = \frac{\tilde{R}^3}{V_T}$.

Zimmerman (1991) described, using the reciprocity theorem, the procedures of calculating strain energy W , which can be written as:

$$W = W_o + W_{c1} + W_{c2}. \quad (I-2)$$

W_o is the strain energy in a unit without inclusions and is given by

$$W_o = \frac{1}{2} \sigma_o (\sigma_o C_s) V_T. \quad (I-3)$$

W_{c1} is the increment in the strain energy due to the work done by σ_o through the strain of the pore space and its constituents, integrated over the pore volume and is given by:

$$W_{c1} = -\frac{1}{2} \sigma_o [\phi \epsilon_G \tilde{R}^3 + \phi \epsilon_u (V_T - \tilde{R}^3)], \quad (I-4)$$

where ϵ_G represents pore strains in the fully-saturated region \tilde{R}^3 ; and ϵ_u represents pore strains in the uniformly saturated region.

The third term W_{c2} represents decrease in the strain energy due to induced pore pressure and has the following expression:

$$W_{c2} = -\frac{1}{2} \sigma_o C_s [\phi \tilde{P}_G \tilde{R}^3 + \phi \tilde{P}_E (V_T - \tilde{R}^3)], \quad (I-5)$$

where \tilde{P}_G is average pore pressure inside in the fully-saturated region, and \tilde{P}_E is average pore pressure outside the region \tilde{R}^3 .

Adding equations (I-3), (I-4), and (I-5), and noting that \tilde{P}_G and \tilde{P}_E are normalized with respect to σ_o , we have:

$$W = \frac{1}{2}\sigma_o^2 V_T [C_s - \phi\Psi(C_s\tilde{P}_G + \frac{\epsilon_G}{\sigma_o}) - \phi(1 - \Psi)(C_s\tilde{P}_E + \frac{\epsilon_u}{\sigma_o})]. \quad (I-6)$$

ϵ_G and ϵ_u will have the following forms as in equations (A-3) and (A-7), respectively:

$$\frac{\tilde{\epsilon}_G}{\sigma_o} = -(\tilde{C}_{pc} - \tilde{C}_{pp}\tilde{P}_G),$$

$$\phi\frac{\tilde{\epsilon}_p}{\sigma_o} = -\phi_D(\tilde{C}_{pc}^D - \tilde{C}_{pp}^D\tilde{P}_D) - \phi_H(C_{pc}^H - C_{pp}^H\tilde{P}_H).$$

Substituting with ϵ_G and ϵ_u into equation (I-6), and making use of equations (27) and (30), we have:

$$W = \frac{1}{2}\sigma_o^2 V_T [C_o - (1 - \Psi)(\phi_D C_{pp}^D \tilde{P}_D + \phi_H C_{pp}^H \tilde{P}_H + \phi C_s \tilde{P}_E) - \Psi \tilde{P}_G (C_o - C_s)]. \quad (I-7)$$

Assuming uniform stresses and strains throughout the unit (the wavelength is much larger than the size of heterogeneities), one can rewrite the strain energy of the unit as

$$\begin{aligned} W &= \frac{1}{2} \int_V \sigma_o \tilde{\epsilon} dv \\ &\simeq \frac{1}{2} \sigma_o \tilde{\epsilon} V_T, \end{aligned} \quad (I-8)$$

where $\tilde{\epsilon}$ is the resulting bulk strain of the unit. Solving equation (I-8) for $\tilde{\epsilon}$, we have:

$$\tilde{\epsilon} = \frac{2W}{\sigma_o V_T}.$$

The effective bulk modulus \tilde{K} is defined as:

$$\tilde{K} = \frac{\sigma_o}{\tilde{\epsilon}} = \frac{\sigma_o^2 V_T}{2W}. \quad (I-9)$$

Equation (63) can be obtained by substituting equation (I-7) into equation (I-9).

Appendix J: Limits Imposed on β

In this appendix, we impose upper and lower limits for the value of β . For a rough estimation, we use a spherical pore to represent the geometry of the stiff pore. The lower limit for β , ($\beta = 1$) can be estimated from the fact that the compressibility of an elongated conduit is always larger than the compressibility of a spherical pore (Zimmerman, 1991).

The upper limit is estimated from equation (23), which gives the following inequality:

$$C_o^\infty > \phi_H C_{pc}^H (1 + \alpha\beta).$$

Using the compressibility of a sphere (Zimmerman, 1991), we have:

$$C_{pc}^H = \frac{2(1 - \nu)}{\pi\mu}$$

Substituting with this expression into the previous equation, and making use of relation $\phi_H = \frac{\phi_\infty}{1 + \alpha}$, we arrive at the inequality (40).

REFERENCES

- Akbar, N., Dvorkin, J., and Nur, A., 1993, Relating P-wave attenuation to permeability: *Geophysics*, **58**, 20-29.
- Berryman, J. G., Thigpen, L., and Chin, R. C. Y., 1988, Bulk elastic wave propagation in partially saturated porous solids: *J. Acoust. Soc. Am.* **84**, 360-373.
- Berryman, J. G., and Blair, S. C., 1987, Kozeny-Carman relations and image processing methods for estimating Darcy's constant: *J. Appl. Phys.*, **62**, 2221-2228.
- Biot, M. A., 1956a, Theory of propagation of elastic waves in a fluid saturated porous solid. I. Low-frequency range: *J. Acoust. Soc. Amer.*, **28**, 168-178.
- Biot, M. A., 1956b, Theory of propagation of elastic waves in a fluid saturated porous solid. II. Higher-frequency range: *J. Acoust. Soc. Amer.*, **28**, 179-191.
- Bourbié, T., Coussy, O., and Zinszner, B., 1987, *Acoustics of porous media*: Gulf publishing Company.
- Brace, W. F., Walsh, J. B., and Frangos, W. T., 1969, Permeability of granite under high pressure: *J. Geophys. Res.*, **73**, 2225-2236.
- Cadoret, T., Marion, D., and Zinszner, B. E., 1992; 1 kHz Elastic wave velocities in partially saturated limestones: Evidence of fluid distribution effect: Expanded Abstract, SEG, 1992 annual meeting, New Orleans.
- Chatterjee, A. K., Mal, A. K., Knopoff, L., and Hudson, J. A., 1980, Attenuation of elastic waves in a cracked, fluid-saturated solid: *Math. Proc. Camb. Phil. Soc.*, **88**, 547-561.
- Coyner, K. B., 1977, Effects of stress, pore pressure, and pore fluids on bulk strain, velocity, and permeability in rocks: Ph.D. Thesis, MIT.
- Domenico, S. N., 1976, Effects of brine-gas mixture on velocity in an unconsolidated sand reservoir: *Geophysics*, **41**, 882-894.
- Dullien, F. A. L., 1992, *Porous media, Fluid transport and pore structure*: Academic Press, Inc., Second Edition.
- Dunn, K. J., 1987, Sample boundary effect in acoustic attenuation of fluid-saturated porous cylinders: *J. Acoust. Soc. Amer.*, **81**, 1259-1266.
- Dutta, N. C., and Odé, H., 1979, Attenuation and dispersion of compressional waves in fluid-filled porous rocks with partial gas saturation (White model)- Part I: Biot theory: *Geophysics*, **44**, 1777-1788.
- Dvorkin, J. and Nur, A., 1993, Dynamic poroelasticity: a unified theory with the squirt and the Biot mechanisms: *Geophysics*, **58**, in press.
- Dvorkin, J., Mavko, G., and Nur, A., 1993, Squirt flow in fully saturated rocks: Expanded Abstract, SEG, 63rd annual meeting, Washington, DC.

- Endres, A. L., and Knight, R., 1989, The effects of microscopic fluid distribution on elastic wave velocities: *The Log Analyst*, **30**, 437-445.
- Gassmann, F., 1951, Über die elastizität porö medien: *Vierteljahrsschrift der Naturforschenden Gesellschaft in Zurich*, **96**, 1-23.
- Gregory, A. R., 1976, Fluid saturation effects on dynamic elastic properties of sedimentary rocks: *Geophysics*, **41**, 895-921.
- Hamilton, E. L., 1972, Compressional-wave attenuation in marine sediments: *Geophysics*, **37**, 620-646.
- Han, D., 1987, Effects of porosity and clay content on acoustic properties of sandstones and unconsolidated sediments: Ph.D. Thesis, Stanford University.
- Jizba, D. L., 1991, Mechanical and acoustical properties of sandstones and shales: Ph.D. Thesis, Stanford University.
- Johnston, D. H., Toksöz, M. N., and Timur, A., 1978, Attenuation of seismic waves in dry and saturated rocks: *Geophysics*, **44**, 691-711.
- Jones, T. D., 1986, Pore fluids and frequency-dependent wave propagation in rocks: *Geophysics*, **51**, 1939-1953.
- Klimentos, T., and McCann, C., 1990, Relationships among compressional wave attenuation, porosity, clay content, and permeability in sandstones: *Geophysics*, **55**, 998-1014.
- Knight, R., and Nolen-Hoeksema, R., 1990, A laboratory study of the dependence of acoustic properties on microscopic fluid distribution: 31 Annual SPWLA Logging Symposium.
- Lucet, N., 1989, Vitesse et atténuation des ondes élastiques soniques et ultrasoniques dans les roches sous pression de confinement: Thèse de Doctorat de l'Université Paris 6.
- Mavko, G., and Jizba, D., 1991, Estimating grain-scale fluid effects on velocity dispersion in rocks: *Geophysics*, **56**, 1940-1949.
- Mavko, G. M., and Nur, A., 1979, Wave attenuation in partially saturated rocks: *Geophysics*, **44**, 161-178.
- Mavko, G. M., and Nolen-Hoeksema, R., 1993, Estimating seismic velocities in partially saturated rocks: Submitted to *GEOPHYSICS*.
- Moore, T. F., and Slobod, R. L., 1956, The effect of viscosity and capillarity on the displacement of oil by water: *Producers Monthly*, **20**, 20-30.
- Murphy, W. F., Winkler, K. W., and Kleinberg, R. L., 1986, Acoustic relaxation in sedimentary rocks: dependence on grain contacts and fluid saturation: *Geophysics*, **51**, 757-766.

- Murphy III, W. F., 1982, Effects of microstructure and pore fluids on the acoustic properties of granular sedimentary materials: Ph.D. Thesis, Stanford University.
- Murphy III, W. F., 1984, Acoustic measures of partial gas saturation in tight sandstones: *J. Geophys. Res.*, **89**, 11,549-11,559.
- Nolen, G., Amaefule, J.O., Kersey, D.G., Ross, G., and Rubio, R., 1992, Problems associated with permeability and V_{clay} models from textural properties of unconsolidated reservoir rocks: *The Log Analyst*, **33**, 177
- Nur, A., Tosaya, C., and Vo-Thanh, D., 1984, Seismic monitoring of thermal enhanced oil recovery processes: Paper RS6, 54th SEG meeting, Atlanta.
- O'Connell, R. J., and Budiansky, B., 1977, Viscoelastic properties of fluid-saturated cracked-solids: *J. Geophys. Res.*, **82**, 5719-5725.
- Ogushwitz, P. R., 1985, Applicability of the Biot theory. II. Suspensions: *J. Acoust. Soc. Amer.*, **77**, 441-452.
- Paffenholz, J., and Burkhardt, H., 1989, Absorption and modulus measurements in the seismic frequency and strain range on partially saturated sedimentary rocks: *J. Geophys. Res.*, **94**, 9493-9507.
- Palmer, I. D., and Traviolia, M. L., 1980, Attenuation by squirt flow in undersaturated gas sands: *Geophysics*, **45**, 1780-1792.
- Shumway, G., 1960, Sound speed and absorption studies of marine sediments by a resonance method: *Geophysics*, **25**, 451-467, 659-682.
- Spencer, J. W., 1981, Stress relaxations at low frequencies in fluid-saturated rocks: *J. Geophys. Res.*, **86**, 1803-1812.
- Vo-Thanh, D., 1990, Effects of fluid viscosity on shear-wave attenuation in saturated sandstones: *Geophysics*, **55**, 712-722.
- Walls, J. D., 1982, Tight gas sands-permeability, pore structure, and clay: *J. Pet. Tech.*, (November), 2708-2714.
- Walls, J. D., 1983, Effects of pore pressure, confining pressure and partial saturation on permeability of sandstones: Ph.D. Thesis, Stanford University.
- Wang, Z., and Nur, A., 1990, Dispersion analysis of acoustic velocities in rocks: *J. Acoust. Soc. Amer.*, **87**, 2384-2395.
- Wang, Z., 1989, Wave velocities in hydrocarbons and hydrocarbon saturated rocks-with applications to EOR monitoring: Ph.D. Thesis, Stanford University.
- White, J. E., 1975, Computed seismic speeds and attenuation in rocks with partial gas saturation: *Geophysics*, **40**, 224-232.

- White, J. E., 1986, Biot-Gardner theory of extensional waves in porous rod: *Geophysics*, **51**, 742-745.
- Widess, M. B., 1973, How thin is a thin bed?: *Geophysics*, **38**, 1176-1180.
- Winkler, K. W., 1979, The effects of pore fluids and frictional sliding on seismic attenuation: Ph.D. Thesis, Stanford University.
- Winkler, K. W., 1985, Dispersion analysis of velocity and attenuation in Berea sandstone: *J. Geophys. Res.*, **90**, 6793-6800.
- Zimmerman, R. W., 1991, *Compressibility of sandstones*: Elsevier science publ. Co., Inc.
- Zoback, M. D., 1975, High pressure deformation and fluid flow in sandstone, granite, and granular materials: Ph.D. Thesis, Stanford University.